UNIVERSITY OF Southampton

Development of a Table-Top Nanosecond Pulsed Fibre Laser for Use in Optical Resolution Photoacoustic Microscopy

Josh Spurrell

Thesis submitted for the degree of
Master of Philosophy

Supervisors : Prof. David Richardson & Dr. Shaif-ul Alam
Collaborators: Prof. Paul Beard & Dr. Thomas Allen of UCL

Date: December 3, 2017

Optoelectronics Research Centre
University of Southampton
Southampton, SO17 1BJ

Abstract

This thesis covers the construction and development of fibre laser Master Oscillator Power Amplifier (MOPA) systems for photoacoustic imaging applications. An initial system developed for photoacoustic tomography was built, based around the use of an Amplifier Spontaneous Emission (ASE) source, modulated by both an acousto-optical modulator (AOM) and an electro-optical modulator (EOM). The system relied on the use of an in-house custom fibre, which allowed the system to generate nanosecond pulses of 9.7mJ energy at 1064nm. This system was then developed to become a more portable system by removing the need for modulators by using a Superluminescent diode (SLED) as a seed source. Despite the size reduction of the system, it was still capable of a 5mJ output. A new system focused on optical resolution photoacoustic microscopy (OR-PAM) was then built. The drawbacks and merits of three different seed sources, a Fabry-perot diode, an ASE source and a distributed feedback (DFB) diode were investigated, indicating that for narrow line width amplification the DFB was best suited. Finally second harmonic generation was tested using the OR-PAM system. We successfully generated over 1μJ of the second harmonic in 3-20ns pulses at repetition rates between 100kHz and 1MHz. The system was then integrated with UCL system to image biological tissue.

Contents

List of Figures

Declaration of Authorship

I Joshua Spurrell declare that this thesis and the work presented in it are my own and has been generated by me as the result of my own original research.

Development of a Table-Top High-Energy Nanosecond Pulsed Fibre Laser Pumped OPO Tuneable Between 450-700nm for Use in Optical Resolution Photoacoustic Microscopy

I confirm that:

- This work was done wholly or mainly while in candidature for a research degree at this University;
- Where any part of this thesis has previously been submitted for a degree or any other qualification at this University or any other institution, this has been clearly stated;
- Where I have consulted the published work of others, this is always clearly attributed;
- Where I have quoted from the work of others, the source is always given. With the exception of such quotations, this thesis is entirely my own work;
- I have acknowledged all main sources of help;
- Where the thesis is based on work done by myself jointly with others, I have made clear exactly what was done by others and what I have contributed myself;
- Parts of this work have been published (see list of publications)

Acknowledgements

Firstly I would like to thank my supervisors Professor David Richardson and Dr Shaif-ul Alam, who helped guide both my theoretical learning and the practical aspects of my research. I always felt able to get support from them throughout my time studying. Alongside my supervisors, Dr Martin Berendt provided me with a wealth of knowledge and expertise. From my first days in the laboratory until I left, Dr Berendt helped me with design decisions, practical construction assistance, understanding of the physics involved and help with my day-to-day work.

I would also like to thank the other members of our research group who were always happy and willing to provide constructive feedback, help me set up new tests or teach me new techniques. Particularly I would like to thank Dr Lin Xu for his assistance with my work in second harmonic generation and designing an OPO cavity.

I would like to thank the members of UCL who were involved with my project, specifically Professor Paul Beard and Dr Thomas Allen. Dr Allen made multiple trips down to the ORC to test our systems, as well as testing and analysing the system we delivered to UCL.

I would like to thank all the members of the team led by Dr Jayanta Sahu for fabricating our large core custom fibre, which enabled us to reach much higher pulse energies than we could achieve with any commercially available fibre. I would also like to thank all of the technicians, IT and support staff within the ORC, who helped me at various stages throughout my studies. I am also very thankful to EPSRC for funding my research.

Finally I would like to thank my wife who supported and motivated me throughout the entire of my studies as well as my parents for tirelessly reading draft versions of my thesis and providing helpful feedback.

List of Abbreviations

AOM	Acousto-Optic modulator
ASE	Amplified Spontaneous Emission
AWG	Arbitrary Waveform Generator
BBO	Barium Borate
BPF	Band Pass Filter
BPM	Birefringent Phase Matching
BDO	Beam Delivery Optics
Cir	Circulator
CW	Continuous Wave
DC	Direct Current
DCF	Double Clad Fibre
DER	Dynamic Extinction Ratio
DFB	Distributed Feedback
DFG	Difference Frequency Generation
EDFA	Erbium Doped Fibre Amplifier
EOM	Electro-Optic Modulator
EPSRC	Engineering and Physical Sciences Research Council
ER_{DC}	Direct Current Extinction Ratio
FBG	Fibre Bragg Grating
FP	Fabry-Perot
FRM	Faraday Rotating Mirror
FWHM	Full Width at Half Maximum
ISO	Isolator
KBO	Potassium titanyl phosphate
LBO	Lithium Triborate
LMA	Large Mode Area
MCVD	Modified Chemical Vapour Deposition
MOFA	Master Oscillator Fibre Amplifier
MOPA	Master Oscillator Power Amplifier
MOPFA	Master Oscillator Power Fibre Amplifier
NA	Numerical Aperture
NCPM	Non-Critical Phase Matching
Nd:YAG	Neodymium-doped Yttrium Aluminium Garnet
OPA	Optical Parametric Amplification
OPO	Optical Parametric Oscillator
OR-PAM	Optical Resolution - Photoacoustic Microscopy
ORC	Optoelectronic Research Centre
OSA	Optical Spectrum Analyser
OSNR	Output Signal to Noise Ratio
PA	Photoacoustic
PAT	Photoacoustic Tomography
PDU	Pump Dump

PSC	Pump and Signal Combiner
PM	Polarisation Maintaining
PRF	Pulse Repetition Frequency
RF	Radio Frequency
SBS	Stimulated Brillouin Scattering
SFG	Sum Frequency Generation
SHG	Second Harmonic Generation
SLED	Superluminescent Diode
SNR	Signal to Noise Ratio
SPM	Self-Phase Modulation
SRS	Stimulated Raman Scattering
THG	Third Harmonic Generation
UCL	University College London
WDM	Wavelength Division Multiplexer
XPM	Cross-Phase Modulation
YDFA	Ytterbium Doped Fibre Amplifier

1 Introduction

1.1 Photoacoutsic Imaging

Photoacoustic (PA) imaging is a newly developing field facilitated by the availability of higher pulse energy laser systems. With high resolution, high contrast images, PA imaging offers the potential to further our understanding of biological processes and anatomy. PA imaging is a combination of ultrasound and optical imaging, providing benefits from the two modalities. Unlike traditional ultrasound imaging, PA techniques offer the ability to detect haemoglobin and lipids[1], while maintaining a greater penetration depth than if a purely optical system was used. PA imaging is able to deliver information about both the structural and functional characteristics, bringing the potential to improve diagnosis and understanding of major diseases, including cancer.

The basis of PA imaging relies on the rapid heating of tissue, due to absorption of pulsed laser light (most commonly at wavelengths between 550-900nm). The heating caused from the absorption will typically increase the temperature of the cells by less than 0.1K (significantly lower than the damage threshold)[1]. Although small, the temperature increase results in a pressure rise, the relaxation of which produces broadband ($\sim 10MHz$) acoustic waves. The waves can be detected at the surface of the tissue using ultrasound receivers. By combining information of both the time delay of the pulses, and the speed of propagation an image can be reconstructed using techniques such as backprojection. A schematic of the PA imaging principle is show in figure 1.

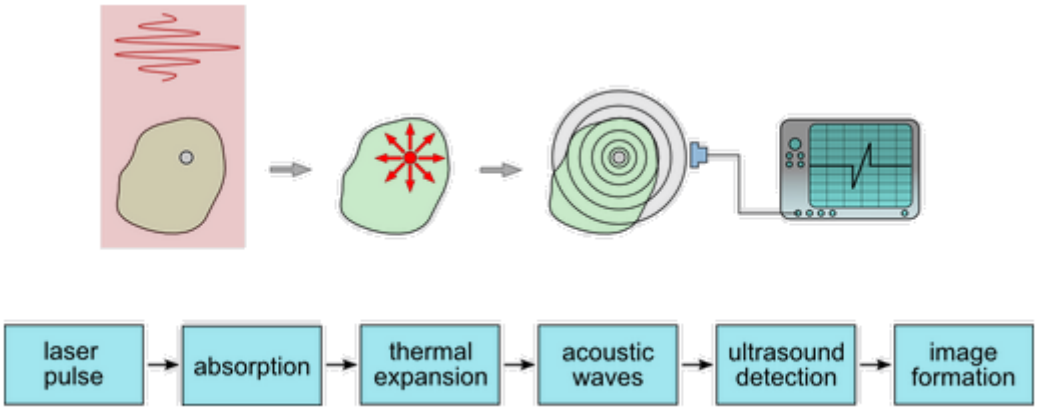

Figure 1: The basic principles of PA imaging. Image taken from RECENDT [2]

The physics behind photoacoustic effects were first described by Alexander Graham Bell in 1880[6]. However, there was very little scientific development due to the lack of suitable light sources. This was resolved with the realisation of the laser, providing high peak power and spectral pure sources that could be used for PA sensing applications. Despite this advancement, it was not until 1995[7] that PA devices began to be used for biomedical imaging, and it took until the mid-2000s before *in vivo* images were produced[7]. This development attracted significant interest and the field began to grow rapidly, with further system improvement and developments of image reconstruction algorithms.

There are two main configurations for PA imaging systems, Photoacoustic tomography (PAT) and Photoacoustic microscopy (PAM). PAT is the more general approach, and due to its design, is less restrictive than PAM systems. A typical PAT system will illuminate the entire surface of the sample tissue, generally using NIR wavelengths which can penetrate significantly throughout the tissue. The image can then be reconstructed from the generated acoustic waves detected at the surface of the tissue. An example of the acquired image is shown in figure 2. PAM differs in that a focused beam is used, only illuminating a small section of the sample tissue at any one time, and being raster scanned over the complete sample. The image can be generated by the

combination of the acquired signals, without the need of a complex algorithm.

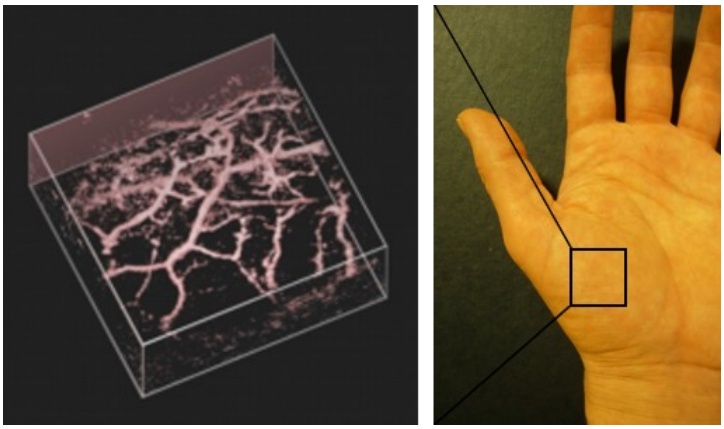

Figure 2: Volume rendered in vivo photoacoustic image of the vascular anatomy in the palm of the hand. Image and caption taken from UCL Photoacoustic Imaging Group [3]

Since conception, PA imaging systems have been evolving and initial proof-of-concept laboratory experiments have been conducted. More recently, initial commercial scanners are beginning to appear. However, with current laser sources, these systems are being held back from reaching their true potential as portable, easily used practical imaging solutions. Current systems rely on large solid state and dye lasers to produce the required wavelengths. Although this works in principle, the size of the PA imaging systems is not practical for widespread use in a medical environment. The actual PA scanner is of table top size, so if the size of the laser source could be reduced, then PA systems could make the next step to becoming more widely used.

1.2 Fibre Lasers and Amplifiers

Fibre lasers systems is a rapidly developing field both commercially and in terms of research. One of the key benefits of fibre systems is the ability to coil the system down to small areas, meaning the laser system can be very compact and portable. The added benefit of a single alignment process during splicing the system together aids in the portability and robustness of fibre systems. Fibre systems still play a huge role within the ever expanding telecommunications field, and the consistent need for more bandwidth and cheap efficient systems will help to drive the development of fibre systems in the future. Fibre based systems have been developed running at multiple wavelengths, for example 1550nm and 1060nm, as well as over huge ranges of repetition rates, from hertz to Gigahertz. Another significantly large field that uses fibre based systems is material processing, where fibre systems are used to cut and weld materials. Figure 3 shows a laser welder used in the UK capable of outputting 16kW. The flexibility of fibre systems themselves, as well as the range of operating conditions, has attracted more and more people to use fibre based systems within all areas of research.

Rare-earth doped fibres are the basis of any fibre laser or amplifier. Much like standard fibres, they generally consist of a central core in which light will propagate, surrounded by a lower refractive index cladding and finally covered with a protective polymer coating. Unlike a typical optical fibre, used for data transmission, the core is doped with a chosen rare-earth, such as erbium or ytterbium. By doping the fibre core, light propagating through the core can interact with the rare-earth ions. Under the right circumstances, based on the rare-earth used, it is possible to amplify the incident light via stimulated emission. The principle of fibre lasers is identical to that of solid state lasers; however, the gain medium is spread over the entire length of the fibre core at a much lower ion concentration. As with a traditional laser, to create a fibre laser, a pump source, a cavity and a gain medium are required. The gain medium is provided by the doped fibre, and the cavity is typically set up using fibre Bragg gratings (FBG) which act as reflectors. The gratings can be designed to reflect different amounts of light, and thus it is possible to create partial reflectors that can act as an output mirror for the cavity. The fibre laser can be pumped by a fibre coupled diode passed through the gratings, as the gratings

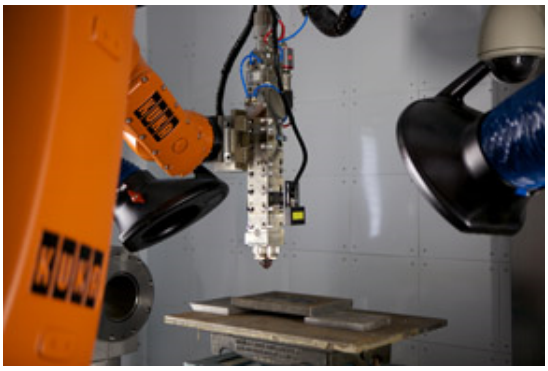

Figure 3: Image of a fibre laser based material processing set-up used to weld materials together. Image taken from Nuclear AMRC [4]

are wavelength dependant, and thus can be designed to allow the pump light to pass, while reflecting the signal wavelength.

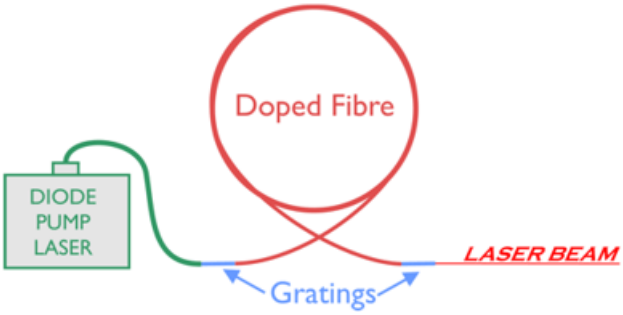

Figure 4: Diagram showing a simple fibre laser, consisting of a pump source, a gain medium in the form of a doped fibre, and a cavity produced through the use of fibre Bragg gratings. Image from ORC - How Fibre Lasers Work [5]

The first rare-earth doped fibre laser was realised in the early 1960's by Elias Snitzer and Charles J. Koester; A Neodymium fibre amplifier with 47dB gain over 1m. Early fibre laser systems were often out-performed by solid-state lasers, which had the advantage of higher powers and efficiencies. This was mainly due to the large losses in early fibres, as well as the lack of availability of practical pump sources, and therefore there was not significant research into the field. A resurgence in fibre lasers didn't appear until almost ten years later when Corning Glass Works were able to produce an optical fibre that had a loss of 17dB per kilometre[8]. By changing the constituent elements of their doped silica fibres, they were quickly able to reduce this loss down to only 4dB per kilometre within a few years. Another key development was made in 1985 when S.B. Poole et al vastly improved the technique used for producing rare-earth doped fibres [9]. The modified chemical vapour deposition (MCVD) process involves depositing a soot layer of silica and other desired substances on the inner surface of a heated silica glass tube. The gas mixture passed through the tube can be adjusted, allowing for layers of varying refractive index to be produced. Finally the glass tube is heated to 2000 degrees, collapsing the layers into a single solid structure. This process allowed for the production of low loss doped fibres, due to being able to use high purity materials while avoiding contamination. Alongside the development of the optical fibres, extensive work was being performed on semiconductor laser diodes, first demonstrated by Robert Hall in 1962[10]. Later developments to produce a stable, room temperature operated diode with a practical working lifetime were reached in 1977 at Bell Laboratories[11], when they produced a gallium-arsenide diode that they claimed could run for 100 years constantly at room temperature. With both of the limiting features solved for

fibre laser systems by the 1980's, the technology began to rapidly develop further.

With fibre systems being focussed on research within the telecommunications area, the invention of the Erbium Doped Fibre Amplifier (EDFA) in 1987[12], advanced the field even further. The EDFA operates in the C band around 1.55μ and displays desirable properties such as high gain, low noise and low threshold. This made it a revolutionary development within the telecoms industry. It allowed for the optical fibres to be operated at their lowest loss wavelength and allowed for large distance communication using the EDFAs in place of expensive repeaters, effectively amplifying the signal at various points along the transmission to account for the loss from the large propagation length through the optical fibres. With the development of the EDFA, other similar rare earth amplifiers were tested and developed, including those using ytterbium and thulium, to cover a large range of wavelengths.

1.3 Master Oscillator Power Amplifier (MOPA) Systems

A master oscillator power amplifier (MOPA) is a system whereby a low power seed laser is amplified, generally through multiple amplifier stages. MOPA systems are attractive as it is easier to control the properties of low power sources, therefore with a MOPA it is possible to obtain the high control a low power source offers while still being able to achieve high powers. The concept of a MOPA system can be realised with either free space components or a completely fiberised system, sometimes referred to as a master oscillator fibre amplifier (MOFA) or a master oscillator power fibre amplifier (MOPFA). Typically, a MOPA system will have three to four amplifier stages, although it can be designed with greater or fewer to meet specific needs.

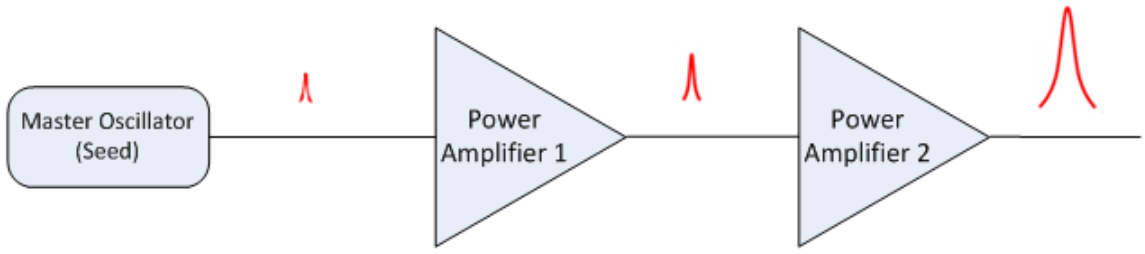

Figure 5: Basic design principle behind a master oscillator power amplifier set-up, beginning with a small controllable pulse and amplifying it multiple times

MOPA systems are designed as a method of scaling the output power of a laser system. Early MOPA systems used a solid state amplifier, however the technique was quickly adopted in fibre systems after the development of the erbium doped fibre amplifier (EDFA) in 1987. In addition, the end of the 80s saw the first double clad fibres (discussed in more detail in section 2.1.2) which aided in the power scaling potential.

An early example of a high energy pulsed MOPA system, relying solely on single cladding fibre, was shown by ORC in 1993 [13]. This MOPA was designed to operate at 1.5μm using erbium amplifiers. The system used here demonstrates the concepts of a MOPA, being able to tune and control the DFB source laser, over a range of pulse widths, while still reaching high pulse energies. One key aspect to note is the use of a large core final amplifier stage in order to store as much energy as possible. The addition of cladding pumped fibres took this principle to the extreme, with an 82mJ pulsed ytterbium MOPA system in 2004 [14]. The final stage of this MOPA was a 200μm core double clad fibre, providing huge potential for energy storage.

In an attempt to improve the performance of MOPA systems further, a great deal of work was focused on fiberising the entire system. This helped to reduce the losses obtained from free space coupling as well as making the system more robust. In 2009, a 2mJ fully fiberised system was presented [15]. Despite removing the need for free space coupling, it was impossible to use such a large core fibre, reducing the potential for energy storage. Another important aspect of this publication was the ability to shape the pulse. By using an

elector-optic modulator (EOM) it was possible to pre-distort the pulses, so that after amplification the result would be square, flat top pulses. This pulse shaping helps to increase the maximum pulse energy that can be obtained from a system.

Most recently in 2013, a fully fiberised 10mJ MOPA system was realised [16]. With developments in fibres and corresponding components, it was possible to have a final amplifier stage with a 50μm core without the need for any free space components.

1.4 Frequency Conversion

Frequency conversion is a powerful tool in optics, as it gives access to wavelengths that are typically difficult to reach. The use of non-linear crystals is a common and relatively easy way to produce these desired wavelengths. Harmonic generation can be used to generate wavelengths that are integer factors smaller than the fundamental source used. With a 1μm pump source, the second harmonic produced is around 500nm, while the third harmonic is at 333nm. The generation of these low harmonic waves can be obtained via second and third harmonic generation within non-linear crystals. These processes rely on the non-linear susceptibility of the chosen crystals. Typically direct third harmonic generation will have a low efficiency due to the small third order susceptibility (typically $\sim$ x$10^{-22} m^2/W$ [19]), therefore more often, the third harmonic is generated via sum frequency generation, where the fundamental and second harmonic waves are combined to produce a wave at the sum of their frequencies, i.e. three times the frequency of the fundamental.

Soon after the discovery and invention of the laser, people began experimenting with various media in an attempt to further explore the new possibilities open to them with the intense and coherent light now available from lasers. With new power levels being reached, people were able to record results from different media that no longer demonstrated a linear response. This led to the realisation of theoretical explanations of non-linear effects, such as second harmonic generation, first described in 1962 by N. Bloembergen and P. S. Pershan [20].

A significant amount of current laser systems rely on borate crystals to perform non-linear conversions, such as lithium triborate and barium borate. The majority of these crystals were first discovered and applied to non-linear optics by the Fujian Institute of Research on The Structure of Matter, Chinese Academy of Science [21] [22]. With the development of these crystals, the possibility of non-linear conversions became significantly easier, and many different experiments were conducted to investigate the various opportunities now available [23] [24] [25].

1.5 Motivation and Aims

The work carried out in this thesis is important in supporting the development of photoacoustic imaging devices. With current systems being limited in development by the size of the required laser source, the main focus of this research is to produce a compact laser system based on optical fibre that is both portable and can produce comparable or improved results in terms of image quality and speed of acquisition to the current solid state laser system used.

The majority of earlier and existing photoacoustic scanners have been laboratory proof-of-concept experiments [41][42][43], aiming to show the feasibility of such a system. However; the aim of this project is to translate the concept into a usable imaging system, with practical applications within a clinical environment, and to aid additional research in the field of life sciences. A major challenge in advancing the development of a practical solution is the laser source used. Current laser sources used in PA imaging are typically large and bulky, unstable, and lack sufficient control over the temporal output. This makes them unsuited to being used as practical clinical tools.

There are two main modes of operation for a PA imaging system, photoacoustic tomography (PAT) and optical resolution photoacoustic microscopy (OR-PAM). PAT uses a large beam to irradiate a significant, if not the entire, volume of the sample tissue. On the other hand, OR-PAM uses a tightly focussed beam that is scanned over the target volume. Generally, PAT is a more flexible and widely applicable mode of operation, with potential uses in both clinical and pre-clinical environments. OR-PAM is more frequently used in pre-clinical

situations for ultra-high resolution images.

Together with University College London (UCL) the University of Southampton (UoS) jointly submitted a proposal, which was accepted and funded by EPSRC. The overall aim of the project is to combine the UoS expertise in fibre laser systems with the photoacoustic imaging specialism of UCL to develop portable, table-top OPO systems that can be used both in photoacoustic tomography (PAT) and optical resolution photoacoustic microscopy (OR-PAM). Specifically two main systems will be targeted, one for each of the photoacoustic imaging operational modes. The PAT system should be tunable between 650-1050nm delivering milli-Joule pulse energies at a pulse repetition rate of 1kHz. The OR-PAM system is required to operate at a higher repetition rate, in the order of 500kHz, with a tunable wavelength range between 450-700nm. Both systems will ideally have tunable pulse widths ranging from 0.5-50ns for OR-PAM and 1-500ns for the PAT system. In order to achieve these goals, throughout the project novel fibres and excitation schemes will need to be developed and tested.

My MPhil project will mainly be focused around the design and development of the OR-PAM system, working on being able to deliver a compact system capable of producing milli-Joule pulses within the visible spectrum. The large majority of the fibre development will take place within the ORC. Two independent systems will be developed, enabling a test system to be transported to UCL for testing and evaluation with a variety of existing PA imaging scanners, whilst the other system can remain at the ORC for further developments.

Successfully attaining the project goals will widely benefit the scientific community. The development of a novel, suitable, compact laser source will enable the development of portable PA imaging systems for specific biomedical applications, as well as aiding further research within the PA field. The developments in the fibre lasers may also have an impact on other biomedical optical imaging methods and systems. There is also a great deal of non-medical potential with the development of the fibre laser system. The high energy pulses and accessible large wavelength range could be of interest within the material processing field, and may even impact research and work based on laser driven fusion.

1.6 Thesis Outline

The content of my thesis is structured as follows:

Chapter 3 presents the theoretical background to the main components of my research, ytterbium fibres, fibre non-linearities and frequency conversion. Within the section on ytterbium fibres, details on the suitability of ytterbium are presented, as well as theoretical descriptions of optical fibres. Next, fibre non-linearities are discussed, focusing on self-phase modulation (SPM), stimulated Brillouin scattering (SBS) and stimulated Raman scattering (SRS) as the most relevant to the work presented. The final section explains the principles of second order frequency conversion, re-enforcing the need for phase matching within these processes.

Chapter 4 discusses work on developing a suitable system for photoacoustic tomography. An initial hybrid fibre and free space system was developed and the construction of the system is explained, along with the steps taken to increase the output pulse energy of the system. A second portable system derived from the first is detailed, describing the system set-up and the similarities and differences between itself and the initial system design. Maximum output data from the two systems is presented and the suitability of the systems discussed.

Chapter 5 looks in detail at the work carried out on developing a suitable system for optical resolution photoacoustic microscopy. The initial system set-up is described, along with the modifications made to improve the performance, and aid in making the system portable. Significant work is presented on choosing a suitable seed design, looking into various locking techniques such as fibre Bragg gratings, and injection locking.

Chapter 6 focuses on second harmonic generation, discussing the choice of crystals available, and why the chosen one was selected. It also details theoretical calculations of the phase matching conditions required and presented, along with experimental results of the conversion process.

Chapter 7 highlights the conclusions of the work, presenting key findings and results from the research. Suggested further work is discussed, focusing on additional frequency conversion stages able to produce the required frequency range for an operational OR-PAM system.

2 Background / Theory

This chapter discusses the background theory of the main components of my research. Section 2.1 details the properties of ytterbium, as well information about optical fibres and how they work. Section 2.2 looks closely at the main fibre non-linearities and how they are generated within a fibre system. Section 2.3 explains how non-linearities within crystals can be used to generate new frequency components in both second harmonic generation and optical parametric oscillators.

2.1 Ytterbium Doped Fibre Amplifiers

2.1.1 Ytterbium Properties

Ytterbium is a very flexible rare earth ion when combined with a silica host material. This is mainly due to its significant gain bandwidth, spanning from 975nm - 1200nm[26]. Ytterbium has a very simple energy level scheme compared with other rare earth elements used in gain media. Ytterbium simply has one excited energy state ($^2F_{\frac{5}{2}}$) that can be reached from the ground state ($^2F_{\frac{7}{2}}$) by absorbing a pump photon. However, both of these two states are stark split into additional sub-levels, shown in figure 6.

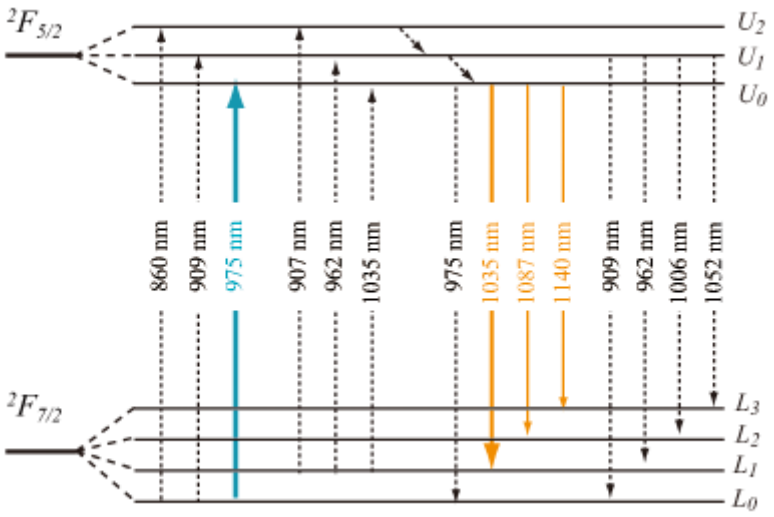

Figure 6: Energy level diagram for ytterbium, showing the split ground and split excited states. Image taken from Optipedia [44]

Figure 7 shows both the absorption and emission cross sections for ytterbium doped germanosilicate glass (commonly used for YDFAs). The absorption cross section indicates that using pump diodes at around 915nm, or 975nm will be strongly absorbed and thus will efficiently invert the fibre. The absorption at 975nm is significantly higher than that at the lower wavelengths, but in turn is much narrower. Due to the smaller absorption cross section, pumping at 915nm is less efficient than at 975nm. Therefore, to achieve the same output power, the amplifier must be longer if 915nm is the selected pump wavelength. Furthermore, due to the strong emission at 975nm being almost equal to the absorption, the population of the upper level is limited to around 50%, whereas an upper state population in excess of 90%[26] can be obtained with strong pumping at shorter wavelengths.

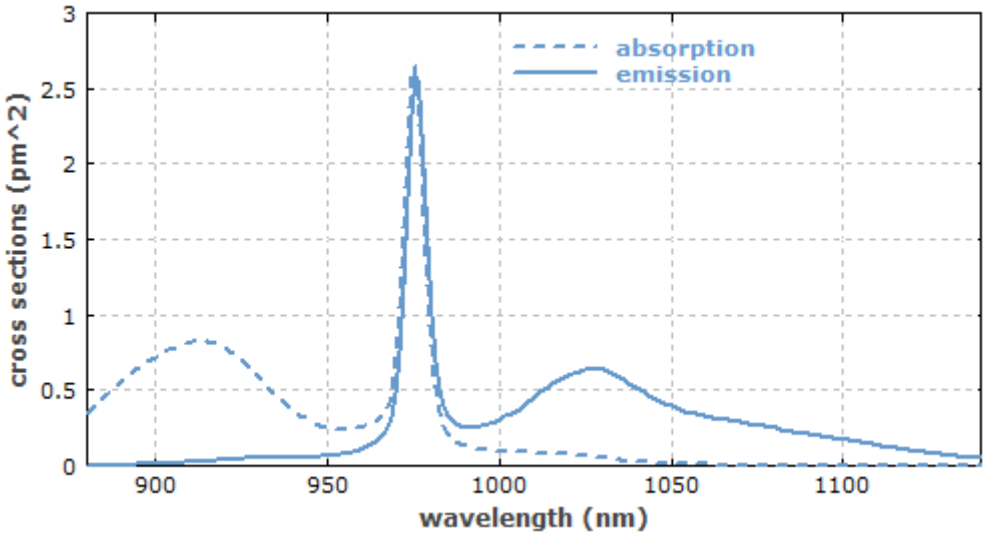

Figure 7: Absorption and emission cross section for ytterbium-doped germanosilicate glass. Image taken from RP Photonics Encyclopaedia [27]

2.1.2 Optical Fibres

Optical fibres have developed significantly since they were first created, but the general principle and design remains the same. The basic structure of an optical fibre consists of three main sections, the core, the cladding and the jacket. The core and cladding sections of the fibre make up the waveguide, while the jacked is applied for protection.

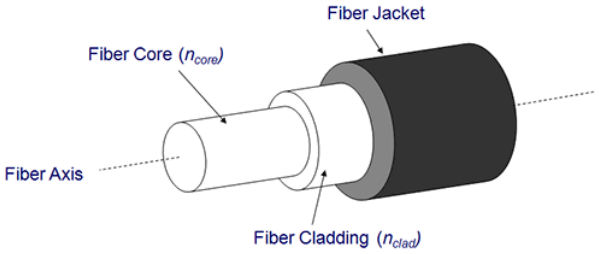

Figure 8: Basic structure of a standard optical fibre. Image taken from Fibrecomms[28]

By surrounding the core material with a lower refractive index cladding material, the light is constrained to propagate in the core due to the phenomena of total internal reflection. As long as the angle at which the light is incident upon the core-cladding interface is greater than the critical angle, the light will be completely reflected back along the fibre core. The critical angle can be related to the difference in the refractive index of the core and cladding materials.

$$\theta_C = sin^{-1}\left(\frac{n_{clad}}{n_{core}}\right) \tag{1}$$

Due to the critical angle requirement, there is a limit on the angle at which the light enters the fibre. This acceptance angle can be defined through the numerical aperture of the fibre, shown in figure 9.

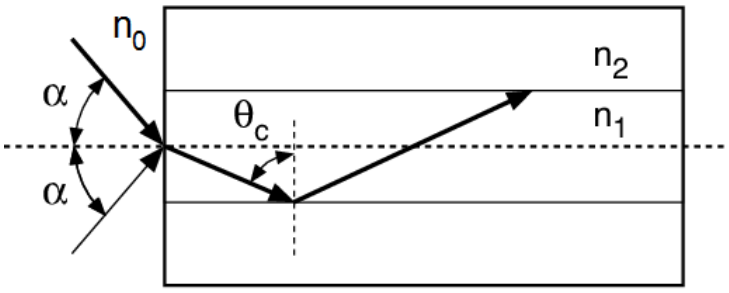

Figure 9: Diagram showing the geometrical requirements for light to propagate along the length of the fibre. 2α represents the full acceptance angle of the fibre, θ_C the critical angle and n_1 and n_2 the refractive index of the core and cladding respectively. Image taken from Newport[17]

Generally, the acceptance angle of a fibre will be referred to through the numerical aperture, which can be defined as,

$$NA = n_0 sin\alpha = \sqrt{n_{core}^2 - n_{clad}^2} \tag{2}$$

By adjusting the relative differences between the refractive index of the core and the cladding, it is possible to adjust the numerical aperture of the fibre. The direct impact of adjusting the numerical aperture of a fibre, is that with a larger NA, it becomes easier to couple more light into the fibre. The drawback of having a higher NA is that there will be an increase in scattering loss, due to the higher dopant concentrations required. The tuning of the NA will also have an impact upon the normalised frequency parameter, also known as the V number. The V number can be used as an indication of the number of modes that a fibre will support.

$$V = \frac{2\pi a}{\lambda} \cdot NA = \frac{2\pi a}{\lambda} \cdot \sqrt{n_{core}^2 - n_{cladding}^2} \tag{3}$$

where a is the radius of the fibre core.

For the case where, V $\leq$ 2.405, only a single mode is supported and propagated by the fibre. Single mode guidance is often desired, as the output of the system can be maintained as near to diffraction limited as possible. Additionally, for applications such as communications, single mode propagation is required to prevent modal dispersion which, otherwise would prevent high transmission rates.

One concern with fibre systems is that the output beam has a random polarisation. This can be an issue where a single polarisation is required, such as frequency conversion. Due to inhomogeneity, or mechanical stress, a fibre will always show some level of birefringence. Moreover, this variation will not be consistent along the whole length, and will result in the polarisation changing along the fibre in an uncontrolled manner. Any fluctuation or changes to the bending or temperature of the fibre will further affect the final polarisation observed at the output. This problem can be avoided by using polarisation maintaining (PM) fibres. PM fibres solve this by creating a high birefringence environment through the inclusion of two stress rods within the fibre.

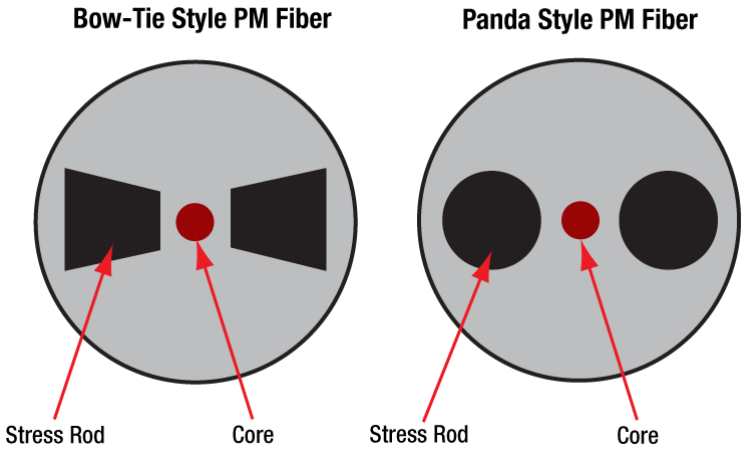

Figure 10: Two polarisation maintaining (PM) fibre designs using stress rods to induce large birefringence along the fibre lengths, minimising fluctuations between polarisations. Image taken from Thorlabs[29]

With a larger birefringence along the fibre length due to the stress rods, the two polarisations now have a more significant difference in their propagation constants. This causes the phase of the two propagating polarisations to differ. This in turn results in needing a larger disturbance to the fibre, such as bending or heating, to couple the two polarisation modes together. Using a PM fibre ensures the input polarisation will be retained over the length of the fibre to the output. However, this relies on the light entering the fibre being polarised along one of the birefringent axes.

Early rare earth doped fibres followed the same structure as a standard optical fibre shown in figure 8. The central core of the fibre would be doped with the chosen rare earth element such as erbium or ytterbium. Ensuring that the cladding has a lower refractive index guarantees guidance down the fibre length. In general, a third layer is also added to the fibres; this coating layer is used as additional protection from shock and excessive bending. This outer coating is formed using a polymer which will have a refractive index higher than that of the fibre cladding layer. To benefit from the rare earth dopant within the fibre core, the fibre must be pumped at a suitable wavelength simultaneously to the signal being passed through. In order to couple both the signal and pump through the core of the fibre, a wavelength division multiplexer (WDM) is used.

A fibre coupled WDM is a specific example of a fused fibre coupler. These devices are used to couple power from one fibre to another. The device is constructed by bringing the cores of two parallel fibres close together such that the evanescent wave from one leaks into the other. By adjusting the distance between the cores and the interaction length, it is possible to completely transfer the power from one fibre to the other. By further increasing the length, the power will begin to transfer back to the initial fibre. By adjusting the length, a tap coupler with any given tap ratio can be manufactured. In the case of WDMs, the transfer of power is dependent upon the wavelength, and therefore to couple both wavelengths simultaneously into one fibre, the component must be made a specific length, and will only retain the exact transfer ratio for the designed wavelength. This can be seen in figure 11 which shows an example of the power in one of the output fibres for two input wave-

lengths.

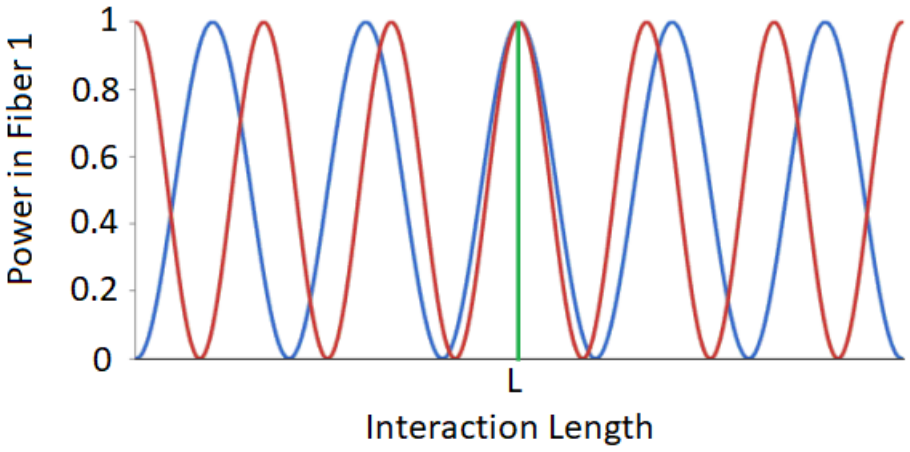

Figure 11: Output power of a WDM for an increasing interaction length for two different input wavelengths. The interaction length L is where both wavelengths are completely coupled into one fibre simultaneously. Image taken from Newport[30]

WDMs are used within core pumped amplifier set-ups, as both the signal and pump wavelengths are coupled into a single fibre core at the output of the WDM. Due to the need for the pump to propagate through the core of the fibre, it is required to be single mode. This heavily limits the available pump power that can be used in this configuration to typically sub-watt levels.

In 1989 a solution to this limited pump power was realised by James Kafka[31]. The new cladding pump set-up was designed to allow the use of high power multimode pumps, capable of hundreds of Watts of power. Despite the use of multimode pumps, it is still possible, using this pumping scheme to obtain a single mode signal output. In order to use a cladding pump set-up, a different fibre configuration is required. As shown in figure 12, a second cladding layer is applied to the fibre with a refractive index lower than both that of the core and the inner cladding layers. These fibres are referred to as double clad fibres (DCFs).

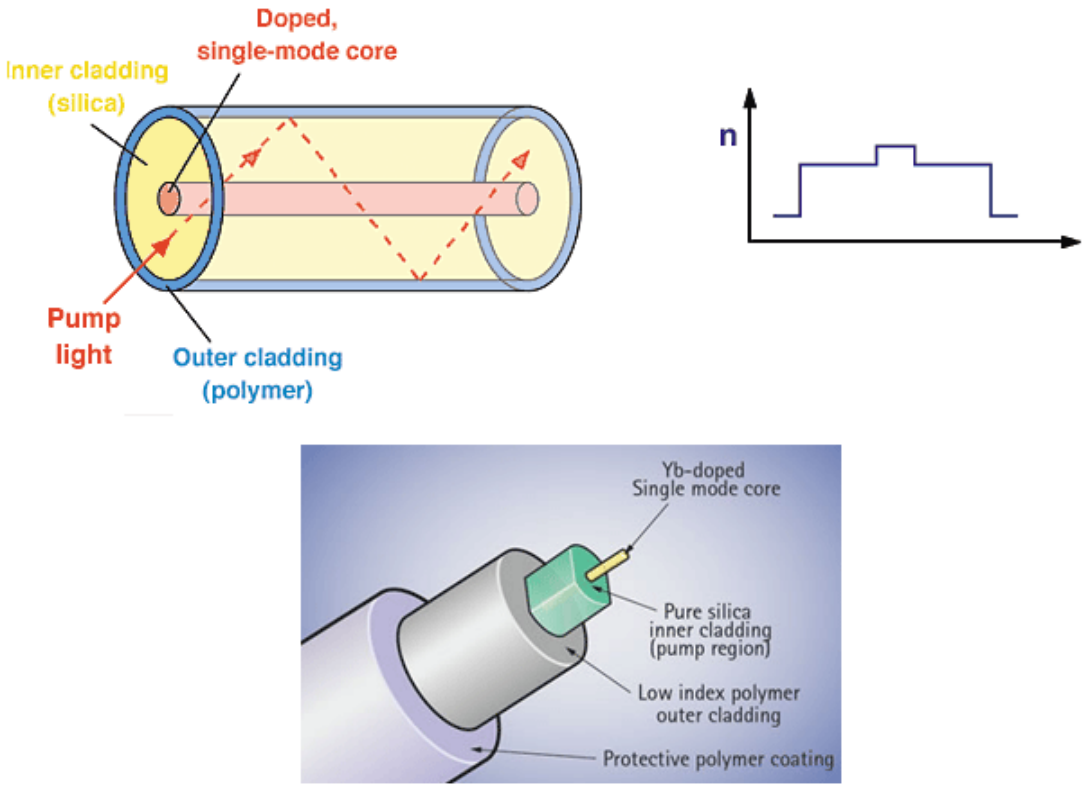

Figure 12: Diagram showing the main sections of a double clad fibre (DCF). Image taken from Coherent[32]

Unlike the core-pumped case, the multimode pump light is now coupled into the inner cladding of the double clad fibre, and experiences total internal reflection from the interface between the inner cladding and outer cladding. Due to the pump being multimode, the pump light overlaps the core at various points along the length of the fibre. To help increase the overlap of the pump modes with the fibre core, the shape of the inner cladding can be altered to help break the circular symmetry. Various cladding shapes can be used, some of the more common are shown in figure 13. Despite this, the absorption will still be lower than that of the core-pumped case, thus, using double clad fibres requires a longer device length to compensate. Typically, power amplifiers will use DCF as they allow for high pumping powers. Some core-pumped amplifiers may be used early on within the system, as pre-amplifiers, designed to overcome losses from modulators and fibre components.

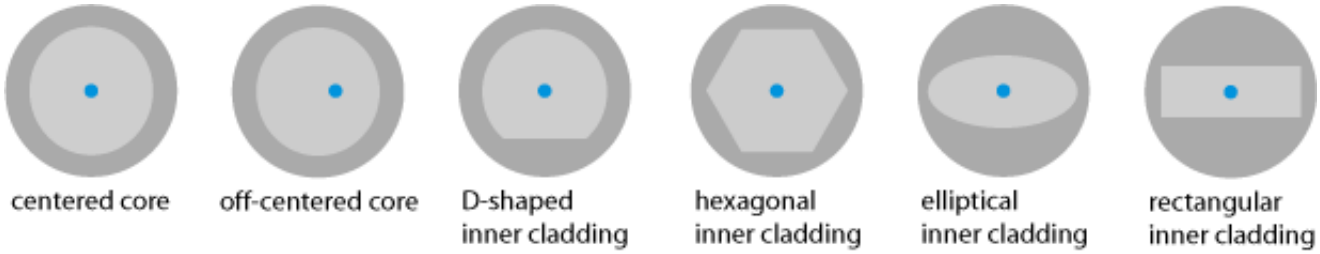

Figure 13: Different DCF shapes used to break the circular symmetry, increasing the overlap of the pump with the fibre core. Image taken from RP Photonics[27]

With the high pump power that is available when using DCFs, it is possible to reach high signal peak powers within the fibre core. This can result in the onset of non-linearities within the fibre, such as self-phase modulation (SPM), stimulated Brillouin scattering (SBS) and stimulated Raman scattering (SRS). To solve this problem, large mode area (LMA) fibres were developed. LMA fibres rely on increasing the core size within the fibre, increasing the threshold for non-linear effects. It is possible, up to a point, to keep these LMA fibres single mode, by reducing the NA, such that the V number of the fibre remains below 2.405. However, the NA can only be decreased so much before the guidance along the fibre becomes weak, and bend losses become significant. By further increasing the size of the core beyond the single mode regime, the beam quality of the output will begin to decrease. In some situations, the higher peak powers obtained are more beneficial and can be an advantageous trade-off. However, there are cases where the beam quality must be as close to diffraction limited as possible. In this case, it is possible to carefully bend the LMA fibre to a point where higher order modes become lossy, while the fundamental mode remains unaffected. This provides the advantage of both higher powers and a good beam quality, but can only be utilised when only a few modes are supported by the fibre, limiting the size of the core, typically to below $25\mu m$.

Usually with fibre laser systems, it is beneficial to have a fully-fiberised system, especially when linking multiple amplifiers together. This provides a more reliable and stable system as the other option is to free space end-pump the fibres. A free space set-up relies on mechanical fibre mounts, dichroic mirrors and lenses. An example set-up is shown in figure 14. Due to the manual alignment of the fibres and lenses, temperature changes and external vibrations can affect the output, and lead to instabilities.

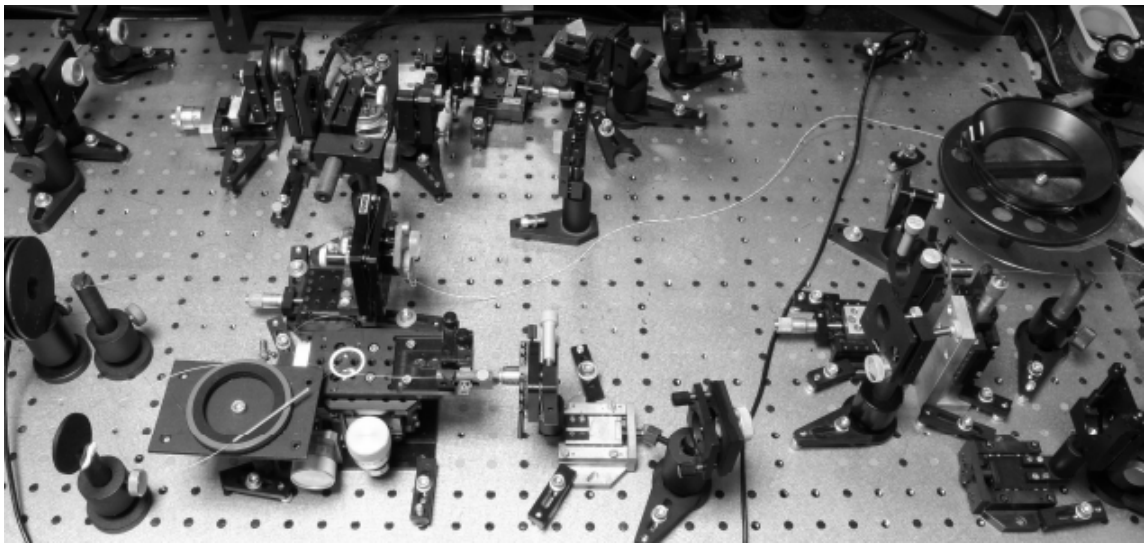

Figure 14: Hybrid bulk/fibre MOPA system. Image taken from SPIE[33]

A fully-fiberised system can be achieved with the use of pump combiners. These work in a similar manner to WDMs, combining multiple inputs into one output fibre. These combiners consist of a bundle of coreless fibres, which are used to couple pump light in from multimode pump diodes, surrounding a central signal fibre. The bundle is then tapered down and spliced to a DCF that matches the size of the desirable rare earth doped fibre. The DCF will guide the signal through the core, while the inner cladding will guide the pump, coupling them both into the active fibre. For high pump power, additional coreless fibres are added to the bundle before tapering; typically, combiners come with 2 or 6 pump fibres.

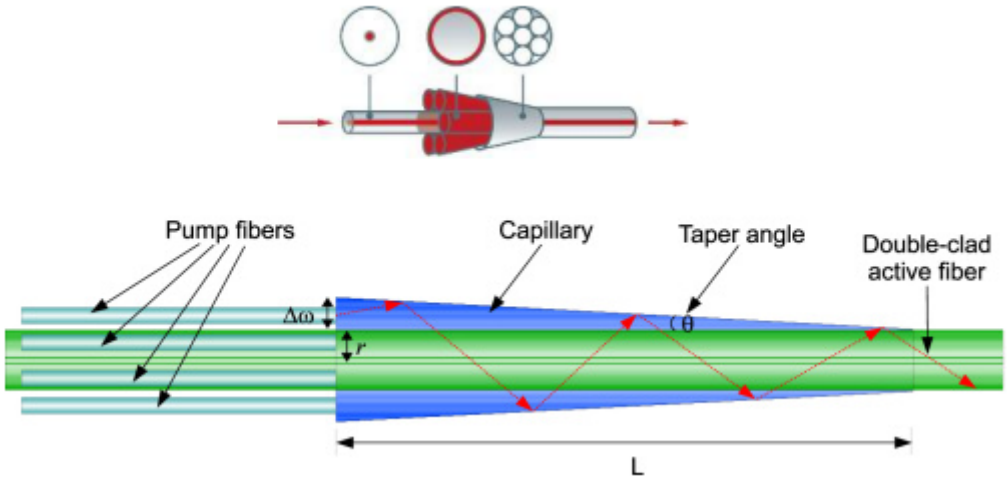

Figure 15: Schematic drawing showing how a pump combiner works. Image taken from OSA[34]

2.2 Fibre Non-linearities

Normally, when an electric field is applied to a dielectric medium it induces electric dipole moments. These dipole moments manifest themselves in the polarisation density. If a weak field is applied, then this response will be linear, such that the polarisation is given by equation 4.

$$\mathbf{P} = \epsilon_0 \chi^{(1)} \mathbf{E} \tag{4}$$

where $\mathbf{P}$ is the polarisation, ϵ_0 is the permittivity of free space, $\chi^{(1)}$ is the linear susceptibility and $\mathbf{E}$ is the electric field.

The linear susceptibility of a material is related to its refractive index by the expression:

$$\chi^{(1)} = n^2 - 1 \tag{5}$$

However, if the incident electric field is very intense, then the polarisation is no longer linear, and can instead be expressed as a Taylor expansion of the electric field.

$$\mathbf{P}(t) = \epsilon_0 [\chi^{(1)} \mathbf{E}(t) + \chi^{(2)} \mathbf{E}^2(t) + \chi^{(3)} \mathbf{E}^3(t) + ...] \tag{6}$$

where $\chi^{(1)}$, $\chi^{(2)}$ and $\chi^{(3)}$ are the linear, second-order and third-order susceptibilities respectively.

In the case of silica fibres, there is no second-order susceptibility. This is due to the fact that silica is a glass, which are centrosymmetric. Thus the lowest order of non-linearity that can arise in a silica fibre is from the third-order susceptibility ($\chi^{(3)}$). The $\chi^{(3)}$ can be separated into two general processes, elastic and inelastic. For elastic interactions, the energy of the incident photon is conserved, whereas in inelastic scattering, the energy of the incoming photon is either increased or decreased. The main cause of the elastic interactions arises from the Kerr effect. The Kerr effect alters the refractive index of the medium and is proportional to the intensity of the light passing through it. This power dependant refractive index can produce non-linear effects such as self-phase modulation (SPM) and cross-phase modulation (XPM). The inelastic scattering non-linearities are usually identified by the generation of new frequency components, as seen in Raman and Brillouin scattering.

2.2.1 Self-Phase Modulation

If an optical pulse propagates through a medium, then due to the Kerr effect, there is a non-linear change to the refractive index of the material, induced by the applied electric field. This non-linear refractive index can be described by equation 7

$$n = n_0 + n_2 I(t) \tag{7}$$

Where n_0 is the refractive index of the core with no incident light, n_2 is the non-linear refractive index coefficient and I is the intensity of the incident light.

Given the phase change of a pulse along a length L of fibre is expressed as,

$$\phi(t) = nk_0L = (n_0 + n_2 I(t))k_0L \tag{8}$$

where $k_0 = \frac{2\pi}{\lambda}$

Then the non-linear phase change that is generated through the Kerr effect can be described as:

$$\phi_{NL}(t) = n_2 k_0 L I(t) \tag{9}$$

The non-linear Schrödinger equation can be simplified in the case where pulses are in the non-linearity dominated region, as $L_D \gg L_{NL}$. In this case, the dispersion effects can be removed, resulting in,

$$i\frac{\partial A}{\partial t} + \frac{1}{2}\frac{\partial^2 A}{\partial x^2} + \gamma|A|^2 A = 0 \qquad \longmapsto \qquad i\frac{\partial A}{\partial z} + \gamma|A|^2 A = 0 \tag{10}$$

The solution of this can be expressed as:

$$A(L,t) = A(0,t)e^{i\phi_{NL}(t)} \tag{11}$$

where $\phi_{NL}(t) = \gamma L|A(0,t)|^2$

This non-linear phase change will impact the pulse by increasing its spectral width, through the relationship:

$$\delta\omega(L,t) = -\frac{\partial\phi_{NL}(t)}{\partial t} = -\gamma L\frac{\partial|A(0,t)|^2}{\partial t} \tag{12}$$

The overall impact of injecting a high intensity beam through a fibre is that, as the power increases, a larger chirp will be observed. This could be potentially detrimental to the system if a particular spectral bandwidth is required at the output of the system.

2.2.2 Stimulated Brillouin Scattering

When incident light propagating through a fibre exceeds a certain threshold power, an acoustic wave is generated via the process of electrostriction. This acoustic wave modulates the refractive index along the fibre and forms a moving index grating, travelling at the acoustic velocity v_a. The incident light is then partially back scattered via Bragg diffraction. The frequency of the reflected photons is downshifted slightly due to the Doppler shift arising from the moving index grating. This shift in frequency, shown in equation 13, can be used to identify the scattered photons as being generated through SBS.

$$\nu_B = \frac{2nv_a}{\lambda} \tag{13}$$

where ν_B is the Brillouin frequency shift, n is the refractive index, v_a is the acoustic velocity and λ is the vacuum wavelength.

The generated Stokes wave grows as it propagates backwards along the fibre following the Brillouin gain spectrum g_B. The Brillouin gain spectrum has a relatively small spectral width, of around 50-100MHz[27], compared with the width of the Raman gain spectrum at around several terahertz[35]. This is due to the strong absorption

of the acoustic waves, leading to a short phonon lifetime of around 10ns. The peak value of the gain spectrum, g_p can be assumed to be independent of the operating wavelength, and in a standard silica fibre, has a value of approximately, $g_p \approx 5 \times 10^{-11} m/W$[18]. This approximation is assuming a near CW pump and thus for a pulsed system, where the pulse width is shorter than the lifetime of the phonons, the value of the Brillouin gain is significantly reduced. Additionally, the gain is also affected by the linewidth of the pump source. Increasing the linewidth of the pump beyond that of the Brillouin gain will result in a significant decrease in the amplitude of the gain. Other factors that can affect the gain are fibre properties such as inhomogeneities in the fibre core diameter or levels of doping along the fibre length.

SBS can arise at a particularly low threshold power, and is generally one of the more dominant non-linear affects within fibre systems. The Stokes wave will generally be generated through spontaneous Brillouin scatter and grow in amplitude as an incident power is applied to the fibre. The threshold for SBS occurs when the critical power condition is reached. The critical power for SBS is defined as the power level at which the Stokes wave at the input end of the fibre is equal to that of the pump power at the output end of the fibre, and can be expressed as:

$$P_{B.critical} = 21\frac{A_{eff}}{g_B L_{eff}} \tag{14}$$

Where A_{eff} is the effective core area of the fibre, g_B is the peak value of the Brillouin gain and L_{eff} is the effective length.

The effective length of a fibre is defined as the length over which the power can be assumed to be constant, as over a long length of fibre the attenuation will slowly reduce the power,

$$L_{eff} = \frac{1 - e^{-\alpha L}}{\alpha} \tag{15}$$

where α is the attenuation coefficient.

Similarly, with the area of the fibre, the intensity will not be uniform over the fibre area. Therefore, to take account of this, the effective area is used, which is defined as,

$$A_{eff} = \frac{\int_r \int_\theta r dr d\theta I(r,\theta)}{\int_\theta \int_r r dr d\theta I^2(r,\theta)} \tag{16}$$

2.2.3 Stimulated Raman Scattering

Stimulated Raman Scattering is another scattering process, based around the interaction between the incident light and optical phonons. This interaction converts a single pump photon into a photon of lower energy and a phonon that carries away the excess energy. Unlike the Brillouin gain, the Raman gain extends over 30 THz, with the first peak in silica being at a 13THz shift from the pump frequency. The gain peak for Raman is approximately, $g_R = 1 \times 10^{-13} m/W$ which is around a factor of five hundred times smaller than that of the Brillouin gain. This in turn leads to a significantly higher Raman threshold, which can be determined using equation 17.

$$P_{R.critical} = 16\frac{Aeff}{g_R L_{eff}} \tag{17}$$

Where A_{eff} is the effective core area of the fibre, g_R is the peak value of the Raman gain and L_{eff} is the effective length.

Both SBS and SRS can be highly detrimental to a fibre system, although either can be used in a specific set-up to generate useful signals, such as in a Raman laser. Generally, given the significantly lower threshold for SBS, this is the limiting case for the maximum power achieved in a fibre amplifier. However, there are cases where using particularly short pulses, in the order of 1ns, where the SBS threshold becomes higher than that of SRS.

2.3 Second Order Non-linear Processes in Crystals

As described in section 2.2 non-linear effects are due to the higher order susceptibility of a material. Unlike silica fibres, the non-linear crystals discussed here are not centrosymmetric and therefore will have a non-zero second-order susceptibility $\chi^{(2)}$. This $\chi^{(2)}$ gives rise to various effects such as second harmonic generation (SHG), sum frequency generation (SFG) and difference frequency generation (DFG). The non-linear effects that will be discussed in this thesis concentrate on the condition where there are two input photons. By looking specifically at the second-order component of the non-linear polarisation, and substituting a general equation for the E field containing two arbitrary frequency components ω_1 and ω_2, the second-order polarisation can be described by equation 20

$$P^{(2)}(t) = \epsilon_0 \chi^{(2)} E(t)^2 \tag{18}$$

$$E(t) = E_1 e^{-i\omega_1 t} + E_2 e^{-i\omega_2 t} + c.c \tag{19}$$

$$P^{(2)}(t) = \epsilon_0 \chi^{(2)} \left[E_1^2 e^{-2i\omega_1 t} + E_2^2 e^{-2i\omega_2 t} + 2E_1 E_2 e^{-i(\omega_1+\omega_2)t} + 2E_1 E_2^* e^{-i(\omega_1-\omega_2)t} + c.c\right] + 2\epsilon_0 \chi^{(2)} \left[E_1 E_1^* + E_2 E_2^*\right] \tag{20}$$

Each term in equation 20 corresponds to a different non-linear process. The first and second term both display SHG, one with an output at ω_1 and the other at ω_2. The third term, $2E_1 E_2 e^{-i(\omega_1+\omega_2)t}$ represents the SFG; this can be seen in the exponent term which contains $\omega_1 + \omega_2$. The fourth term represents difference frequency generation where the generated frequency is at $\omega_1 - \omega_2$. The final term represents optical rectification as it has no dependence upon the frequency. Despite multiple non-linear terms being present, only one process will dominate with substantial power output due to different phase matching conditions.

2.3.1 Phase Matching

When attempting to obtain a high conversion efficiency for second-order non-linear processes, it is important for it to meet the phase matching condition. This is where the sum of all the phases equates to zero.

$$\Delta k = k_a - k_b - k_c \tag{21}$$

$$\text{where} \qquad k_i = \frac{2\pi n_i}{\lambda_i} \tag{22}$$

where k_i is the wave vector, n_i is the refractive index and λ_i is the wavelength of the corresponding waves (i = a, b, c).

If the phase matching condition is not reached, then the generated frequency will be converted back to the fundamental over the coherence length. Typically, the efficiency of non-phase matched processes are several orders of magnitude lower than when they are phase matched.

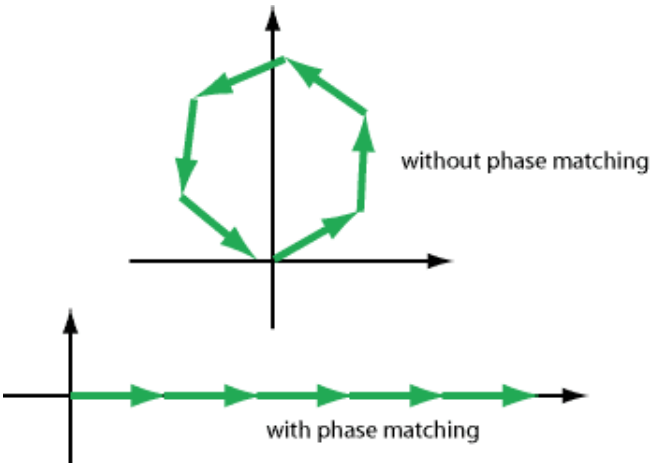

Figure 16: Phasor diagram representing the difference between a phase matched ($\Delta k = 0$) and non-phase matched ($\Delta k \neq 0$) system. Showing the addition of various SHG contributions from along the length of the crystal [27]

The phasor diagram in figure 16, shows that without phase matching the periodic shift in the phase leads to only a small generated second harmonic power that oscillates over the length of the crystal. Whereas when the phase matching condition is met, each component adds up constructively, resulting in an increasing power over the length of the crystal. A phase mismatch has a strong negative effect on the conversion efficiency obtained for the SHG process. This effect can be described by the phase mismatch factor[36], $sinc^2(\frac{\Delta kL}{2})$, which has been plotted in figure 17. Figure 17 clearly shows that a small increase in Δk will result in a significant decrease in the value of the phase mismatch factor which directly affects the efficiency obtainable. To achieve the phase matching conditions, we rely mainly on the birefringent properties of certain materials.

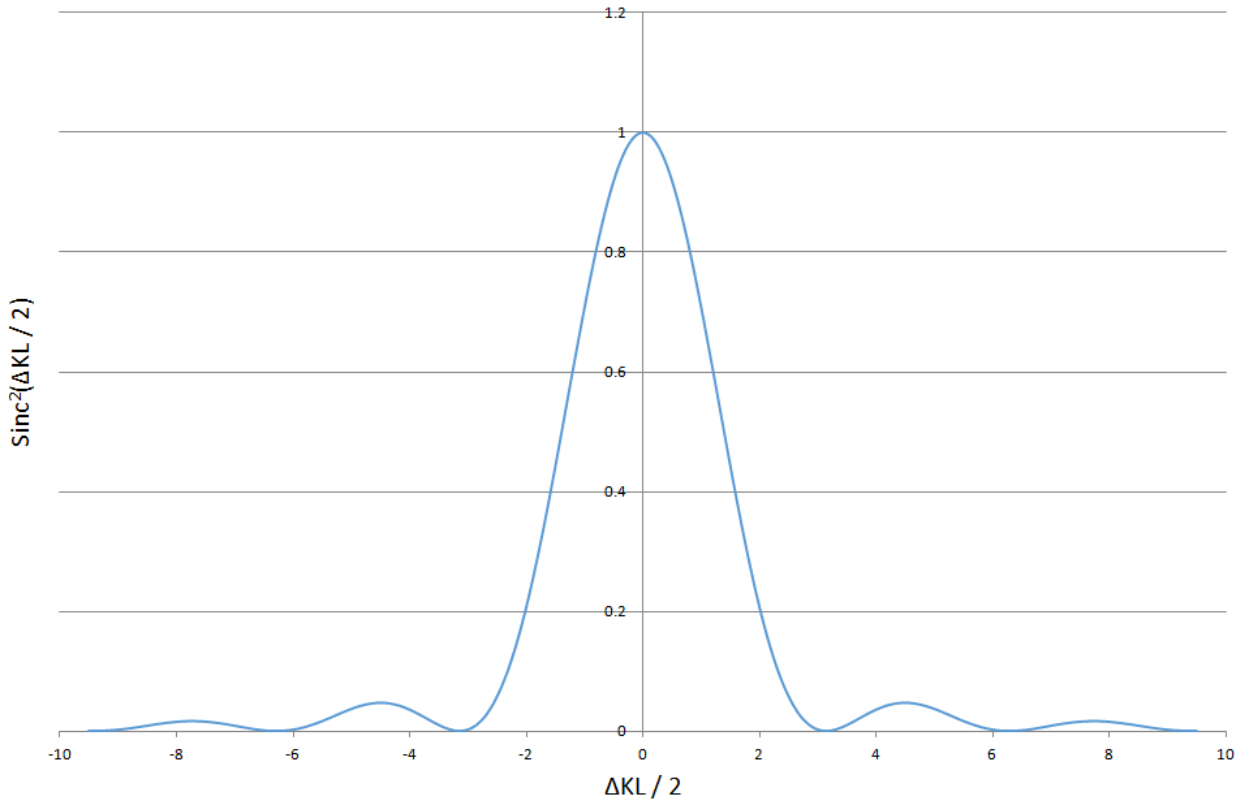

Figure 17: Plot of the phase mismatch factor, indicating the importance of phase matching to reach high conversion efficiencies

Birefringent phase matching (BPM) relies on tuning the temperature or angle of the crystal to access suitable refractive indices for both the ordinary and extraordinary polarisations in order to satisfy the phase matching condition. BPM can be be used to phase match the second harmonic generation (SHG) process. In this case, we have an input beam to the crystal at the fundamental frequency ω and generate the second harmonic which has a frequency 2ω. The phase matching condition for SHG is:

$$\Delta k = k_\omega + k_\omega - k_{2\omega} = 0 \qquad \rightarrow \qquad 2k_\omega = k_{2\omega} \tag{23}$$

which simplified to:

$$n(\omega) = n(2\omega) \tag{24}$$

after substituting in the value of k from equation 22 for the corresponding frequencies.

Typically, this condition would not be feasible in a normal dispersive material, as with an increase in frequency the refractive index would also increase. However, in birefringent materials, the refractive index is different for different polarisations of light propagating through the medium. These are referred to as the ordinary and extraordinary polarisations which have the corresponding refractive indices n_o and n_e. By adjusting the temperature and/or the angle of the crystal, it is possible to reach the condition where the $n(\omega) = n(2\omega)$ is satisfied, where the fundamental and second harmonic waves are polarised in the extraordinary and ordinary directions respectively, for a negatively birefringent crystal (where $n_0 > n_e$).

There are two options for the polarisations to achieve phase matching for SHG. The two fundamental waves can have either the same polarisation, known as type I, or perpendicular polarisations, known as type II. For a negatively birefringent crystal type I phase matching, the input signals must be polarised along the extraordinary axis and the output second harmonic will be produced with the ordinary polarisation. Type II, using the same crystal material, would need to be orientated such that one input was aligned with the extraordinary and one with the ordinary polarisations, and would produce an output along the extraordinary polarisation.

Generally, where possible, temperature tuning the crystal to reach the phase matching condition is desirable. This is due to the fact that as the angle is adjusted away from 0° or 90° there is a spatial walk-off between the interacting beams. This arises from the Poynting vector and the direction of propagation no longer being parallel for the extraordinary wave. As a result of the waves walking-off from each other, the interaction length is reduced, and in turn the efficiency obtained. When temperature tuning, the crystal can remain at an angle of 90° while the phase matching condition is still met. This special case is known as non-critical phase matching (NCPM).

2.3.2 Optical Parametric Oscillator

Although difference frequency generation (DFG) can be thought of in the same manner as SFG, it is more commonly considered as an optical parametric amplification (OPA) process. In this case, one signal photon entering the crystal causes the annihilation of a single high energy pump photon which results in the creation of a second signal photon and an additional photon at some lower energy, referred to as the idler wave. The amplification of the signal takes place at the expense of the pump wave, and in addition, a new wave is generated. Following energy conservation principles,

$$\omega_p = \omega_s + \omega_i \tag{25}$$

where the subscripts p, s and i represent the pump, signal and idler waves.

To enhance the gain of the signal wave, the non-linear crystal used can be placed inside a cavity, forming an optical resonator. This type of resonator is known as an optical parametric oscillator (OPO) and can be used to amplify either the signal or idler waves. In some special cases it is also possible to amplify both of the output waves. The feedback created from the optical cavity means that it is not necessary to have a signal wave entering the crystal, and instead the generated wave from noise will rapidly be amplified within the OPO, providing a high intensity pump wave remains present, passing through the crystal. Generally, OPOs are operated in the scenario where only one output wave is amplified, known as a singly resonant case. This leads to a much more stable system, as only one phase matching condition needs to be maintained at one time. Such a system can be realised by coating the cavity mirrors so that the signal wavelength, for instance is highly reflected, while the idler has a high transmission. This particular case would be referred to as a singly resonant OPO. In order to produce a doubly resonant OPO, where both the signal and idler waves are reflected back into the cavity, both waves must be phase matched simultaneously. Therefore, small changes to the temperature, pump wavelength or other operating conditions can lead to instabilities. The positive aspect of a double resonant OPO is that it offers a lower threshold value, as in a singly resonant OPO, there are significant losses associated with the non-resonant wave. Within this thesis, only singly resonant OPOs will be discussed further.

In order to describe how the three amplitudes vary throughout the parametric process, a set of coupled-wave equations can be used. These are solutions of the wave equation 26, and describe the amplitude change of each wave as a function of the other two.

$$\bigtriangledown^2 \mathbf{E} = \frac{n^2}{c^2}\frac{\partial^2}{\partial t^2}\mathbf{E} + \mu_0 \frac{\partial^2}{\partial t^2}\mathbf{P}_{NL} \tag{26}$$

By describing the three waves as travelling plane waves, with signal frequency ω_s, idler frequency ω_i and pump frequency ω_p as stated in equation 25:

$$E_p(z,t) = \frac{1}{2}\left(A_p(z)\sqrt{\frac{\omega_p}{n_p}}e^{i(\omega_p t - k_p z)} + c.c \right) \tag{27}$$

$$E_s(z,t) = \frac{1}{2}\left(A_s(z)\sqrt{\frac{\omega_s}{n_s}}e^{i(\omega_s t - k_s z)} + c.c \right) \tag{28}$$

$$E_i(z,t) = \frac{1}{2}\left(A_i(z)\sqrt{\frac{\omega_i}{n_i}}e^{i(\omega_i t - k_i z)} + c.c \right) \tag{29}$$

The solutions can be found to be:

$$\frac{dA_p}{dz} = -i\kappa A_s A_i e^{i\Delta k z} \tag{30}$$

$$\frac{dA_s}{dz} = -i\kappa A_p A_i^* e^{-i\Delta k z} \tag{31}$$

$$\frac{dA_i}{dz} = -i\kappa A_p A_s^* e^{-i\Delta k z} \tag{32}$$

where κ is the coupling constant defined by equation 33, and $\Delta k = k_p - k_s - k_i$ is the phase mismatch parameter.

$$\kappa = \frac{d_{eff}}{c} \cdot \sqrt{\frac{\omega_p \omega_s \omega_i}{n_p n_s n_i}} \tag{33}$$

These coupled-wave equations, can be used to describe all three-wave mixing processes such as sum frequency generation and difference frequency generation. However, they are for the simplest case, assuming a lossless medium, collimated monochromatic plane waves, in a CW steady-state regime.

The simplest parametric scenario to describe is when there is no depletion of the pump signal, $\frac{dA_p}{dz} = 0$. By assuming no pump depletion, no initial idler signal, and some arbitrary level of signal entering the crystal, then providing the system is perfectly phase matched, such that $\Delta k = 0$, the solutions to the coupled wave equations are given by:

$$A_s(z) = A_s(0) cosh(gz) \tag{34}$$

$$A_i(z) = -iA_s^*(0) sinh(gz) \tag{35}$$

where g is the parametric gain coefficient and is defined as:

$$g = \sqrt{\left(\kappa A_p(0)\right)^2 - \left(\frac{\Delta k}{2}\right)} \tag{36}$$

Generally, when operating a CW OPO as described above, the parametric gain is very low, and thus $gz \ll 1$. In this regime the solution can be expanded up to the second order term, giving:

$$A_s(z) = As(0)\left(1 + \frac{1}{2}(gz)^2\right) \tag{37}$$

substituting in g, if $\Delta k = 0$

$$A_s(z) = A_s(0) + \frac{1}{2}(\kappa z)^2 |A_p(0)|^2 A_s(0) \tag{38}$$

$$A_i(z) = -iA_s^*(0) \cdot gz = -i\kappa z A_p(0) A_s^* \tag{39}$$

Equation 38 and 39 show the behaviour of the signal and idler wave in the case of the CW pumped OPO. It can be seen that the signal will grow quadratically, as it passes through the length of the crystal, while the idler, which was not present at the input, will grow linearly with the interaction length z.

3 Photoacoustic Tomography System

3.1 Introduction

The primary goal of this project is to develop two photoacoustic imaging systems, one for photoacoustic tomography (PAT) and another for optical resolution photoacoustic microscopy (OR-PAM). This section will focus on the creation and development of the PAT system. Section 3.2 details the construction and testing of the PAT system, specifically looking at the ASE seed source and the modulation techniques. This section continues to outline the measured output values of the system, both at the end of the fiberised section as well as after the final free space coupled amplifier. Section 3.3 discusses the development of the system into a portable device, and the changes made to achieve this.

The PAT system was focused around reaching high pulse energies, ideally in the order of tens of milli-Joules. In order to achieve this, multiple amplifier stages could be used to boost the peak power of the system. Additionally the use of large core fibres provided the benefit of high energy storage providing this could be extracted. Another design specification for this system was the requirement for tunable pulse widths, between 1-500ns. Through the use of modulators, the system could be time gated, to restrict the length of pulses to a defined duration. However, with a change of pulse width comes a change in peak power. This had to be monitored, to ensure that through changing the pulse width destructive levels of peak power were not reached. This system was targeted to run at a repetition rate of 1kHz.

3.2 MOPA1

3.2.1 Introduction

The initial system proposed and constructed, referred to as MOPA1, uses an amplified spontaneous emission (ASE) source as the seed laser and time gating via an AOM. The system is based around four power amplifiers; increasing in core diameter from 5μm to 50μm. The pulse characteristics, pulse shaping, and operational conditions are all computer controlled with the aid of an arbitrary waveform generator (AWG). The majority of the system is fibre coupled, with only the final power amplifier requiring a free space launch for both the signal and the pump. Dr Martin Berendt designed and built the MOPA1 system, and I assisted in the operation and taking measurements, upon completion of the system.

The MOPA1 system was designed to be a multi-stage amplifier system, implementing an acousto-optic modulator (AOM) as a time gating component. The system is based around three seed amplifiers, designed to produce a suitable power seed with a narrow output spectrum. This is then followed by two pre-amplifiers (pre-amps), designed to overcome losses within the system. Finally, the system uses 3 power amplifiers to reach the target pulse energy output. Throughout the MOPA1 chain, isolators are placed to protect components from back reflections that may occur. In figure 18 the system has been split into three sections, the seed, the pre-amplifiers, and the power amplifiers.

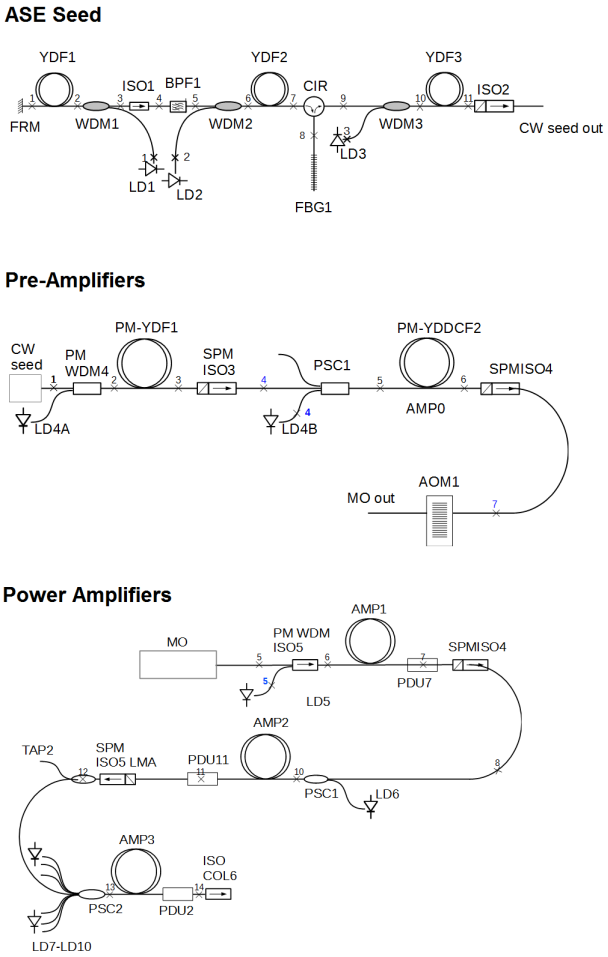

Figure 18: Schematic diagram showing the design of the MOPA1 system. PM - Polarisation maintaining, WDM - Wavelength division multiplexer, YDF - Ytterbium doped fibre, ISO - Isolator, EOM - Electro-optical modulator, PSC - Pump combiner, DCOF - Double clad optical fibre, PDU - Pump dump, AOM - Acousto-optic modulator, PBF - Band pass filter, FRM - Faraday rotating mirror, CIR - Circulator, CW - Continuous wave, FBG - Fibre Bragg grating

The seed is based around a spectrally sliced ASE source that is amplified to 20μW. Amp0 is constructed from 7m of Nufern PM-YSF-LO fibre, and can produce an output of 4mW. Thus the pre-amps are able to produce a combined gain of 23dB. After the pre-amps, the pulses pass through an AOM. This is used to carve pulses of desired pulse width and shape from the seed pulse before further amplification takes place. The pulses then pass through 4m of Nufern PM-YSF-LO, 2.1m of Nufern PLMA YDF 10/125, followed by 3.2m of Nufern PLMA YFD 25/250 fibre amplifying the signal up to 0.4mJ pulse energy.

3.2.2 ASE Seed

The MOPA1 system is seeded with pulses generated through amplified spontaneous emission (ASE) within an ytterbium doped fibre (YbDF350). ASE sources are broadband, temporally incoherent light sources that can be produced in a rare-earth doped fibre by pumping it without any signal input. The spontaneous emission produced in the fibre is then amplified due to the fibre being inverted by the pump source. The ASE propagates in both the forwards and backwards direction; however, the Faraday rotating mirror (FRM) is used to reflect the counter propagating ASE back through the fibre. Additionally, there will generally be more ASE generated in the opposite direction to the pump light, and therefore the fibre is counter pumped to encourage forward propagating ASE.

The generated ASE is then passed through a band-pass filter. This is used to allow only the wavelengths that were required to pass into the second amplifier, so that only the wavelength range that is useful for purpose is amplified, and gain is not wasted amplifying wavelengths that cannot be used. The spectral width is filtered down to 5nm using this band-pass filter. After amplifying the light through YDF2, the bandwidth of the light is drastically narrowed down to 0.4nm using a circulator and a fibre Bragg grating (FBG). This is required as, in order for the output of the MOPA system to be successfully frequency doubled, the bandwidth must be narrow. Reducing the bandwidth of the seed down to 0.4nm results in a large loss of power, and therefore a second seed amplifier is used to regain the output power from YDF2 at the end of YDF3 but with a significantly smaller bandwidth. The final output of the CW seed has an average output power of 20μW.

3.2.3 AOM Modulation

The MOPA1 system relies on an acousto-optic modulator (AOM) to specify both the repetition rate and pulse duration within the system. The principle of AOM operation is based on the generation of acoustic waves within a crystal from an applied RF signal. The generated acoustic waves propagating through the crystal modulate the refractive index, forming a sinusoidal grating inside the crystal. Light passing through the crystal will be scattered from the acoustic wavefronts. In order to retain as much of the signal as possible, scattering from successive acoustic wavefronts needs to interfere constructively. This relies on the Bragg condition being met, such that:

$$n\lambda = 2\Lambda sin\theta_d \tag{40}$$

where n is an integer representing the order of diffraction, λ is the wavelength of the incident light, Λ is the wavelength of the sound waves, and θ_d is the angle the scattered light makes with the acoustic wavefronts.

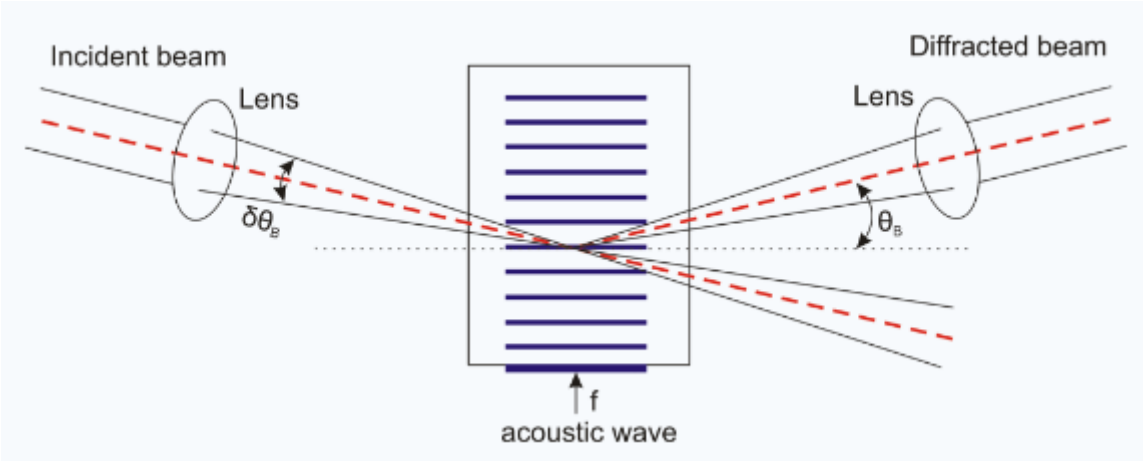

Figure 19: Schematic diagram showing the incident light being diffracted from the refractive index grating generated by the acoustic wave propagating through the crystal. Image from Elent A[39]

In a fibre coupled AOM, the device is set up such that when no RF signal is applied, the light will be terminated inside the component. When a signal is applied, the output fibre is positioned so that it picks up the first order diffraction, and thus the signal is transmitted through the device and onto the rest of the system. Using a pulsed RF signal, it is possible to produce a pulsed output at a chosen repetition rate, as well as pulse duration by adjusting the pulse width. The AOM can also be used to shape the pulse. This is done by applying a shaped RF pulse to the AOM, which causes a more gradual transition between the two AOM states resulting in a varied amplitude along the pulse width. By shaping the pulse we can account for pulse distortion that will arise later in the system.

3.2.4 System Operations

Unlike typical fibre laser systems, the high energy PAT system was required to operate at a frequency around 100Hz. To successfully develop the MOPA system to operate at a low frequency, several amplifier stages made use of pulse pumping. In a pulse pumping set-up, the amplifier pump is only switched on for a short duration before the signal pulse. The pump pulse needs to be sufficient to fully invert the fibre before the pulse passes through. The benefit to pulse pumping at low frequencies is the removal of long periods of time where the fibre is pumped with no signal passing through. This can reduce the energy loss throughout the system due to a reduction in spontaneous emission and ASE.

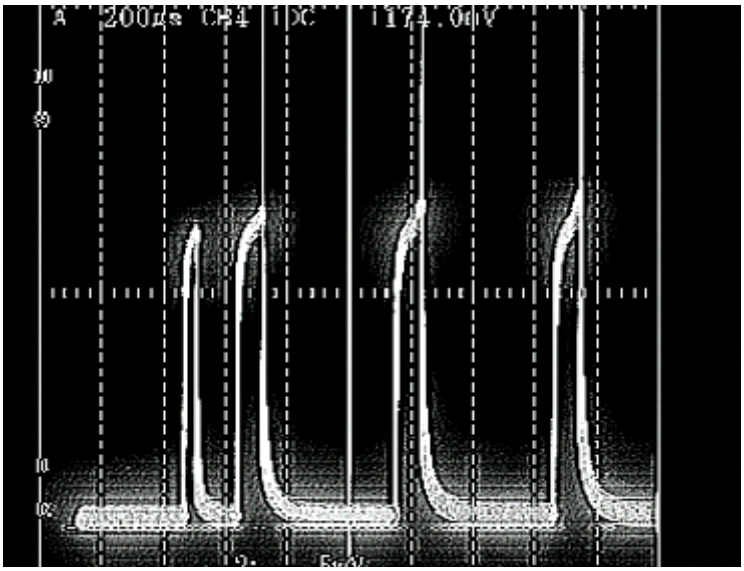

Figure 20: trace showing the pulse pumping scheme for the MOPA1 amplifiers

To provide the most flexibility possible for experimentations with photoacoustic imaging, UCL requested that the PAT system be able to generate short bursts of pulses, known as codes. These codes needed to be generated to user requirements, in terms of number of pulses as well as the spacing between them. To incorporate this within the MOPA1 system, Dr Martin Berendt designed a LabView application which allowed the user to manually enter the number of pulses required as well as the pulse length they should be contained within.

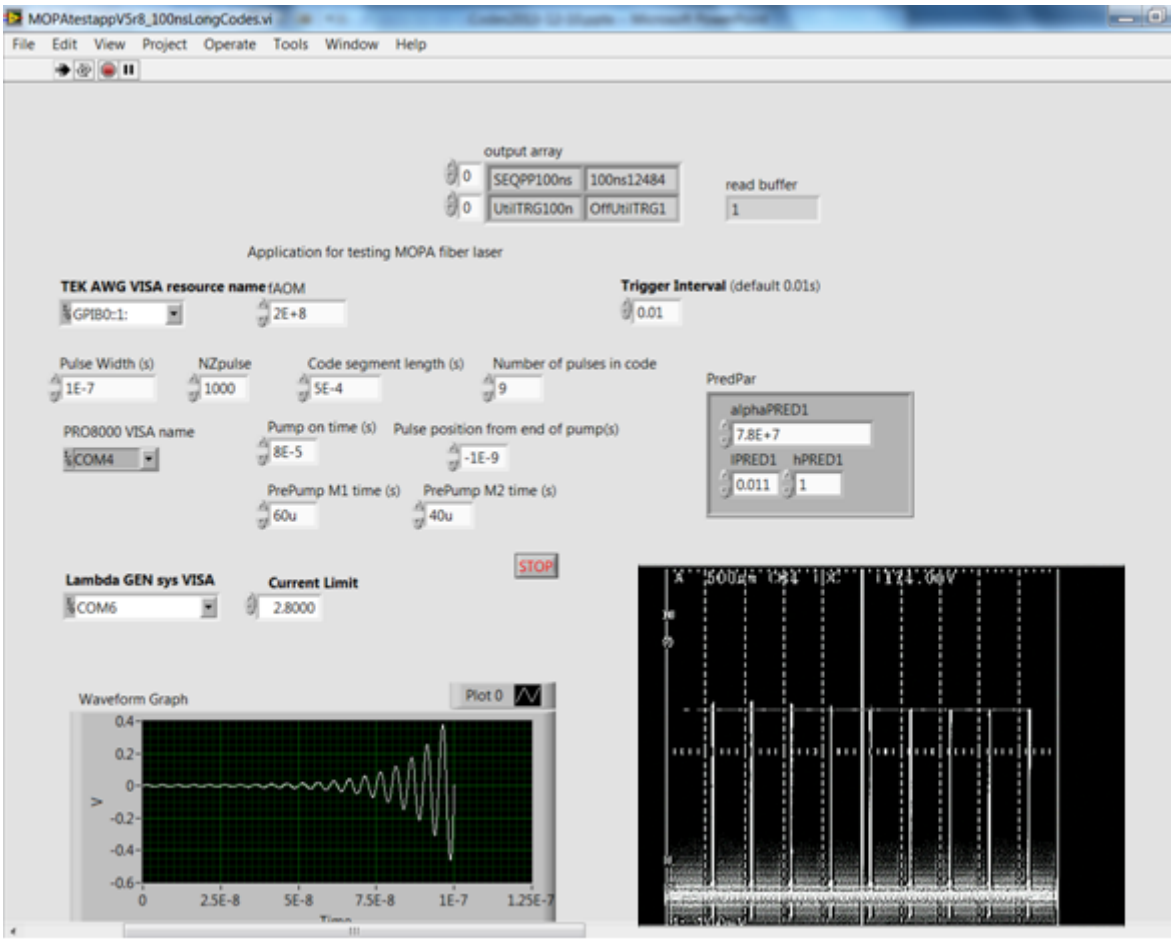

Figure 21: LabView program used to generated codes of specified number of pulses. Bottom right shows the 9 pulses contained within the code all reaching similar amplitudes after amplification

3.2.5 Free Space Coupled Final Amplifier Stage

To be able to reach high pulse energies, a final amplifier stage was added to the system shown in figure 18. In an attempt to reach as high an output as possible, the final amplifier stage, AMP4, relied on a LMA $50\mu m$ core fibre. Due to the size of the fibre, it was difficult to splice to the rest of the system. The amplifier was constructed from 1m of multi-mode CorActive DCF-YB-50/400um fibre. Therefore the final amplifier stage was set up to be coupled via free space optics, as shown in figure 22. Due to the large core size of this fibre, it was coiled tightly in an attempt to operate the fibre in a single mode.

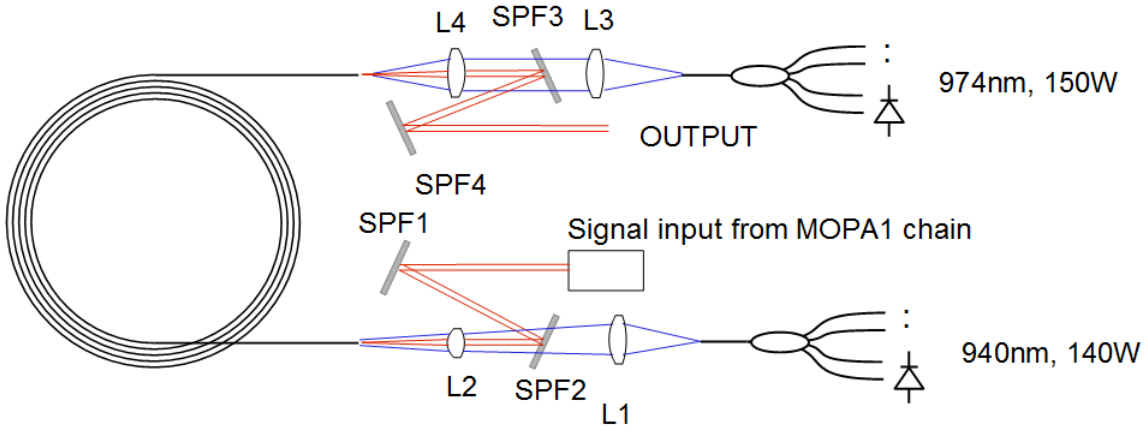

Figure 22: Schematic showing the free space coupled, bidirectional pump set-up for the CorActive 50μm core fibre. Schematic drawn by Dr Martin Berendt

The signal is coupled into the amplifier via the reflection from two dichroic mirrors SPF1 and SPF2 and then focused through lens L2, with a focal length of 8mm. The system is set up with the option of both co and counter pumps, which can be run individually or simultaneously. The pump light is generated from multiple diodes connected to a combiner to provide around 150W of available power in either direction. The pump light is coupled through an additional lens, L1 for the co-pump and L3 for the counter pump. The wavelengths of the pump sources were chosen to be different to prevent the non-absorbed pump light from being coupled into the pump diodes operating in the opposite direction.

For the PAT system to be sufficient for initial testing stages, it needed to reach a pulse energy output of greater than 10mJ. With the addition of the free space pumped final amplifier stage, the system was only able to produce around 2.5mJ. The main limiting factor was the energy storage capability of the final amplifier. Therefore, in order to reach significantly higher output energies, the size of the fibre needed to be increased. However, the $50\mu m$ core fibre being used is one of the largest commercially available ytterbium doped fibres, and thus, finding a suitable substitution with a larger core size proved challenging. This is due to the fact that as the core diameter, and in turn the cladding diameter, of the fibre increase, the fibre begins to lose its flexible property and more resembles a glass rod. This limits the practical application as well as significantly increasing the space required to incorporate the large fibre into a portable fibre system.

The only commercially available ytterbium doped fibre that had a core size that exceeded $50\mu m$ at the time of testing was CorActive HPA-YB-140-02. This is a double clad fibre, with a core size of $140\mu m$ However, the ytterbium doping is confined to a central region of diameter $85\mu m$ within the core. With a confined doping region, there may be modes that propagate outside of the doped region which will not produce any gain. Despite this, the doped region still exceeded the $50\mu m$ core of the fibre being used. Consequently, the final amplifier stage was replaced with a 2.5m length of the CorActive HPA-YB-140-02 fibre. The final stage was replaced, rather than adding a new stag,e for ease of measurement. With the final stage being free space coupled, it required comparatively little work to swap the fibres and re-align, rather than to add a completely new stage to the MOPA system.

After the fibre had been prepared, it was placed into the system for initial tests. The results of these showed no improvement over the previous fibre. An initial assumption was that the free space launch of the pump, or the signal, was not well aligned. To improve the alignment, a camera was set up to image the output facet of the fibre. Figure 23 shows the image that was taken while the system was running. The larger illuminated area represents the entire 140μm core. However, while the system was running, the signal was found to be confined to a much smaller region than expected. The signal light, represented by the bright central spot, was confined to a region of less than 25μm. The position of the launched signal was adjusted slightly, but the same result were achieved, whenever the signal was coupled into the core of the fibre.

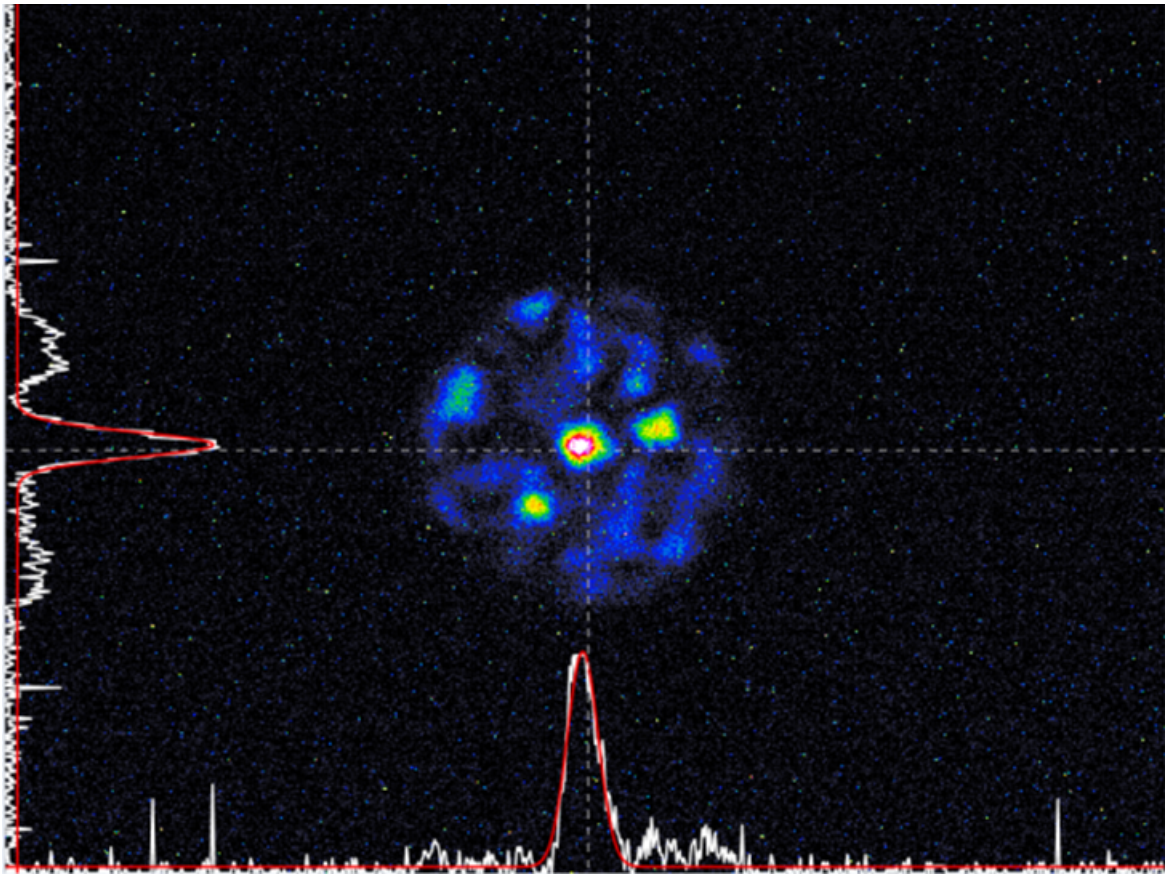

Figure 23: Image of the end facet of CorActive HPA -YB-140-02 fibre, being pumped with signal passing through.

With no other larger core fibres commercially available, a large core fibre had to be developed in-house. The in house fibre had a core diameter of 96μm with uniform ytterbium doping, providing us with the largest core active fibre available. The CorActive HPA-YB-140-02 fibre was swapped with 3.7m of the in-house fibre. After re-alignment of the pumps and signal beams entering the fibre, the output pulse energy reached almost 6mJ before plateauing. This was more than double the output pulse energy when the 50μm core fibre was used as the final amplifier. However, the energy storage would be expected to scale with the area, and therefore with no other limiting factors, the anticipated output would be increased by a factor of four, compared with the output of the 50μm core. To improve the output of the system, a narrow band filter was added to the input of the final amplifier stage, removing any ASE build up from previous amplifier stages. With the addition of the filter, the system was now capable of reaching a pulse energy of up to 9.7mJ.

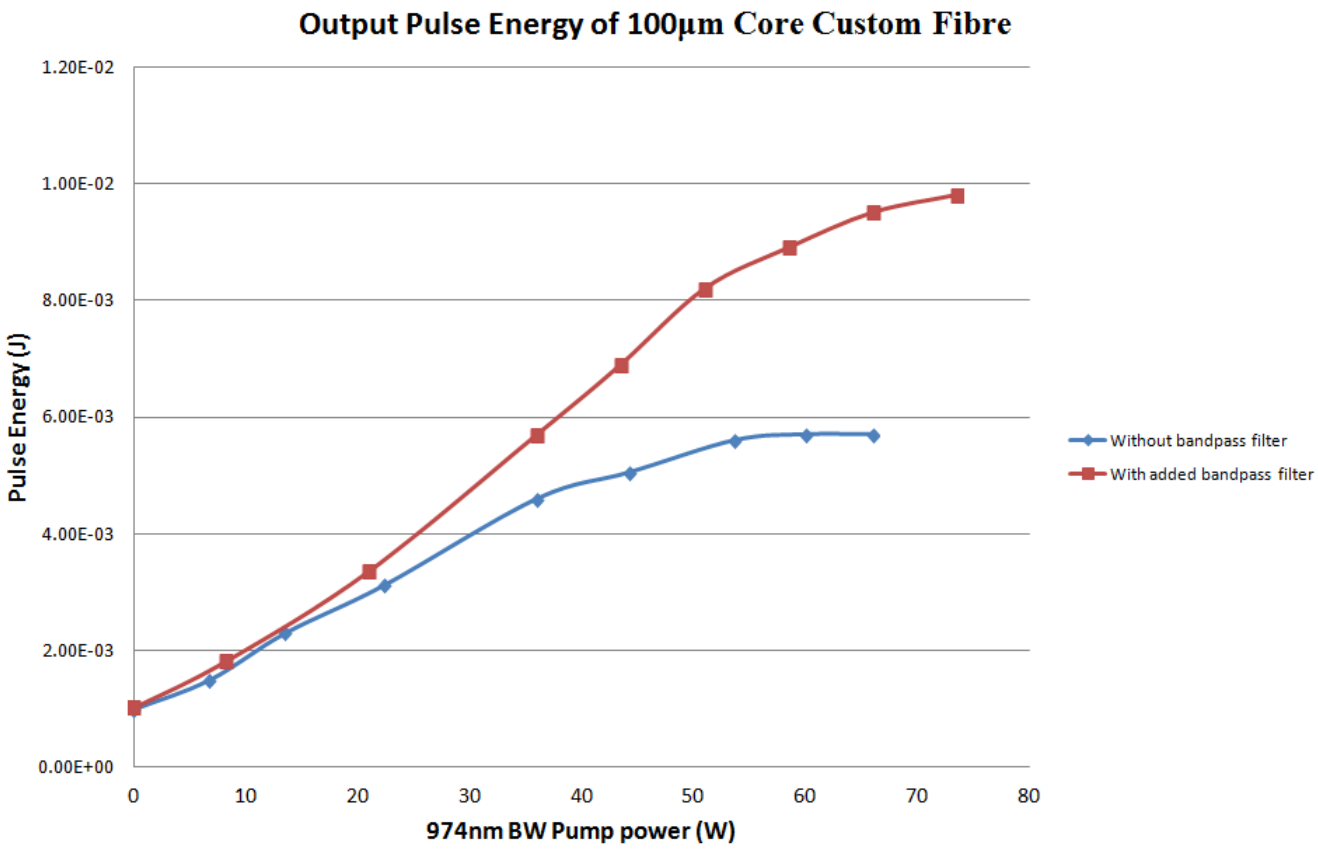

Figure 24: Output Pulse energy of the MOPA1 system, using a custom in-house made 100μm core fibre as the final amplifier stage. Red curve represents data taken with the addition of a band-pass filter before the final amplifier. Blue curve represents the data taken without the filter.

3.2.6 Conclusions

The MOPA 1 system was an initial system design that was targeted to be able to operate at the specified operating conditions proposed in the project brief, described in section 1.5. With the pulse widths and repetition rates being the main focus, our experiments were based around exploring the maximum potential pulse energies that could be produced by the system. The system was based around an ASE seed, as this gave us flexibility in terms of the seed power, as we could increase the gain in the seed amplifiers, or swap the band pass filter to create a narrower spectrum if required. The main modulation of the system was controlled via an AOM. By adjusting the opening times of the modulator we could cut pulses to required length as well shape them to account for pulse distortion in later amplifiers. The AOM was digitally controlled via a LabView program to provide an easy method to tune the opening conditions to generate the desired pulse. This program was also used to control the amplifiers of the system, and operate them in a pulsed scheme. Pulse pumping was chosen to help reduce long periods of time where the amplifier was inverted but no pulse was present due to the low operating frequency of the system. The final improvements made to the system was focused on the final amplifier stage. By trying a variety of commercial fibres we concluded that with the system we had it would be difficult to reach a pulse energy over 5mJ. Therefore we opted to develop a custom large mode area in-house fibre, with a core diameter of 96μm. This fibre successfully pushed our maximum pulse energy obtained to 9.7mJ

3.3 Portable System

3.3.1 Introduction

With the MOPA1 system now achieving a usable pulse energy, we needed to look into being able to make the system more portable, so that the system could be taken to UCL to undergo extensive photoacoustic tests. Although MOPA1 was built on a breadboard, the addition of the free space optics made it less suitable for transportation. With the development and learning from the MOPA1 system, a new system was designed that would be able to reach pulse energies of around 5mJ, whilst remaining fully fiberised to preserve the portability aspect of the system. This system will be referred to as MOPA3 throughout the rest of this thesis. The MOPA3 system was designed by Dr Martin Berendt, and I assisted in the building and operation of the system

In order to make the system more compact and simple, we opted to remove the AOM time gating from the system. Although this helped to simplify the system, the lack of a modulator added the additional constraint that the correct pulse width and repetition rate were achieved from the seed. Due to this fact, the decision was made to build the system with a Fabry-Perot (FP) laser diode as the seed. With this seed, we could produce pulses between tens and hundreds of nanoseconds long, matching the requirements of the targeted system. The design for the system, as shown in figure 25 is based around 3 amplifier stages, 5m of Nufern PLMA YDF 10/125, 4.2m of Nufern PLMA YDF 25/250 and 0.85m of CorActive DCF-YB-50/400-FA. An isolator-band-pass filter hybrid component is used before the final amplifier, to cut out any ASE build-up in Amp1 and Amp2 from entering it.

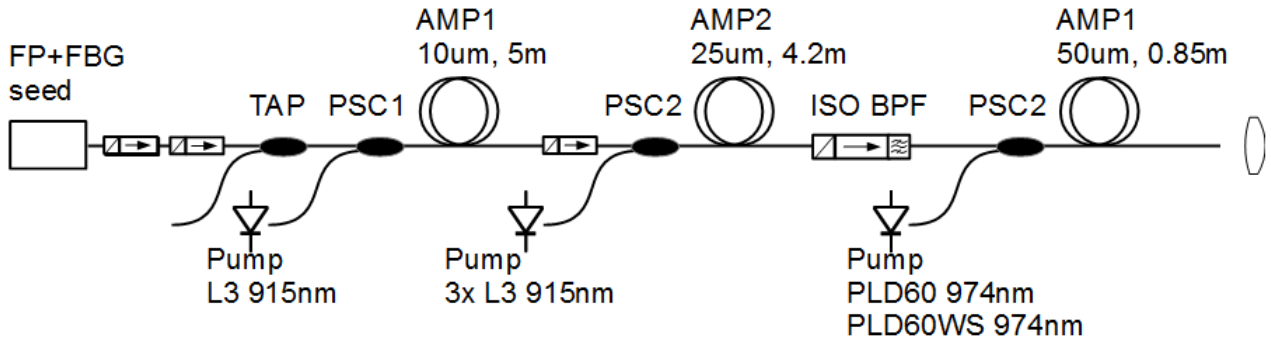

Figure 25: Schematic diagram showing the design of the MOPA3 system. FP - Fabry-Perot, FBG - Fibre Bragg grating, ISOBPF - Isolator-band-pass filter hybrid, PSC - Pump combiner.

When the system was built, there was an immediate problem of SBS present. Due to the requirement of long pulses, an attempt was made to reduce the SBS by dithering the pulse. Figure 26 shows various pulse shapes that were tried in order to reduce the SBS, however, it was only the final pulse shape that succeeded. Therefore, in order to make pulses of the correct length - tens of nanoseconds, the pulse had to be made up with several shorter pulses close together.

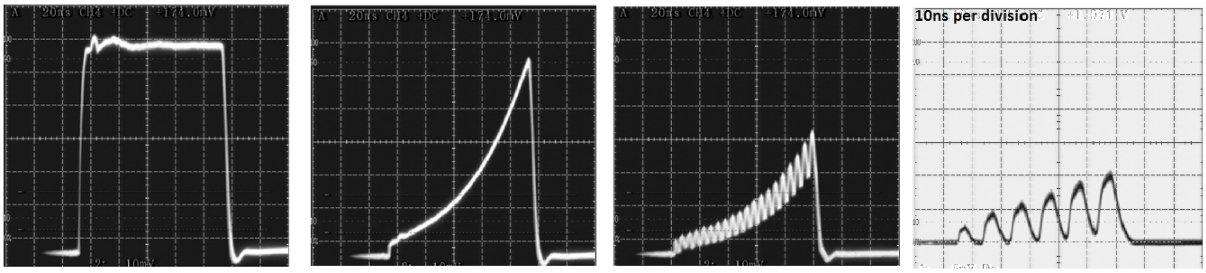

Figure 26: Pulse shape required to create long (greater than 20ns) pulses without producing SBS.

With the burst of pulses, the SBS was successfully suppressed, allowing initial tests to be carried out to determine the output of the system. Primary tests were performed at various pulse widths and repetition rates in order to optimise the output power, optical spectrum, and manage any ASE or non-linear effects. Figure 27 shows a set of data taken at 40kHz, where we obtained an average output power of almost 4W, with Amp2 producing more than 16dB of gain. The spectrum, shown in figure 28 was taken at the maximum pump power measured, displaying a 3dB spectral bandwidth of 0.49nm. This was slightly broadened from the seed pulse, which measured 0.2nm after the FBG. This broadening is due to SPM through the fibre system, and currently is not an issue.

Figure 27: Output power and gain from Amp2 as a function of the applied pump power. Data taken with the system running at 40kHz and a pulse burst of 6 pulses within a 55ns window

The results from the MOPA3 system indicated that, with the addition of another amplifier, we could potentially achieve a useful output pulse energy. However, our partners at UCL deemed the pulse burst set-up unsuitable for their measurements, and would prefer to have a single pulse. Therefore before further investigating the amplifier chain, a different solution to the SBS issue had to be implemented.

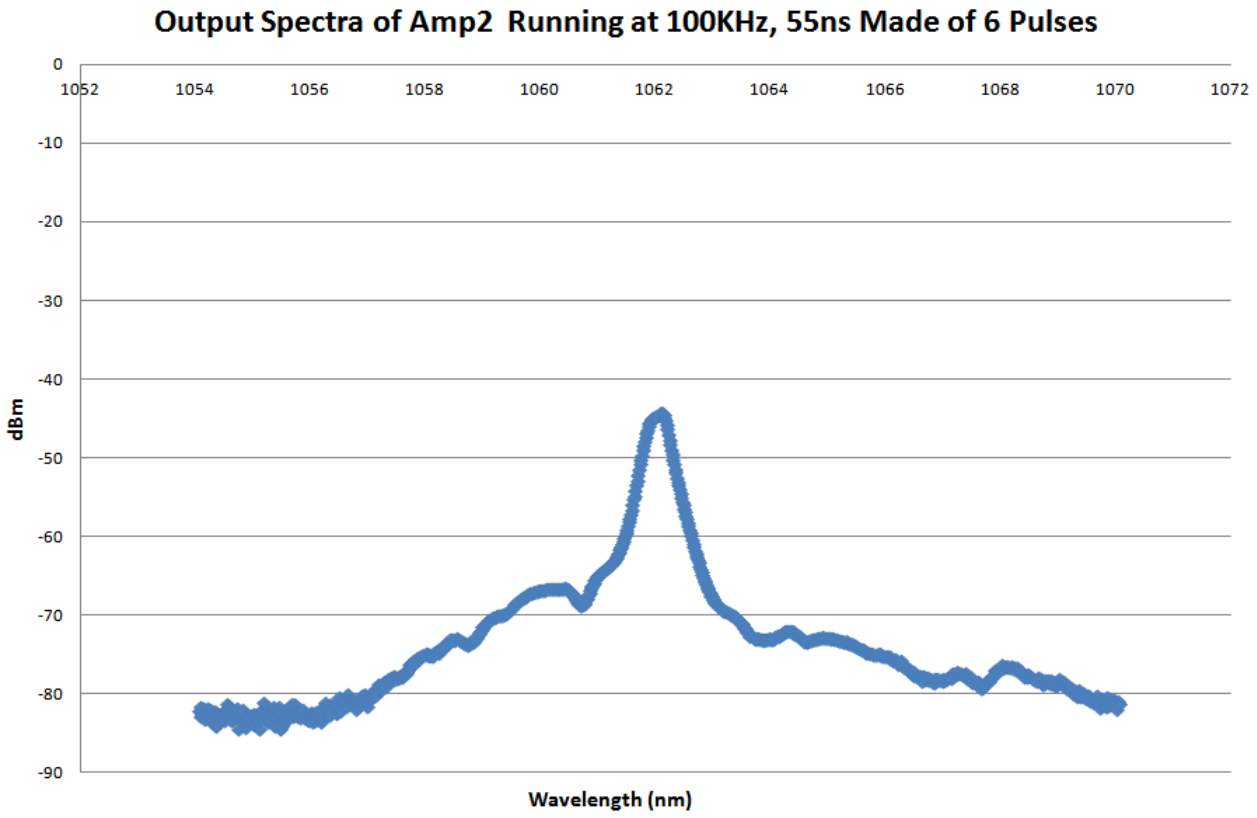

Figure 28: Output spectrum from Amp2. Data taken with the system running at 40kHz and a pulse burst of 6 pulses within a 55ns window

3.3.2 SLED Seed

As the FP diode had to be modulated to produce longer pulses without the generation of SBS, a decision was made to swap the seed to a Superluminescent diode (SLED). An SLED comes packaged much like a FP diode, however produces an output more similar to an ASE source. Therefore, using an SLED provides the space benefit of a diode but will prevent the SBS issue arising with the FP diode due to the significantly wider spectral width. The output of the SLED has a relatively broad spectrum, typically around 70nm. In order to generate a narrow bandwidth signal for amplification the signal from the SLED was filtered using a 5nm band-pass filter followed by a circulator-FBG grating, as shown in figure 29. The spectrum shown is measured through the FBG and thus the dip in the spectrum represents the 0.2nm bandwidth that is reflected from the FBG back to the circulator and through the system. The SLED behaves in a very similar way to the ASE source used in MOPA1. Due to the average power output of the SLED being over such a broad spectrum, after filtering, the power was significantly lower than that of the FP seed.

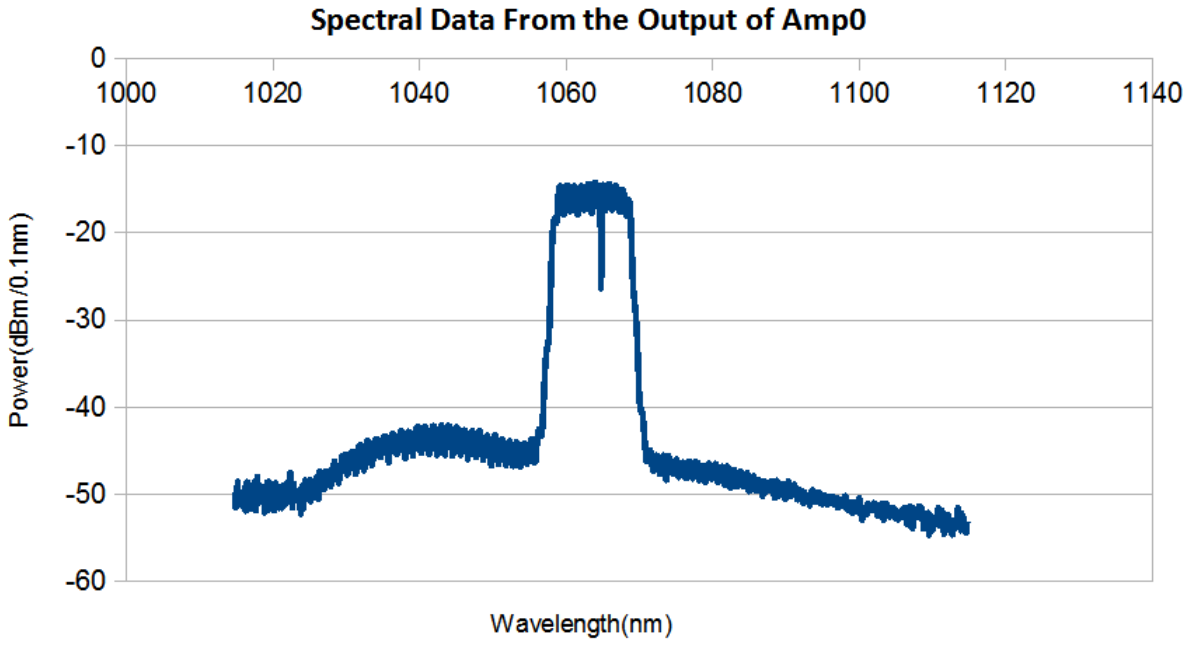

Figure 29: Spectral data taken at the output of AMP0, showing the broad spectral output from the SLED seed diode

To overcome this, an additional amplifier was added to the system after the seed diode. This amplifier increased the power of the seed diode output before the FBG, aiming to produce a similar seed power, after the FBG, as the FP could achieve. The additional amplifier was constructed from 6.5m of Nufern PM-YSF-HI fibre, and was bi-directionally pumped in order to achieve enough gain to overcome the losses produced from reducing the bandwidth down to 0.2nm with the FBG. The complete set-up for the SLED MOPA system is shown in figure 30. Furthermore, we also swapped the final amplifier stage to use the in-house 100μm fibre, as this was expected to increase the output pulse energy to 5mJ.

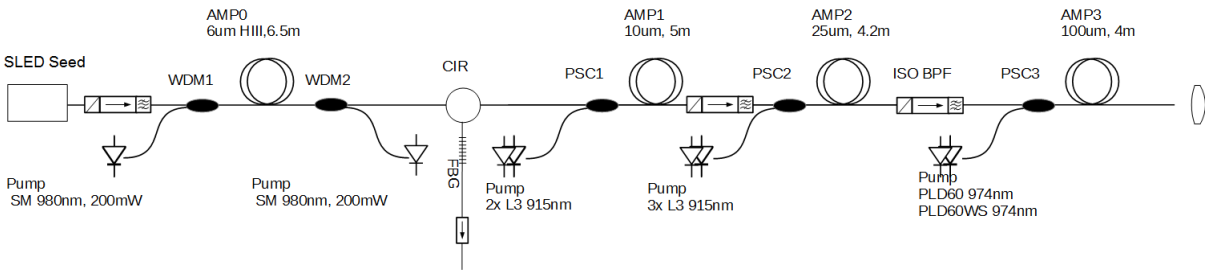

Figure 30: Schematic diagram of the revised MOPA3 design using an SLED seed diode. SLED - Superluminescent diode, ISOBPF - Isolator-band-pass filter hybrid, WDM - Wavelength division multiplexer, CIR - Circulator, PSC - Pump combiner.

3.3.3 System Details

Further measurements were taken at the output of AMP3, to investigate the spectral properties and temporal profile of the pulse, as well as looking into how the pulse energy evolved as the pump power was increased. With the diagnostic set-up used, there was very little power available to measure a clear spectrum, as only the signal power was high enough. However, this did provide enough power to be able to measure the 3dB spectral bandwidth as 0.2nm, indicating that there had been little to no broadening throughout the entire amplifier chain. As there were no modulators within the system, it was crucial that the seed pulse shape was correct, to ensure that a square pulse was obtained at the end of the MOPA chain. Figure 31 shows both the input and output pulses of the MOPA system, and it is clear that the input pulse is a suitable shape, such that the distortion arising from the amplifiers, due to gain saturation effect, produce a relatively square output pulse.

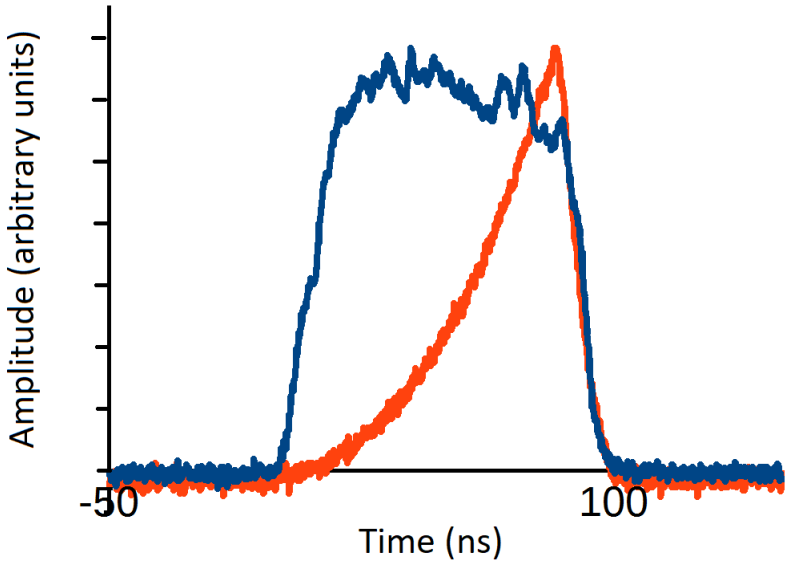

Figure 31: Input pulse shape to the MOPA system, shown in red, and the output pulse shape, shown in blue.

The MOPA3 system used a pulse pumping scheme for the pump diodes, and therefore when increasing the pump to the final amplifier, it is more meaningful to look at the pump energy used. Figure 32 shows how the output pulse energy of signal increased with applied pump energy, up to a final signal pulse energy of over 5mJ.

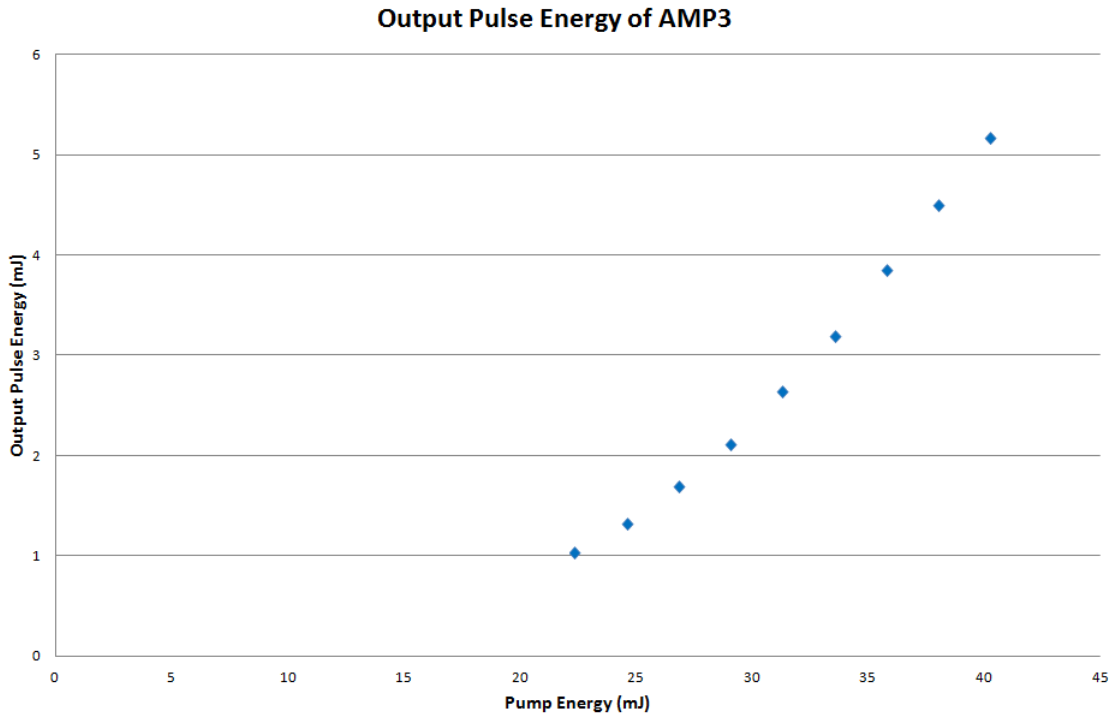

Figure 32: Output pulse energy of the MOPA3 system, shown as a function of applied pump energy to AMP3.

With the MOPA3 system able to reach an output pulse energy of over 5mJ running at a repetition rate of 100Hz, with a narrow 0.2nm spectral bandwidth, the system was highly attractive to UCL as an initial source to begin running high energy photoacoustic measurements using the fundamental (1060nm) beam. The system was suitably successful that the findings were published at CLEO 2015, highlighting both the energy potential and shaping capabilities[40].

3.3.4 Conclusions

This system relied on a SLED as the seed source as opposed to either an ASE source or FP-diode. This allowed us to develop a system that was both portable and capable of producing 5mJ output pulse energy. In order to achieve this the system was operated at 100Hz with a pulse duration of 100ns. Due to the lack of AOM, the ASE was controlled with the incorporation of isolator-band-pass filter hybrid components between amplifier stages as well as the use of pulse pumping to minimise the build up of ASE within the amplifiers. Successfully reaching an output energy of 5mJ allowed the system to be used for initial photoacoustic testing at UCL, progressing towards the goal of a portable PAT system.

4 Optical Resolution Photoacoustic Microscopy

The OR-PAM system follows similar design elements to that of the PAT system, however due to the differences in the targets various components could be removed or changed, resulting in a more compact and simple system. This section of the thesis will focus on the design and development of the OR-PAM system. Section 4.1 discusses the first design of the system following on directly from the MOPA1 PAT system. Measurements were taken to investigate the impact of a different pulse width and repetition rate to the system. Section 4.2 discusses initial modifications to the systems seed source, and how using an ASE seed source affected the system results. Finally section 4.3 investigates further how different seeds can impact the system by swapping to a DFB seed from the ASE source.

The OR-PAM system had slightly different targets to that of the PAT system. Most notably the OR-PAM system was required to be polarisation maintaining throughout. This further limited the availability of fibres that could be used within the system. Due to this requirement the target pulse energy was reduced to 1 micro-Joule. This system was also aiming to operate at higher repetition rates than that of the PAT system, with an initial target of 500kHz. Furthermore the specified pulse width was much narrower with a duration in the range of 0.5-50ns. This reduced pulse width will also lead to higher peak powers and therefore non-linear effects were expected to be more present.

4.1 Initial Three Stage FBG System

4.1.1 Introduction

The development of the PAT system, provided insight into initial expectations for the output of an OR-PAM system. Moreover, certain design considerations were highlighted, for instance, the use of an ASE seed led to the requirement of multiple pre-amplifier stages, which add complexity and increase the physical size of the system. A lot of the learning from the PAT system can be transferred, as the basic design for the OR-PAM system is very similar, incorporating a seed source, followed by pre-amplifier stages and final power amplifiers. The main restriction with the OR-PAM system, compared with PAT, is the requirement to maintain a good beam quality, $M^2 \sim 1$, and thus a single mode output must be produced. This limits the maximum core size that can be used for the amplifier fibres, and in turn, the available output pulse energy that can be reached. Although the system has a lower targeted output energy, due to expected efficiencies in the frequency conversion process, which largely depends on the input pulse peak power and hence the pulse energy. A large portion of the energy may not be converted, and thus as high an energy as possible generated at the fundamental wavelength is desirable.

MOPA2 was designed to run with a single pre-amplifier stage followed by two power amplifiers. The pre-amplifier consists of 5.5m of 5μm diameter, core pumped fibre, while the two power amplifiers are cladding pumped with increasing core diameters from 10μm to 25μm of lengths 6m and 2.5m respectively. Unlike the PAT system, this system uses both an electro-optic modulator (EOM) and an acousto-optic modulator (AOM). This is so that the pulse shape and duration can be set using the EOM, while the AOM can be used later in the amplifier chain to reduce the repetition rate as well as to remove excess ASE in between the pulses. This allows for the system to be operated at a comparable repetition rate to the PAT system for comparison and low energy tests, as well as at higher rates for optical resolution imaging. The initial design of the system can be seen in figure 33.

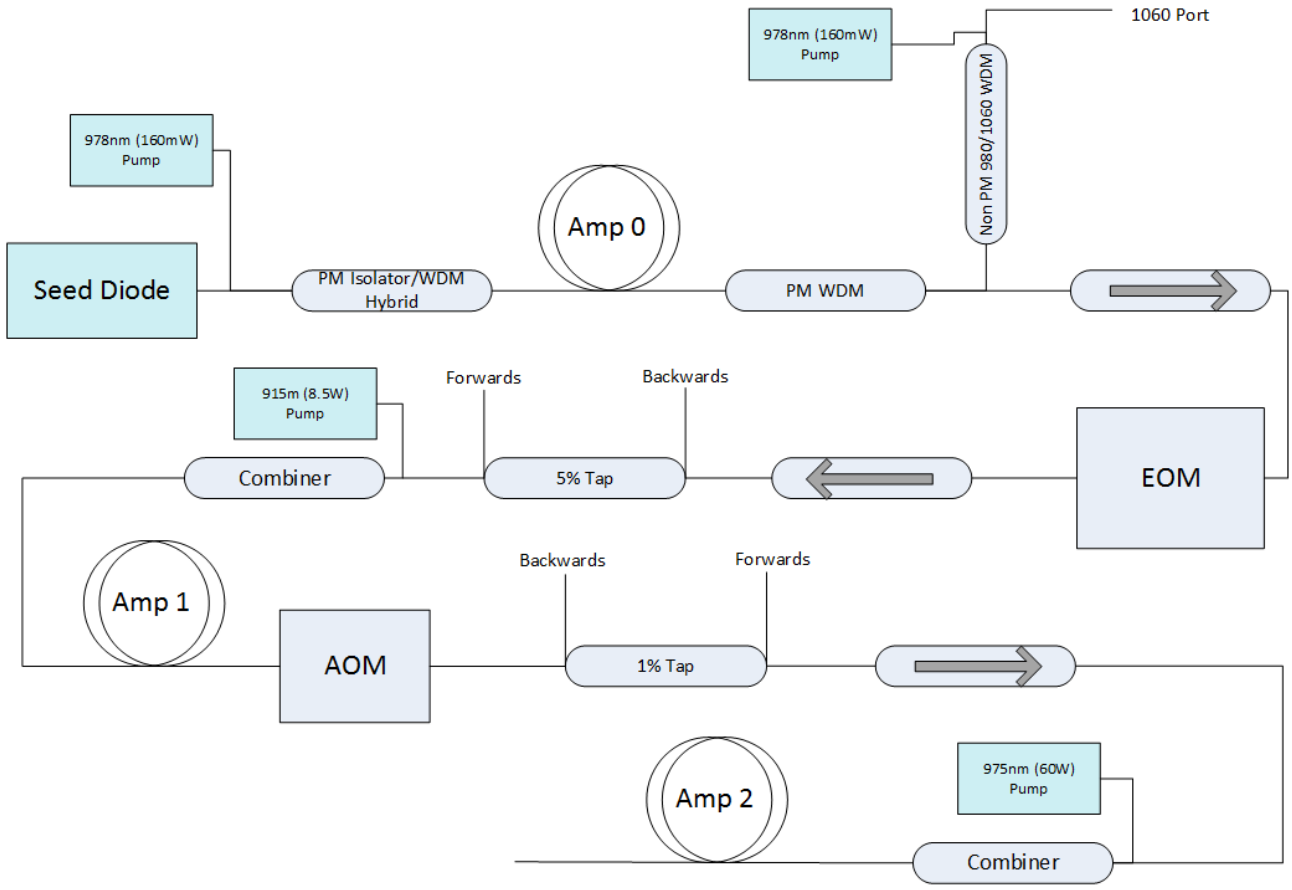

Figure 33: Schematic diagram showing the design of the MOPA 2 system. Light blue boxes represent laser diodes, arrows represent isolators and double circles represent ytterbium doped fibre amplifiers. PM - Polarisation maintaining, WDM - Wavelength division multiplexer, EOM - Electro-optic modulator, AOM - Acousto-optic modulator

4.1.2 Fabry-Perot Seed with Fibre Bragg Grating Locking

The seed diode used in the OR-PAM set-up, figure 33, is a 1064CHP, 3S photonics diode mounted on a PicoLAS BFS-VRM 03 high speed seed driver. With the addition of a narrow 0.2nm bandwidth fibre Bragg grating (FBG) spliced to the seed diode, narrow bandwidth (0.23nm) nanosecond pulses, centred around 1061.2nm can be produced. Although the use of an FP seed resulted in SBS in the PAT portable system, this can be overcome in this case, by generating longer square shaped pulses from the FP diode, where SBS was not measured, and then carving the pulse width down to the required duration using the EOM. The benefit of using an FP diode over the SLED or ASE source is that due to the higher peak powers within a narrower bandwidth, the need for seed amplifiers is reduced. Using only one seed amplifier, or even none at all, simplifies the system and helps to condense the system whilst minimising component failure and amplifier configuration. Figure 34 shows the spectral data taken while operating the seed at three different repetition rates (5, 10 and 25kHz) as well as two different pulse widths (25 and 50ns).

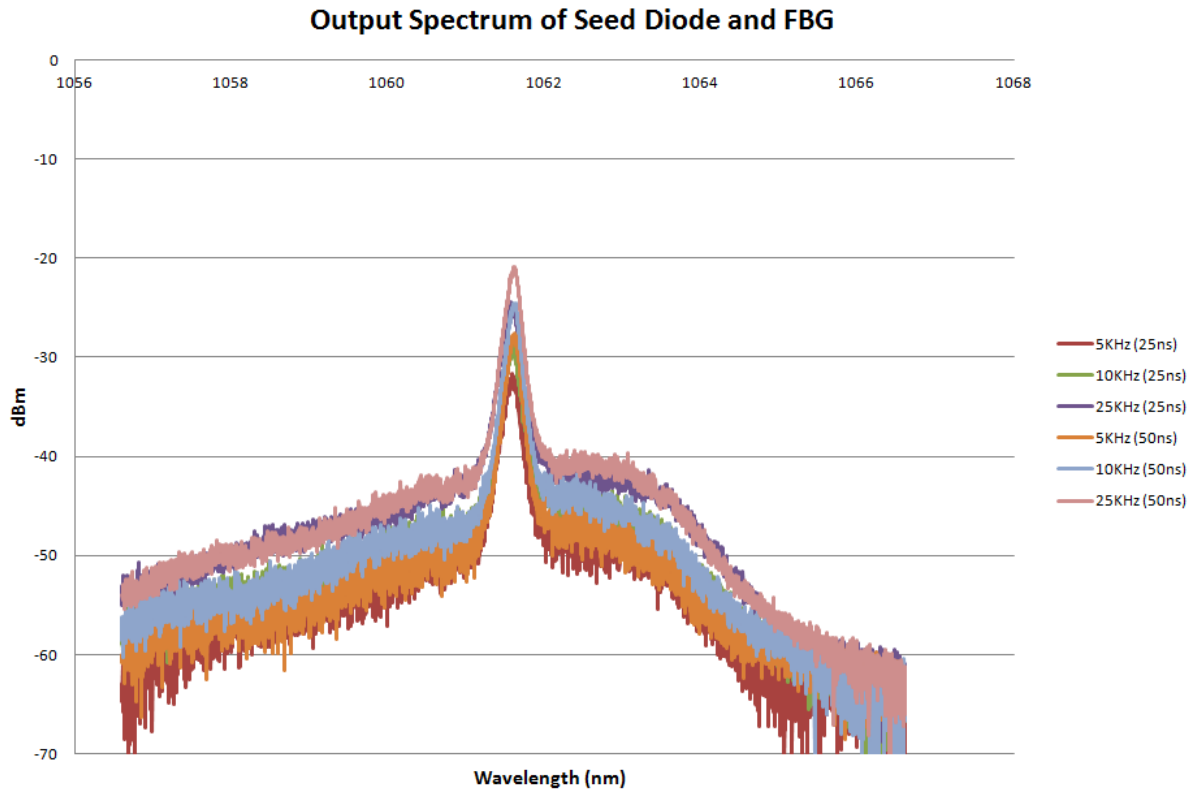

Figure 34: Output spectrum from FBG stabilised seed diode. Signal is centred around 1061.2nm and has a spectral width of 0.23nm

The Seed pulses are created using an arbitrary waveform generator (AWG) and can be produced at any length from 15ns (limited by the diode driver) to continuous operation. One issue with this set-up was the operating drive voltage for the PicoLAS board was 1V, while the AWG was only able to produce 0.5V. Thus, in order to effectively drive the seed diode, a radio frequency (RF) amplifier was attached to the output of the AWG alongside two attenuators, to produce an output signal of 1V. With the increased drive voltage, the seed diode is able to output 4.9mW average power for 50ns, and over 16mW for a pulse width of 200ns at a repetition rate of 25kHz.

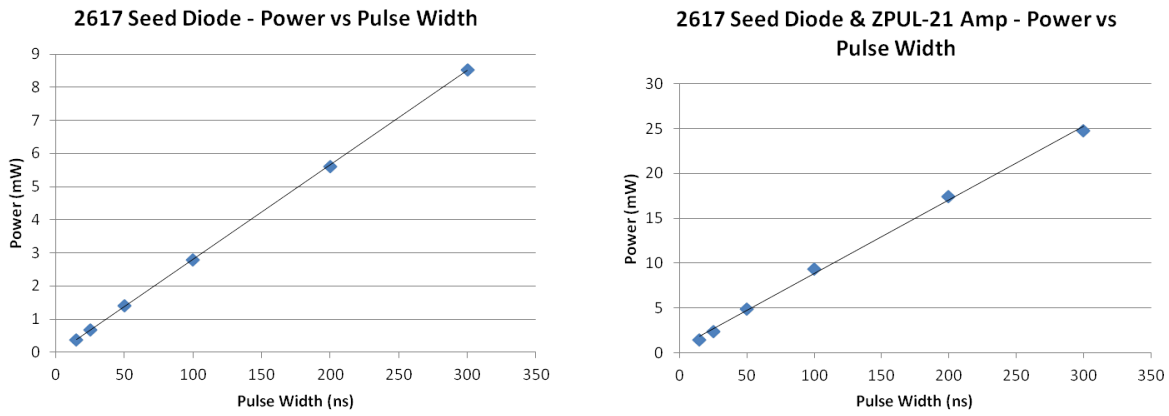

Figure 35: Output power from seed diode measured at varying pulse widths between 15ns and 300ns. Left: Seed driven straight from AWG. Right: Seed driven by an amplified AWG output. All data taken at a constant repetition rate of 25kHz, with a bias voltage of 20mA

4.1.3 Modulation Techniques

The OR-PAM system was designed with two modulators; an electro-optic modulator (EOM) and an acousto-optic modulator (AOM). The EOM is used to shape the pulse to compensate for distortions that will occur in later amplifier stages. This is achieved by applying different pulse shapes to the EOM driver via the AWG. The EOM relies on the electro-optic effect, which causes a change to the refractive index of an optical medium when an electric field is applied to it. The crystals used in EOMs are birefringent and the refractive index can be manipulated when an external voltage is applied. By applying different voltages to the EOM, it can effectively 'open' and 'close', either allowing or rejecting the linearly polarised pulse to pass through the device. Generally, the switching speeds of the modulators are limited by the drivers, but typically are within a few nanoseconds.

The difference between the output power of the EOM when it is opened and closed is referred to as the extinction ratio. The extinction ratio can be referred to in one of two ways: the direct current (DC) extinction ratio (ER_{dc}) and the dynamic extinction ratio (DER). There is no difference between the physical quantities; they are just two different processes by which the extinction ratio can be measured. In order to acquire a clear and definitive value for the extinction ratio, we decided to measure both the ER_{dc} and the DER.

To measure the ER_{dc} the bias voltage is adjusted and the power through the EOM is measured; the ER_{dc} is the difference between the maximum and minimum powers. When measuring the ER_{dc} there is no RF signal applied to the EOM. The system was operated in three different configurations when measuring the ER_{dc} to ascertain if there was any significant difference to the measurement. The seed was run in a CW mode and a 100ns, 100kHz pulse mode, both with the amplifier pumped and not pumped. At the same time as measuring the ER_{dc} it was also possible to compare the maximum power output to the input power, in order to measure the insertion loss. From the data, both the insertion loss and ER_{dc} were calculated. The values are shown in table 1.

Table 1: ER_{dc} Measurements

Seed Operation Mode	Insertion Loss (dB)	DC Extinction Ratio (dB)
CW	3.98	39.35
100ns-100kHz	4.19	35.08
100ns-100kHz - 103mW pump power	4	36.96

The DER is another approach to measuring the extinction ratio. Unlike the ER_{dc} measurement, to calculate the DER, an RF signal is applied to the EOM to control the opening and closing. The bias is set to the operating voltage; in this case, maximum transmission and thus the voltage was set to 4.5V at which previously a maximum power had been measured. The RF signal applied to the EOM was such that only half of the pulse was passed through the EOM. This made it possible to see the maximum and minimum values of the transmitted power simultaneously. Figure 36 shows the maximum and minimum values taken from the oscilloscope whilst following the regime explained. From these values, the DER was calculated to be 27.96dB. Although this value is significantly lower than the ER_{dc} measured, this is not unexpected [37], and both the values were within measurement error of the test data, stating an extinction ratio of greater than 30dB.

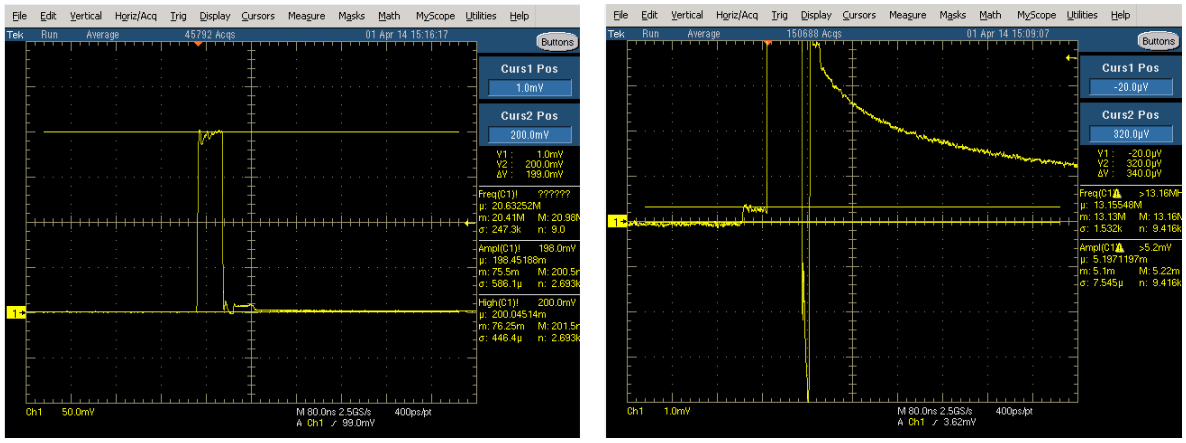

Figure 36: Left: Oscilloscope trace of EOM bias set to allow the maximum power through the EOM. Right: Oscilloscope trace of EOM bias set to block the maximum power through the EOM

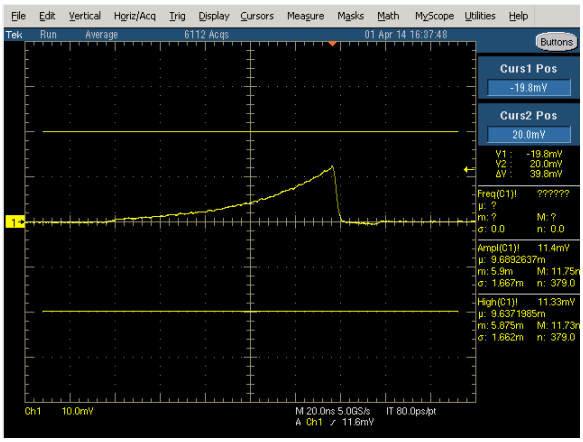

Figure 37: Square pulse input that has been shaped by applying an exponentially increasing signal to the EOM

From the measurements, it was apparent that the EOM was performing as expected and there were no unusual losses present. To test the EOM's capability to shape the pulses, an increasing ramp shape was applied. The expectation is that the beginning of the pulse will begin to peak as it passes through all of the power amplifiers due to saturation effects, and therefore to correct for these, the EOM needs to produce an exponentially increasing pulse shape. By applying the desired pulse shape to the RF input of the EOM, an exponentially

increasing optical pulse shape can be successfully produced, shown in figure 37.

The second modulation device used within the system is an acousto-optic modulator (AOM). The purpose of the AOM is to reduce the frequency of the system down to around 1kHz and remove any ASE build-up in between the pulses. The AOM behaves as described in section 3.2.3. By setting the frequency of the AOM to 1kHz and a pulse window of a few hundred nanoseconds, we can ensure that only one pulse from the EOM will be passed through the AOM every 1ms. As the pulse has already been shaped by the EOM, the AOM is only required to be open, using a square pulse, applied from the AWG. The AOM can either be biased open, to test the system at its fundamental frequency, or can be triggered by the AWG to down-sample the frequency to 1kHz. Initial tests suggested that the AOM was operating correctly in both scenarios.

4.1.4 Amplifier Configuration

Amplifier 0 (Amp0) is the only pre-amplifier stage in the MOPA2 system. The gain produced by this amplifier overcomes the inherent insertion losses of the modulators later on in the system. Amp0 consists of 5.5m of Nufern PM-YSF-HI fibre. Amp0 is pumped both forwards and backwards by separate 978nm diodes (Agilent F0427L). To connect the diodes to the amplifier, wavelength division multiplexers (WDMs) were used. The forward pump was connected through a hybrid WDM/Isolator. As the power at this point was relatively low, a high power isolator was not required, and the hybrid component saved additional splice loss, as well as the cost of an extra optical component. The WDMs enable the combination of the pump (978nm) and signal (1062nm) wavelengths to propagate down the same fibre. The pumps used for this were both capable of outputting a maximum of 300mW average power each. To relate the applied current to the output power of the diode during operation in the MOPA system, the pumps were first characterised.

Bi-directional pumping was chosen for this amplifier to provide enough gain, as it was expected there would be over 15dB loss to overcome. With only single direction pumping, the gain could not exceed this value, unless the pump was heavily over driven. Therefore, to alleviate the stress on the pump diode, we chose to run two diodes at slightly lower currents. With two pump diodes, it was possible to achieve over 20dB gain, and therefore compensate for all of the expected loss from the two modulators, as well as additional loss from the isolators and other components.

The current to the pump diodes are easily adjustable during operation, and therefore can be tuned to adapt to the operating condition. However, an initial condition of 200mA forwards (corresponding to 85.4mW) and 450mA backwards (corresponding to around 184.6mW) was opted for, as it minimised the amount of ASE generated, while still producing over 20dB of gain.

Amp1 was the first amplifier anticipated to begin to work towards the higher energy pulses that we required. To produce the targeted energy of hundreds of micro-Joules (required to reach energies in the targeted range for the output of the final OR-PAM system), it was necessary to have high gain amplifier stages, and therefore Amp1 was designed using a cladding pumped 10μm core ytterbium doped fibre (YDF). This stage was pumped using a JDSU-L3 High-Power pump diode, capable of producing up to 8.5W of power. The pump diode was calibrated, so that the output power could be known from the applied current.

To characterise the power amplifier, we examined the gain produced through the amplifier at various levels of pump power. The system was run at two different frequencies, 100kHz and 25kHz, to compare the performance of the amplifier. The results demonstrated that at lower frequencies, a higher gain can be achieved, reaching 17.8dB and 22.5dB at 100kHz and 25kHz respectively. This is due to the fact that, at lower frequencies, there is a longer time for the inversion to build up before the gain is extracted by the pulse. This leads to a higher gain being obtained. While measuring the gain, the pump power was only increased up to 4W as some saturation of the gain was already evident, a clear indication of the ASE build-up in between the pulses becoming dominant. The results taken at 25kHz are shown in figure 38.

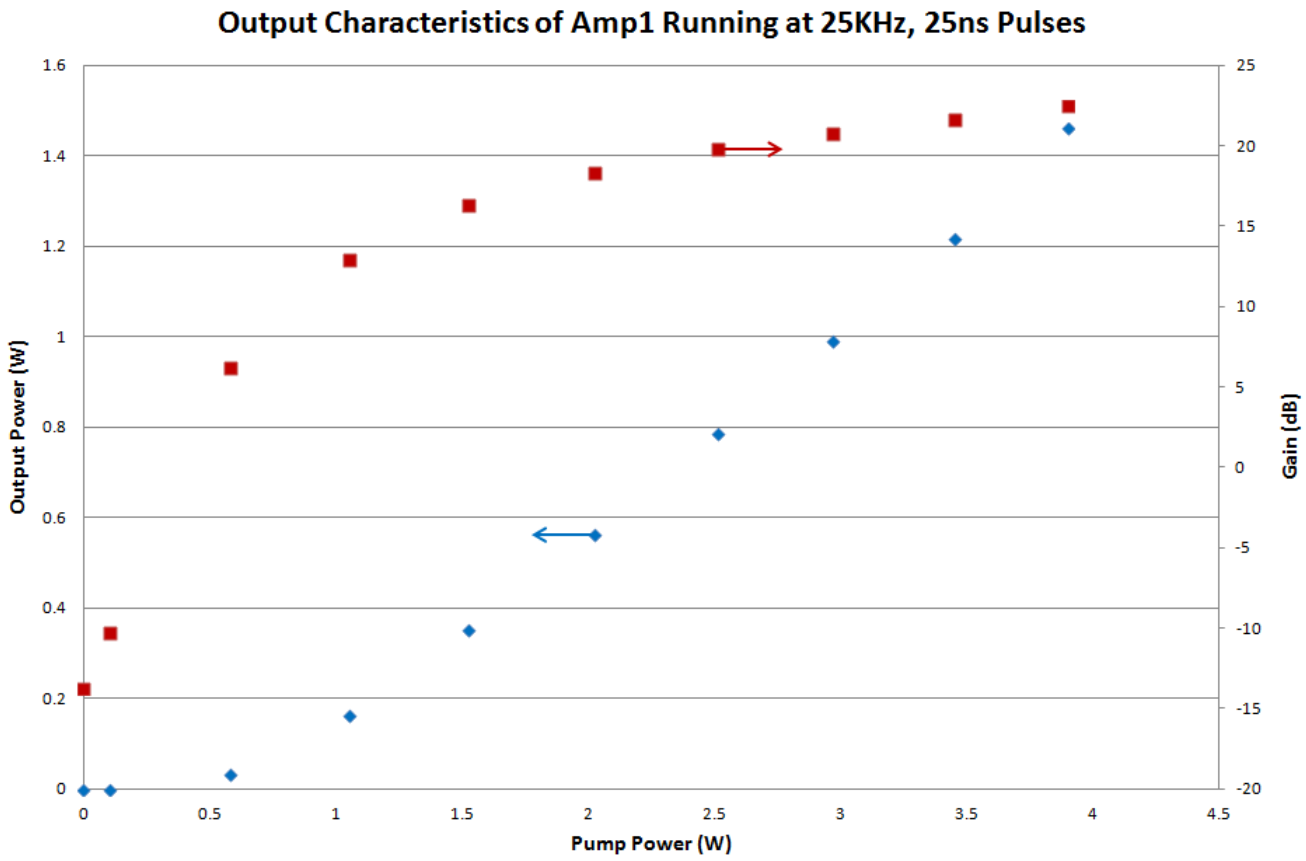

Figure 38: Results showing the output power and gain values for Amp1 at 25kHz using 25ns seed pulses.

The spectral data, shown in figure 39, was measured after splicing the AOM and the 1% tap to the system to allow an easy pick up of the spectrum through the forward tap port. The data collected indicates that there is a relatively large amount of spectral broadening, due to SPM, within this amplifier. The spectral width was measured, increasing from 0.2239nm at low pump power up to 0.553nm with 2.5W pump power. One reason that the broadening observed here is particularly large is due to long lengths of passive fibre after the amplifier. The passive fibre comes from the pigtails of both the AOM and the tap coupler, contributing over 1m of passive fibre between them. The passive fibre transmits the maximum peak power achieved in the amplifier for the whole length, as opposed to just at the end in the amplifier. This resulted in a larger chirp, and thus greater broadening. Although this broadening is significant, the amplifier will not necessarily be needed to operate much above 2W, where the gain begins to level off. It is also possible to go back and remove excess passive fibre from the system to optimise the performance, but this is best done after the final output conditions are known.

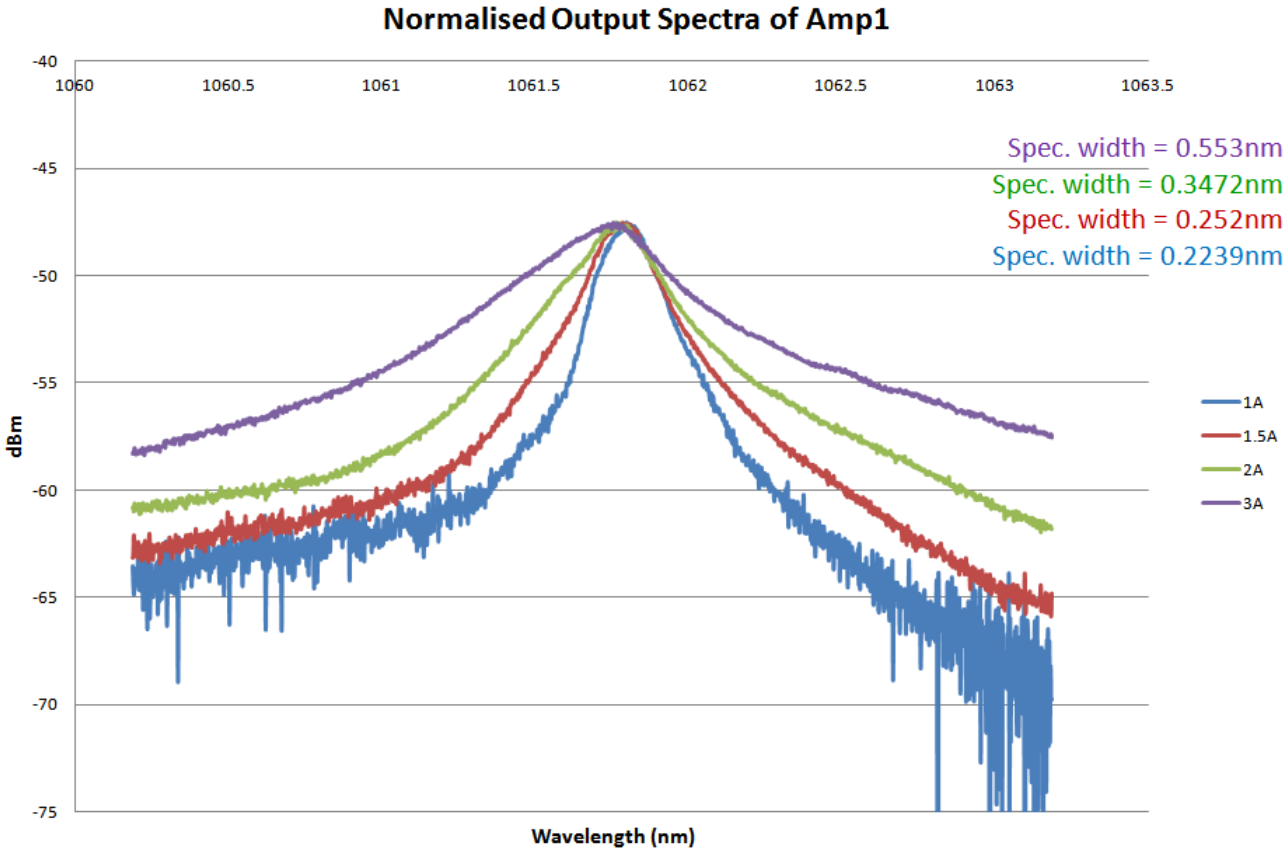

Figure 39: Normalised spectral measurements around the signal peak, showing how the spectral width varies at four different pump powers

Amp2 is the final amplifier in the MOPA2 system, and is used as a final boost to the output signal to reach the desired operating conditions. In order to keep the MOPA system fully fiberised, despite the increasing core diameter from Amp1 to Amp2, the final isolator used 10μm core fibre input and 25μm core fibre output pigtails. This allowed larger core fibres to be directly spliced onto the output of the final isolator. In an identical approach to that with Amp1, we used a fibre coupled pump combiner to couple the signal into the amplifier core, while simultaneously coupling the pump light into the cladding. For Amp2, an IPG-60W high power multimode diode was used.

The purpose of Amp2 is to dramatically increase the output signal of the MOPA system, and therefore to produce as much gain as possible. However, due to the increasing peak power within the system, the maximum output achievable is limited by non-linear effects such as SBS. Additionally, due to the need for a narrow bandwidth to efficiently frequency convert the signal, the output may be limited by spectral broadening due to SPM. In an attempt to be able to measure as many variables as possible in a single measurement, a series of wedges and dichroic mirrors were set up, as shown in figure 40. This set-up enabled us to simultaneously measure the output average power, the spectrum and the pulse shape, as well as providing the option to image the focus spot.

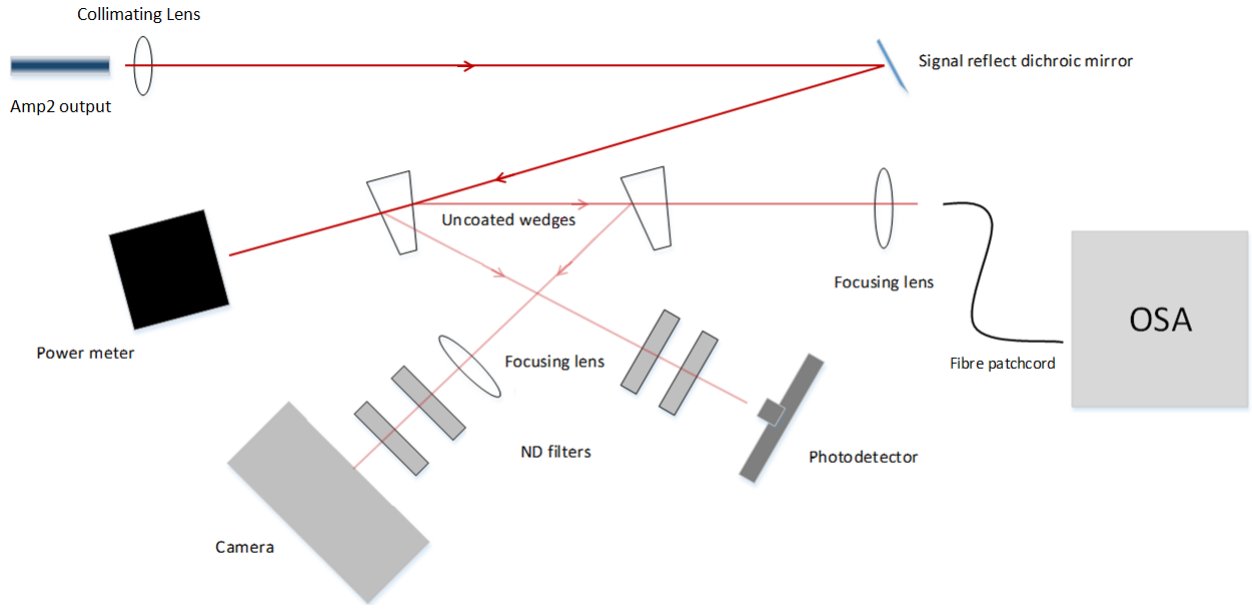

Figure 40: Schematic diagram, showing the set-up used to collect spectral, temporal and power data as well as the option of being able to image the beam.

Initial amplifier tests were carried out at a frequency of 25kHz, a seed pulse width of 100ns, and then carving this down to 50ns using the EOM. The results shown in figure 41 indicate that the amplifier is behaving as expected, and it was possible to successfully produce almost 3W of output power, having achieved a gain of 14dB from the amplifier for an input signal power of 100mW with a 3dB spectral bandwidth of 0.2332nm.

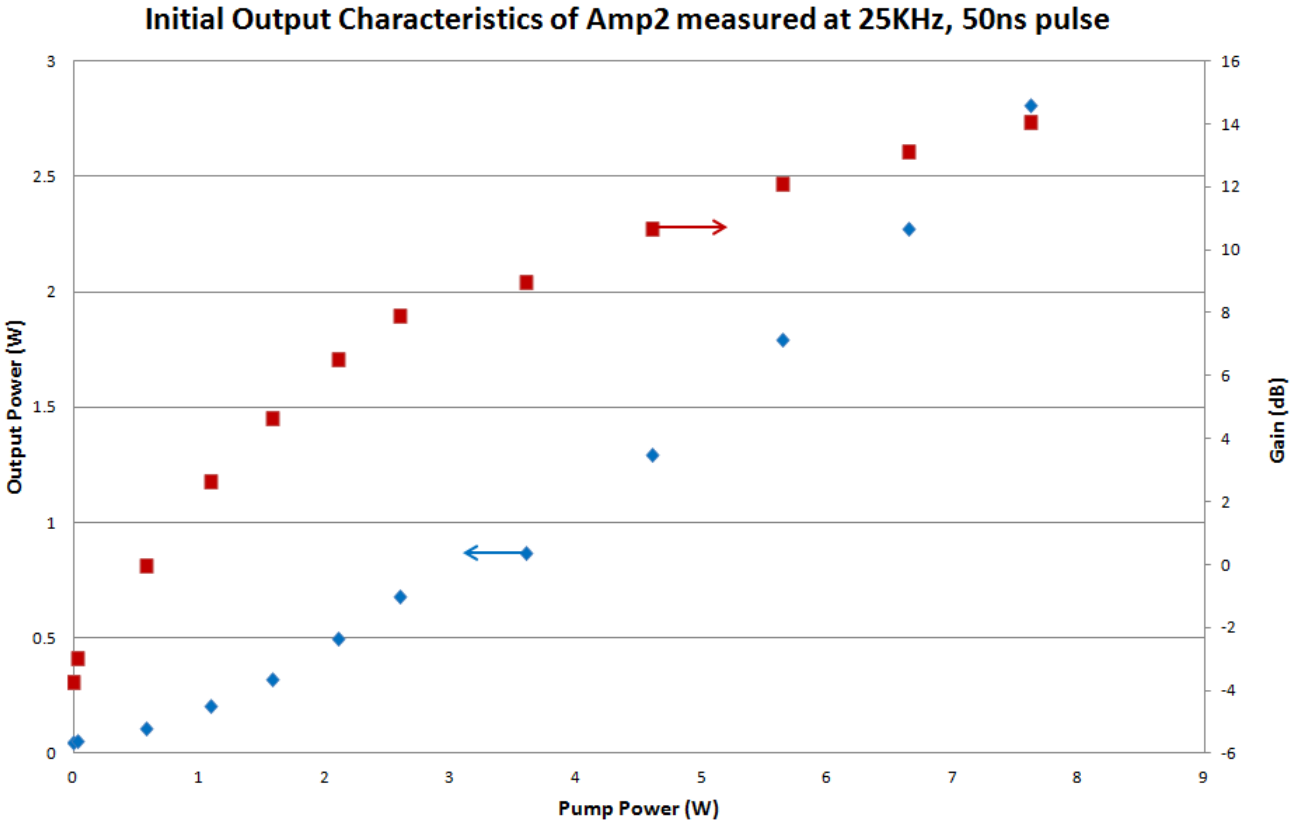

Figure 41: Plot showing the average output power and gain for Amp2. Measurements taken at a constant pump of 1.5W through Amp1

While running these initial tests, the backwards signal was monitored from both tap couplers within the system. It became apparent that there was some stimulated Brillouin scattering (SBS) taking place. Figure 42 shows the pulse in the backwards direction from the 5 % tap coupler, the horizontal yellow line indicates the average maximum signal. Approximately once every few seconds the pulse will peak significantly higher, as shown in figure 42. This is a characteristic sign that there is SBS within the system.

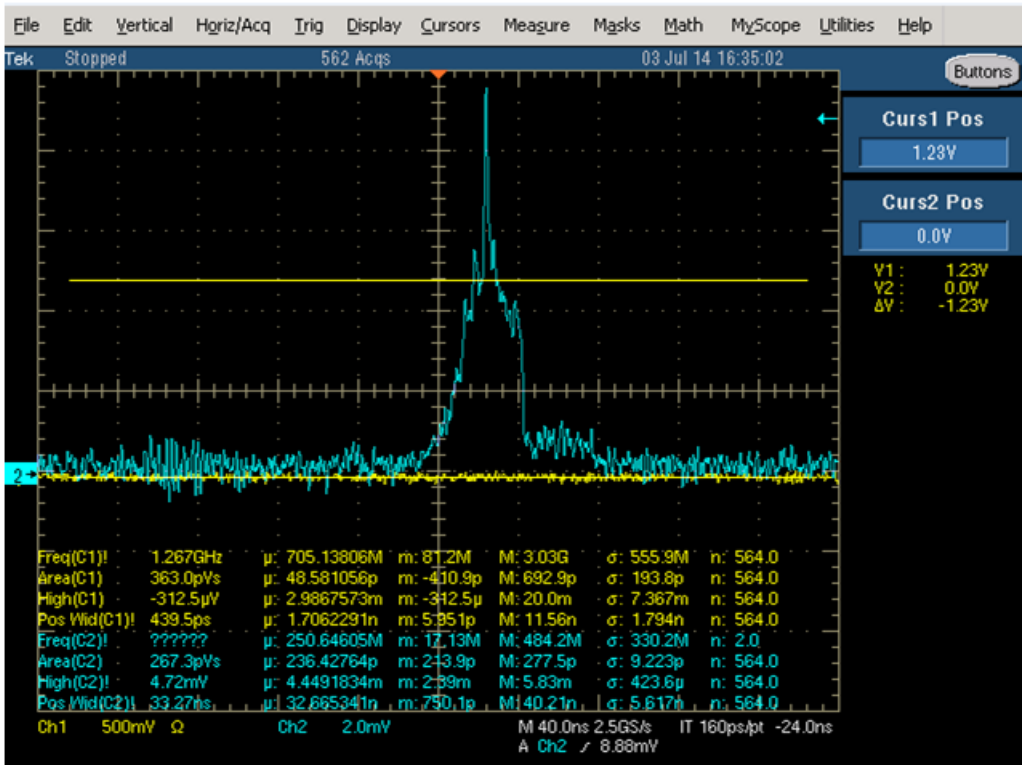

Figure 42: Oscilloscope trace showing distinctive pulse in the backwards direction, characteristic of stimulated Brillouin Scattering.

Within a MOPA system SBS can be highly destructive, as a high peak power pulse travelling backwards through the system can burn the amplifiers or even damage the seed. To resolve the issue of the SBS, the EOM opening duration was changed, as well as the seed pulse length. By monitoring in the backwards direction a 50ns seed pulse and a 12ns EOM opening time were deemed to be the best set-up, to retain as much power as possible, while producing little to no SBS. With the new pulse conditions, the output power was re-measured, shown in figure 43 as well as the spectral width. As the pulses going into the amplifiers were now significantly shorter, the resulting peak power within the amplifiers is much higher. This higher peak power will in turn lead to increased spectral broadening and thus it is crucial that the bandwidth is regularly measured to ensure that it does not exceed 0.7nm, the acceptance bandwidth of the SHG crystal. At the maximum pump power tested, 7.62W, the spectral width was measured to be 0.4784m.

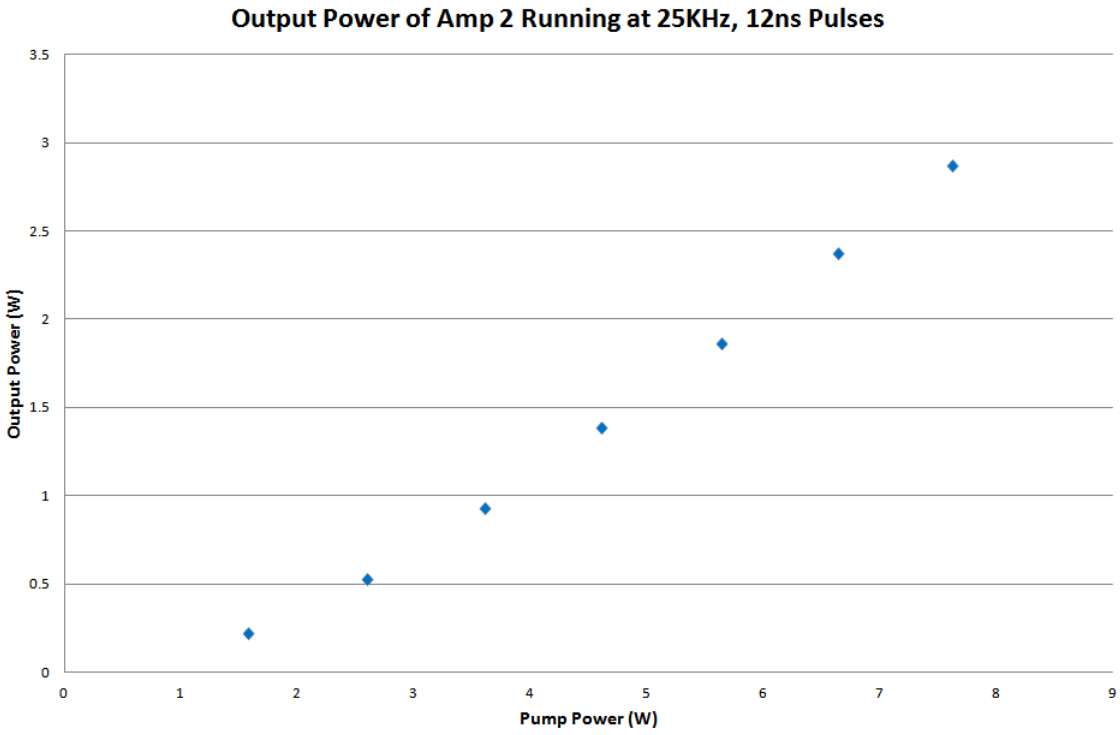

Figure 43: Output power taken at the output of Amp2 while running the system at 25kHz, 50ns seed pulses and 12ns EOM opening window

4.1.5 Amplifier Improvements

The first step to improving the output of Amp2, was to properly prepare the facet of the fibre. Up to this point, the end of the fibre had just been angle cleaved. By preparing an end cap to splice to the facet, the output will remain more uniform and also allow the beam to diverge to a larger spot, aiding in preventing catastrophic damage to the fibre facet. The end cap consisted of 5mm of 400μm coreless fibre, spliced directly onto a flat cleaved end of Amp2. With the end cap spliced on, the fibre was then mounted in a V-groove and clamped into position, so that the fibre tip could not move during measurements. The V-groove was then subsequently mounted onto a translation stage to give precise alignment. Directly after the fibre, a collimating lens of focal length 25mm was used to produce a collimated output, simplifying further measurements. The final optical element used to produce a clear and clean output was a dichroic mirror, reflecting wavelengths shorter than the 1060nm, while allowing the signal to pass through. This mirror removed any excess pump light still propagating with the output beam.

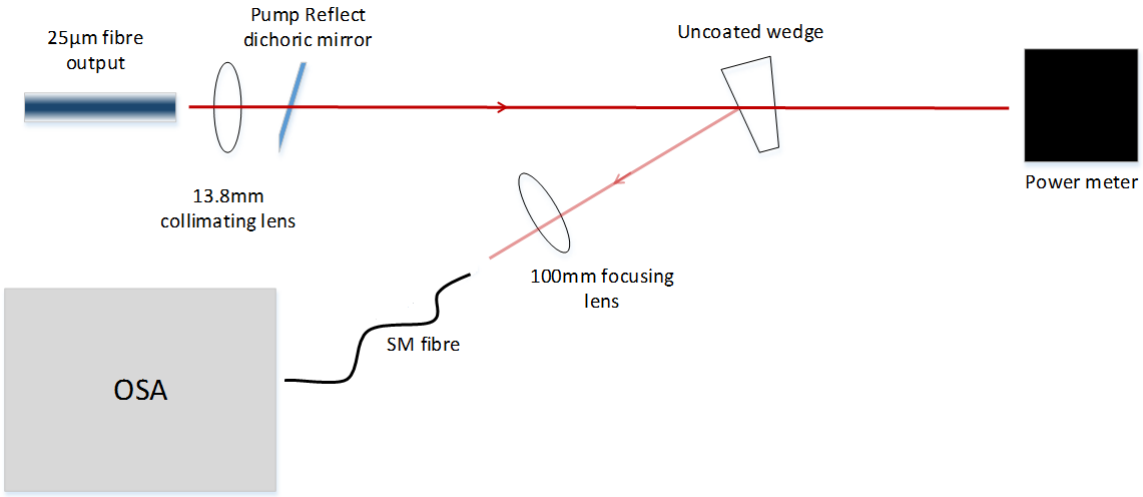

Figure 44: Schematic diagram of set-up used to measure output power, and simultaneously measure the output spectrum from Amp2.

Before running additional tests, the diagnostic set-up was refined, to reduce the number of optical components that could add distortions or interference to the measurements. The refined set-up, shown in figure 44 can measure the output power of the system, while simultaneously measuring the spectrum. The light coupled into the OSA is now focused into a fibre, which is mounted on a translation stage, to stop the fibre from moving and providing the most freedom to adjust its position to maximise the coupling.

Spectral measurements were taken while running the system at both 25kHz as well as at 100kHz, allowing for comparisons to be made between the two. In order for the comparison to be meaningful, the peak power must be equal in both cases. Therefore, the tests carried out at 100kHz were pumped to an average output power four times that of the test at 25kHz. As shown in figure 45 there was significant power at 1114.45nm which increased with the pump power. This suggested that the peak was due to some non-linear contribution. In order to determine if this is the case, the frequency shift from the signal peak can be investigated. A shift of 13.3THz matches that of the calculated Raman shift in germanosilicate fibre[35]. The Raman peak can also be identified while the system is running at 100kHz, shown in figure 46.

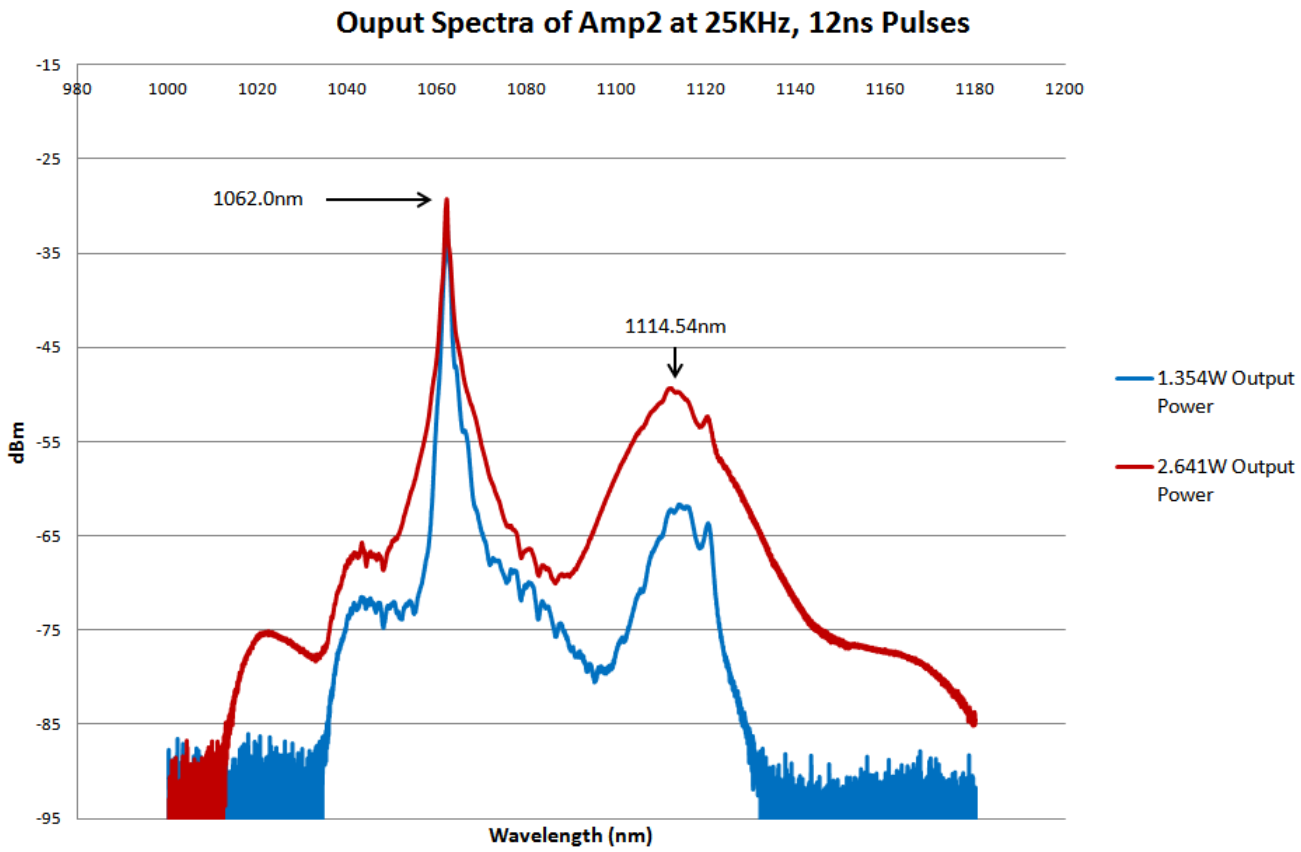

Figure 45: Spectral data from the output of Amp2 after new pulse duration of 50ns from the seed, then cut down to 12ns by the EOM. Spectral features peak wavelength labelled.

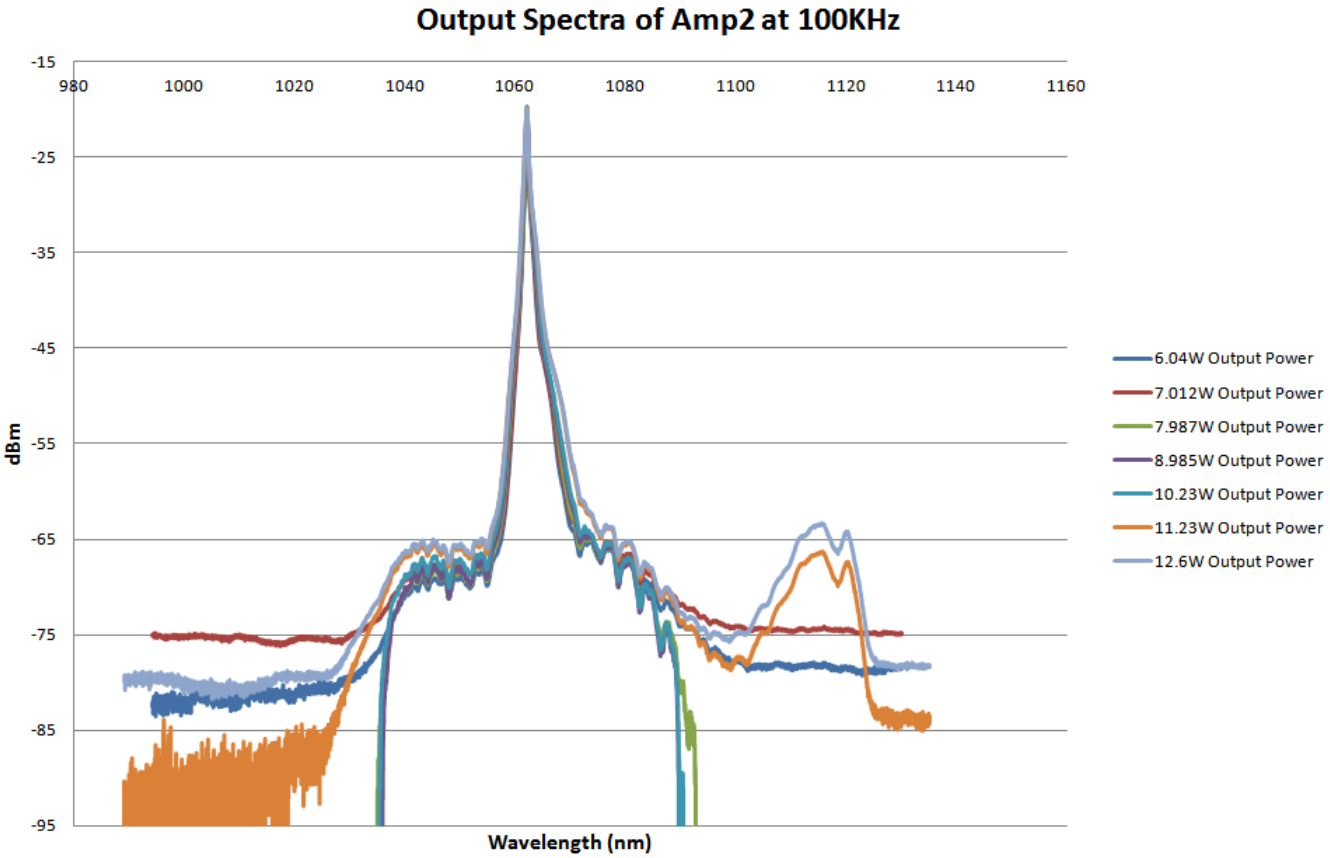

Figure 46: Spectral data taken at 100kHz measured at the output of Amp2. Measurements taken at a constant pump of 2.361W through Amp1.

From both figure 45 and 46, it is apparent that there is a larger Raman peak signal when the system is running at 25kHz. Despite the attempts to match the average outputs of the system, by increasing the pump power to the second amplifier, it was noted that there was no corresponding corrections made to the first amplifier stage. This led to there being a significantly higher input peak power to Amp2 when the system was running at 25kHz. This higher input will have in turn increased the Raman signal produced due to the larger non-linear effects present. This error was further confirmed when looking at the spectral bandwidth of the output signals, shown in figure 47. The bandwidths are consistently higher when the system was running at 25kHz. Despite this, it was clear that the increasing pump power was steadily increasing the non-linear broadening of the output signal in both cases.

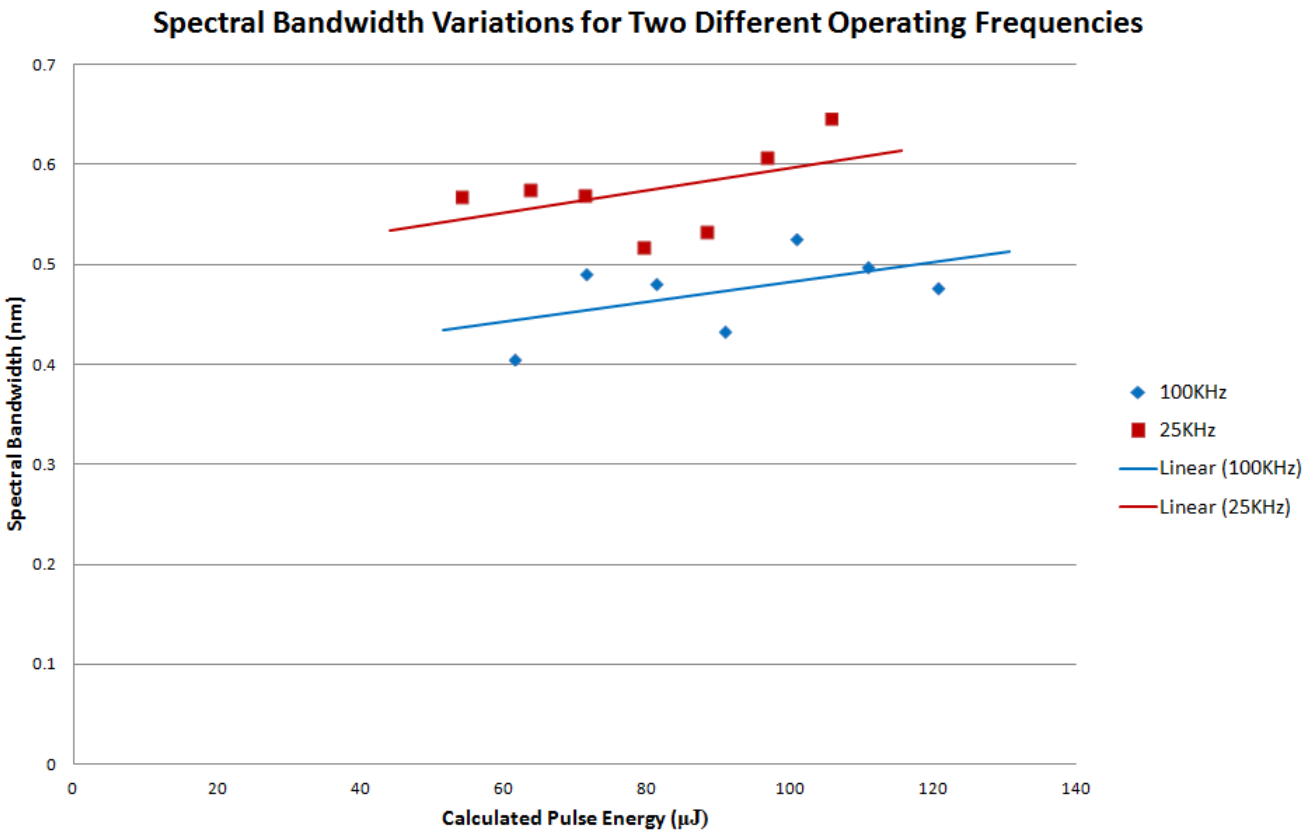

Figure 47: Spectral width at increasing output pulse energies, measured at two operating frequencies.

The only concern with the 100kHz results is the inconsistent spectral shapes as the pump power is increased, as well as the spectral bandwidth occasionally being lower at a higher pump power than other results at lower pump powers. To try to determine if this is systematic error or not, six different measurements were taken all at a pump power of 24W. The first test was taken after switching the system on and increasing the pump power up to 24W. In the second test, the pump power was increased above 24W, and then adjusted back down. The third test was taken after approximately 5-10mins of the system running at 24W. After recording the results from these three tests, the system was shut off and left for 10-20mins. After this, the system was restarted and the same 3 tests taken again. The results shown in figure **??** show the fluctuations test to test. These results indicate that there is some small discrepancy between the measurements but in general they have very similar spectral content. The spectral width of each measurement was also recorded, and an average of 0.51nm was calculated, with any individual measurement being within 5% of the average.

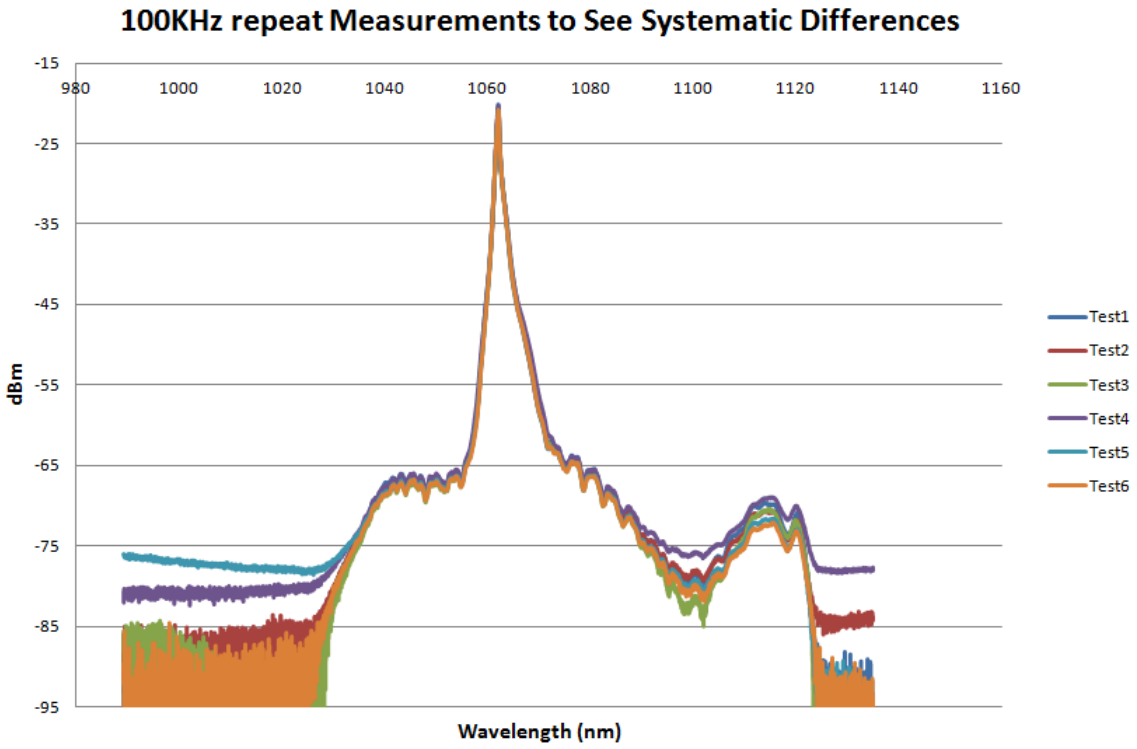

Figure 48: Repeat measurements all taken at the same condition at 100kHz with a pump power of 24W.

As mentioned previously, the OR-PAM system has a strict requirement on the beam quality. Most of the fibres within the MOPA2 system are intrinsically single mode, and therefore should cause no problem. However, the 25μm core fibre can support the first higher order mode, that could potentially increase the M^2 value of the output. In order to measure the beam quality of the output, an automatic scanning slit device was used (Thorlabs BP209-IR - Dual Scanning Slit Beam Profiler). The device is able to produce an image of the output beam, as well as determining both the dimensions of the beam and the intensity profile, and thus it is able to calculate the beam quality. To measure the beam quality of the MOPA2 output, a simple set-up was used, whereby the output is first collimated, and then focused onto the profiler. The profiler's position is then adjusted to inspect the beam on either side of the focal point to gather information regarding the divergence, to allow it to calculate the M^2 value [38].

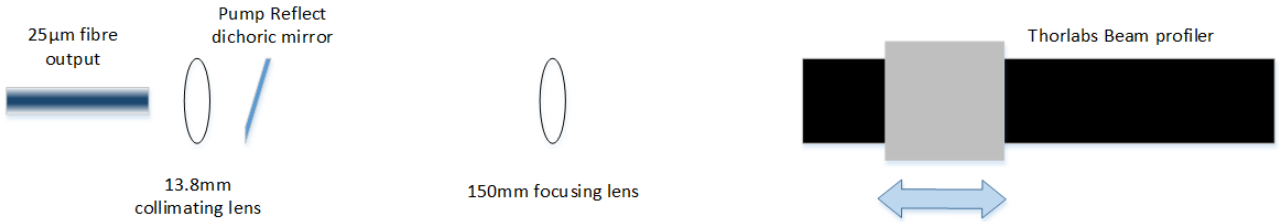

Figure 49: Schematic diagram showing the set-up used for M^2 measurements. Thorlabs Beam profiler was computer controlled and its position was automatically moved during measurements.

When running some initial tests with the set-up described in figure 49, ring patterns were observed over the beam profile. The rings appeared to have been produced by some diffraction effect, and were causing the results of the profiler to be inaccurate. After swapping around optical components, it was apparent that the 25mm collimating lens was causing the problem. This was simply resolved by using an aspheric lens, as opposed to the bi-convex lens that was being used. The new collimating lens had a focal length of 13.8mm, and thus created a smaller spot. However, using this lens allowed a clean M^2 measurement without any interference.

In order to control the higher order modes within Amp2, the fibre was coiled to a diameter of 70mm. This was expected to cause any higher order modes to leak out of the fibre, resulting in the propagation of only the fundamental mode. In order to test this, the M^2 measurement was first carried out with the 25μm not coiled, allowing some propagation of the higher order modes. Figure 50 shows some clear distortions from the expected circular shape. This is particularly clear on the profile before the beam waist, where the spot is elliptical in both axes. This is a sign that there are additional higher order modes propagating through the fibre. The next measurements were taken after coiling the fibre to a diameter of 70mm.

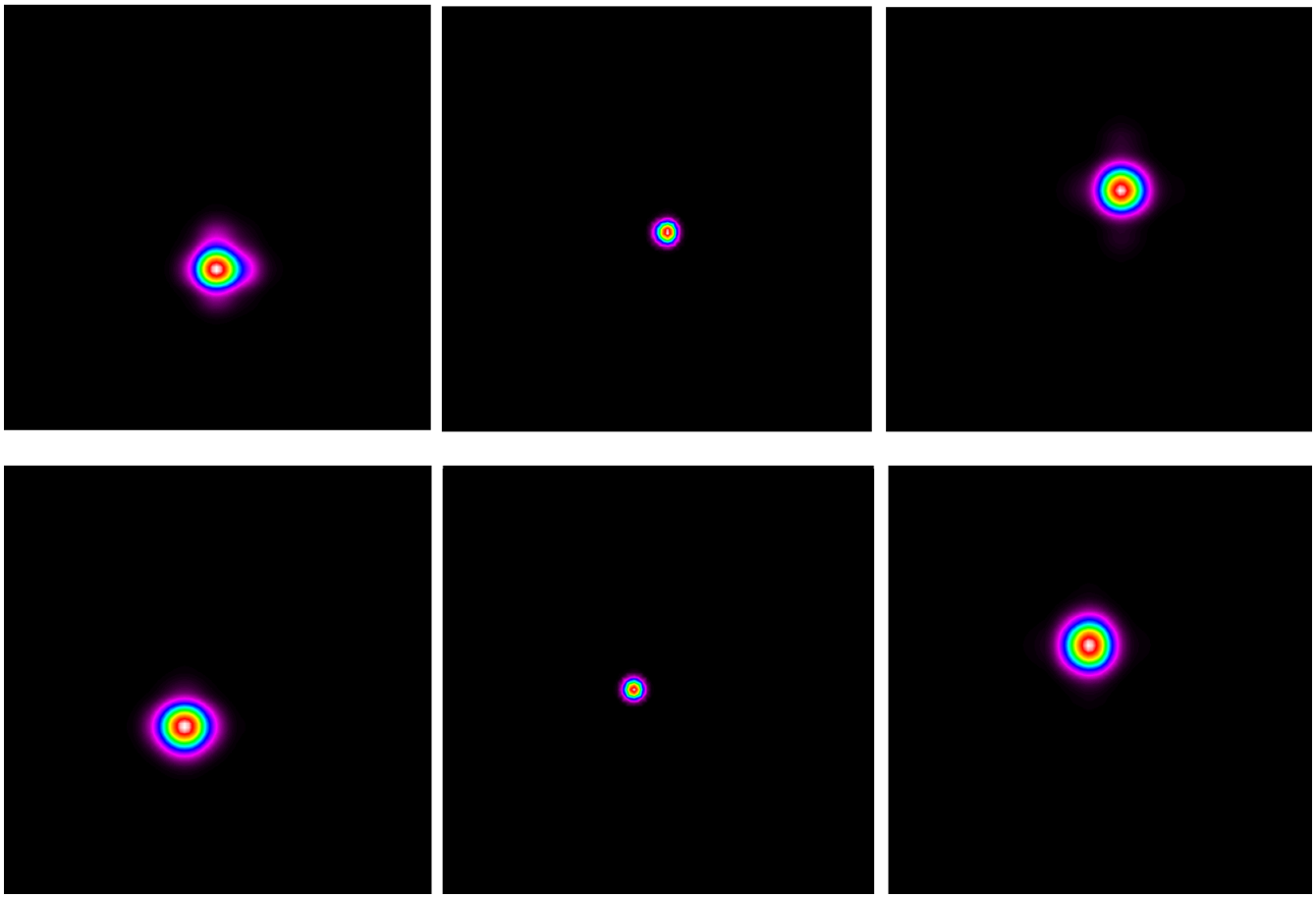

Figure 50: Top: Images showing the beam profile with the fibre uncoiled at various positions, before the beam waist, at the beam waist and after the beam waist, in order. Bottom: Same measurements taken again, this time with the fibre coiled to a diameter of 70mm.

The beam profiles taken after coiling the fibre, shown at the bottom of figure 50 show a much more spherical nature, and thus an improved M^2 value. In order to determine the value of M^2, the beam diameter data, collected by the profiler, was fitted against a perfect Gaussian beam, following equation 41. A Matlab program, written by Dr Zhihong Li, was edited to fit the operating conditions and data collected, and was able to determine the M^2 values, shown in figure 51

$$\omega(z) = \omega_0 \sqrt{1 + \left(\frac{z}{z_R}\right)^2} \tag{41}$$

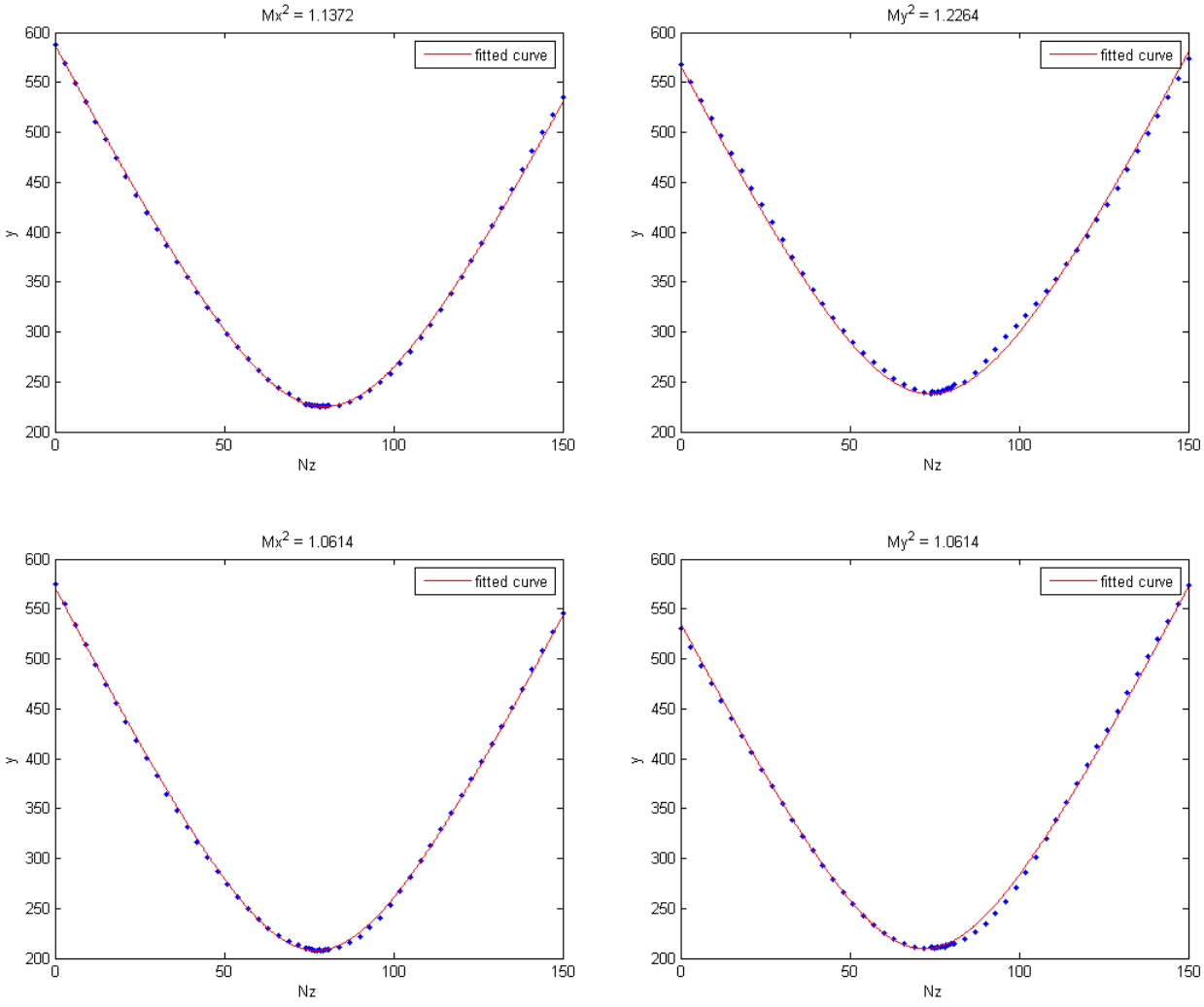

Figure 51: Measured data fit via a program to determine the M^2 value. Top: Uncoiled fibre. Bottom: Coiled fibre

The measured values of the M^2 were 1.18 and 1.06 for the uncoiled and coiled fibre respectively. This information indicates that the coiling of the fibre successfully removes the higher order modes. Additionally, since the value of the M^2 is less than 1.2, and close to one, the output is almost single mode and is within the limits of the project definitions.

4.1.6 Conclusion

The initial approach to developing an OR-PAM system, was to base the design on the already successful PAT system. Due to the desire to keep the system size to a minimum it was decided to use a FP diode as the seed rather than an ASE source. Both an EOM and an AOM were placed within the system to allow for pulse carving, shaping and frequency reduction. This would enable the system to operate as both a PAT and OR-PAM system. Although initial tests were successful with both modulators performing suitably, there was a significant issue of broadening as well as the detection of initial SBS signatures. Improvements were made to the system in the form of reducing the pulse width to 12ns, coiling the final amplifier to remove higher order modes, and using aspheric lenses. With these improvements to the system we were able to remove any sign of SBS, as well as produce a clean beam with an M^2 value of less than 1.2. However is was apparent that as the system was pumped harder, significant non-linear effects began to appear, most noticeably SRS. Based on the results, it was apparent that the use of extra components, such as the two modulators, added significant fibre length via the component pigtails. This resulted in limiting the potential power that could enter the final amplifier stage, leading to the need for high gain. To resolve the problem the system needs to specifically target OR-PAM only, removing un-necessary restrictions on the system given that a PAT system is already operational.

4.2 Amplified Spontaneous Emission (ASE) Injection Locking System

4.2.1 Introduction

The previous design of the MOPA2 system worked as intended, however with the two modulators, the system required a large number of power supplies reducing portability. Also the modulators were particular weak points in the system, limiting the peak power early on in the system. Consequently, to develop the system into a more practical and portable system, the decision was made to remove the modulators. Removing the AOM only limited the ability to run at low repetition rates of around 1kHz. This posed little problem as the operating repetition rate for the OR-PAM is in the order of hundreds of kiloHertz to MegaHertz. Removing the EOM had a much more significant impact on the system, as the short pulses would have to be generated directly from the seed. When an FP diode was used in the portable PAT system, there were issues with SBS, resulting in the need to significantly dither the signal. The difference in the OR-PAM is that required pulse widths need to be between 0.5 - 10ns. If short enough pulses can be generated ($< 5ns$) then the threshold for SBS will be increased significantly, due to the pulse width being notably shorter than the phonon lifetime. To achieve locked short pulse generation from the FP diode, an injection locking set-up was implemented.

Injection locking is based upon the idea of forcing a, 'slave', oscillator to oscillate at an applied frequency from a 'master' oscillator. Providing the frequency of the master oscillator is sufficiently close to that of the free running slave oscillator and a good coupling between the two oscillators is established. As a result, the master oscillator can influence the slave, essentially forcing it to oscillate at the same frequency as the master oscillator. This principle works with all forms of oscillators, from pendulum clocks, to lasers. In terms of lasers, a weak locking signal can be injected into a laser, forcing the laser to oscillate at the applied frequency, as shown in figure 52. Using this technique, a seed laser can be locked to a specific required frequency, as well as within the applied bandwidth. This is beneficial within our experiment as it provides a method to produce narrow band seed pulses at 1064nm.

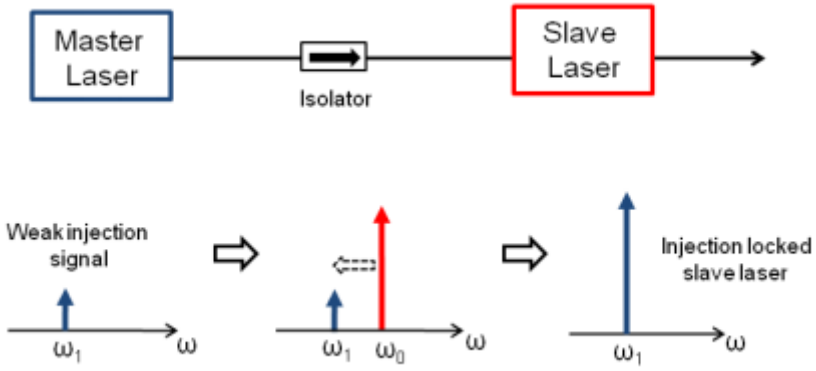

Figure 52: Basic diagram explaining the principles of injection locking. A weak applied locking signal causes the slave laser to oscillate at the applied frequency ω_1 [50]

By injection locking the FP diode, it is anticipated that multiple longitudinal modes can be locked within a shorter time frame, than in the case with a FBG. By locking multiple modes quickly, the chance of single modes locking will decrease, which in turn will increase the threshold for SBS. Moreover, by basing this system around injection locking, it will be possible to compare the pros and cons of an injection locking set-up to an SLED set-up, giving a better understanding as to whether one technique is more suitable than the other.

4.2.2 ASE Locking Source

The modified MOPA2 system, shown in figure 53, uses a FP seed diode, that is injection locked via an amplified and spectrally filtered ASE source. The output of the FP diode is then amplified via two LMA fibre amplifier stages; one 6m stage based on Nufern PLMA YDF 10/125 and a second 2.5m stage based on Nufern PLMA YDF 25/250 fibre. Due to the removal of the modulators, the system no longer needed a core pumped pre-amplifier stage, as enough gain could be achieved without it. Table 2 shows the estimated power budget of the system, taking into account insertion losses, indicating that a gain of 26dB from the first amplifier, and a gain of 22dB from the second, will be able to produce an output signal with peak powers in excess of 10kW.

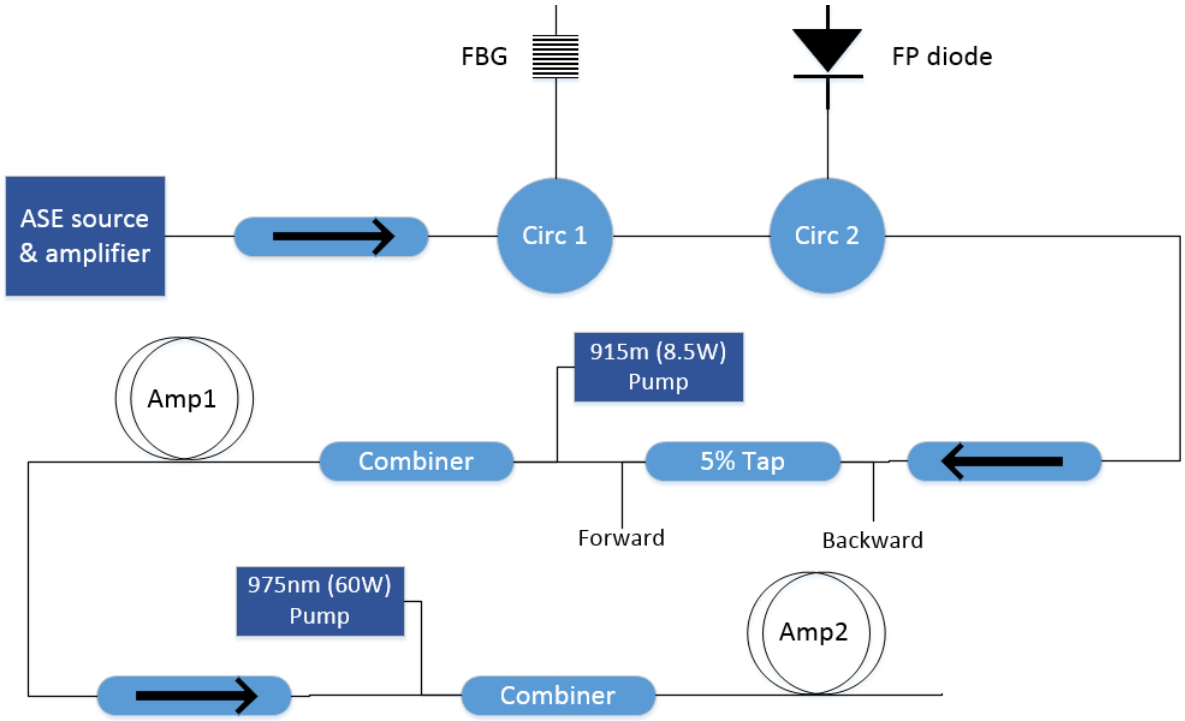

Figure 53: Schematic diagram showing the injection locking set-up. ASE source and amplifier used as the master oscillator injected into a FP diode. The seed output is then amplified by two fibre amplifiers

Table 2: Power Budget at 100kHz, for 10ns pulses

	Seed	**Loss 1**	**Amp 1**	**Loss 2**	**Amp2**
Gain (dB)	-	-3	28	-1.5	23
Peak Power (W)	0.3	0.15	94.87	67.16	13.4×10^{3}
Average Power (W)	3.00×10^{-4}	1.50×10^{-4}	9.49×10^{-2}	6.72×10^{-2}	13.4
Average Energy (J)	3.00×10^{-9}	1.5×10^{-9}	9.49×10^{-7}	6.72×10^{-7}	1.34×10^{-4}

The initial focus of the experiments was concentrated on producing a suitable signal from the ASE source to be used to lock the FP laser diode. The locking signal needs to have a suitably narrow bandwidth, so that the locking power is contained within the desired wavelength region. Typically the bandwidth of an ASE source is very large, as shown in figure 54, the two ASE sources tests had a 3dB bandwidth of 10.16nm and 28.1nm respectively. The following experiments were conducted with the higher power ASE source, as, despite being centred around a lower wavelength, the power at 1064nm was still higher than the other source.

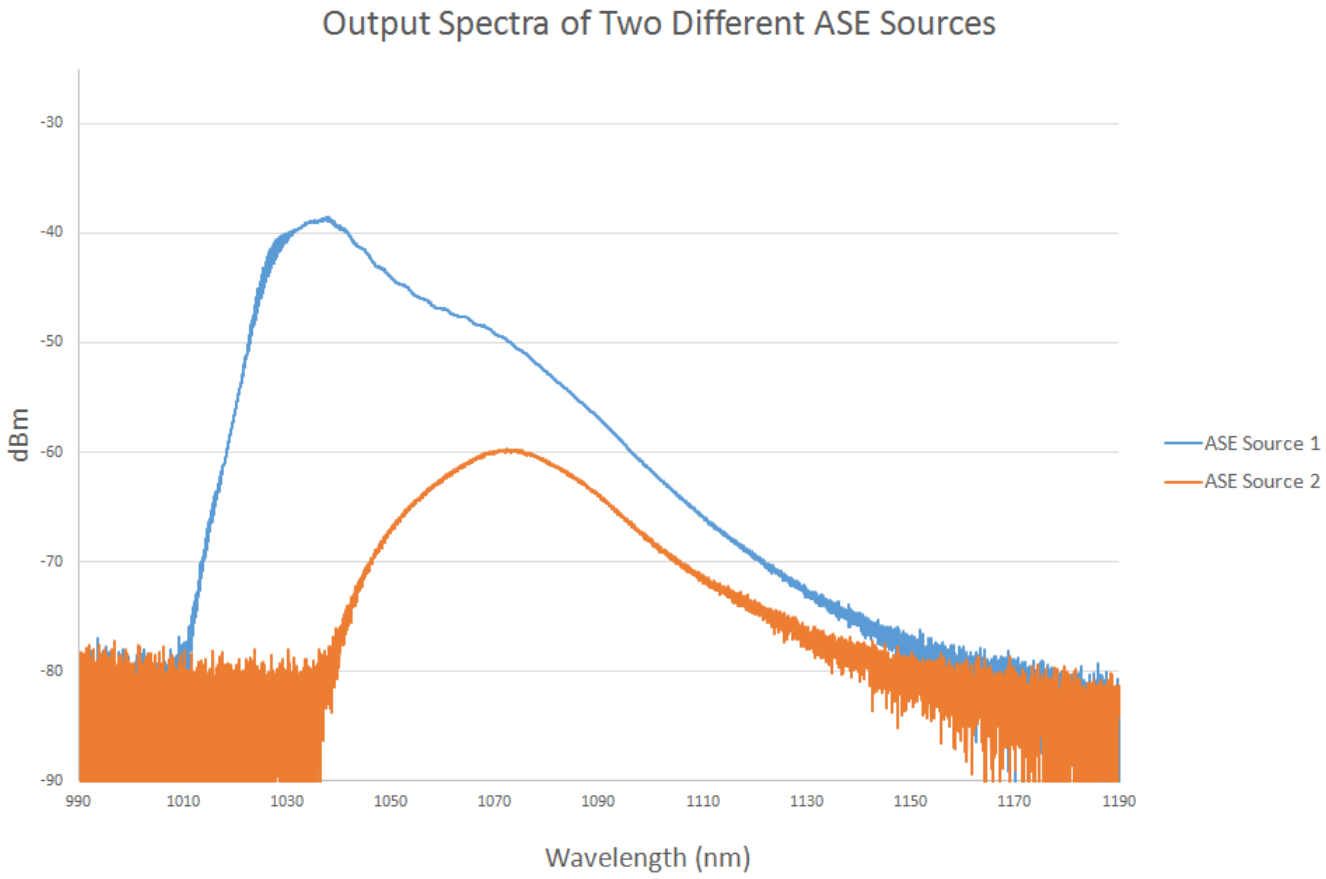

Figure 54: Spectral measurements taken for two different ASE sources

Therefore, to use the ASE source as a locking signal, it first needed to be spectrally filtered. The process of filtering the ASE source significantly reduced the maximum power of the ASE power. By using a 3nm band pass filter at 1064nm, the power will be significantly reduced, the filter is not only selecting a 3nm portion of the spectra, but the portion selected is not around the peak value. The power measurements indicated that the power was reduced from 33.60mW to 312μW, after passing through the 3nm band pass filter. With significantly lower power than desired, and still too broad, the 3nm spectrum then needed to be amplified before being filtered further using a FBG, and finally being injected into the FP diode. This was achieved by connecting the output of the band pass filter to a fibre amplifier stage. The amplifier stage consisted of 3m of core pumped 5/120μm fibre. The source was now capable of producing 18.35mW at the output of the ASE source & amplifier stage, shown in figure 53.

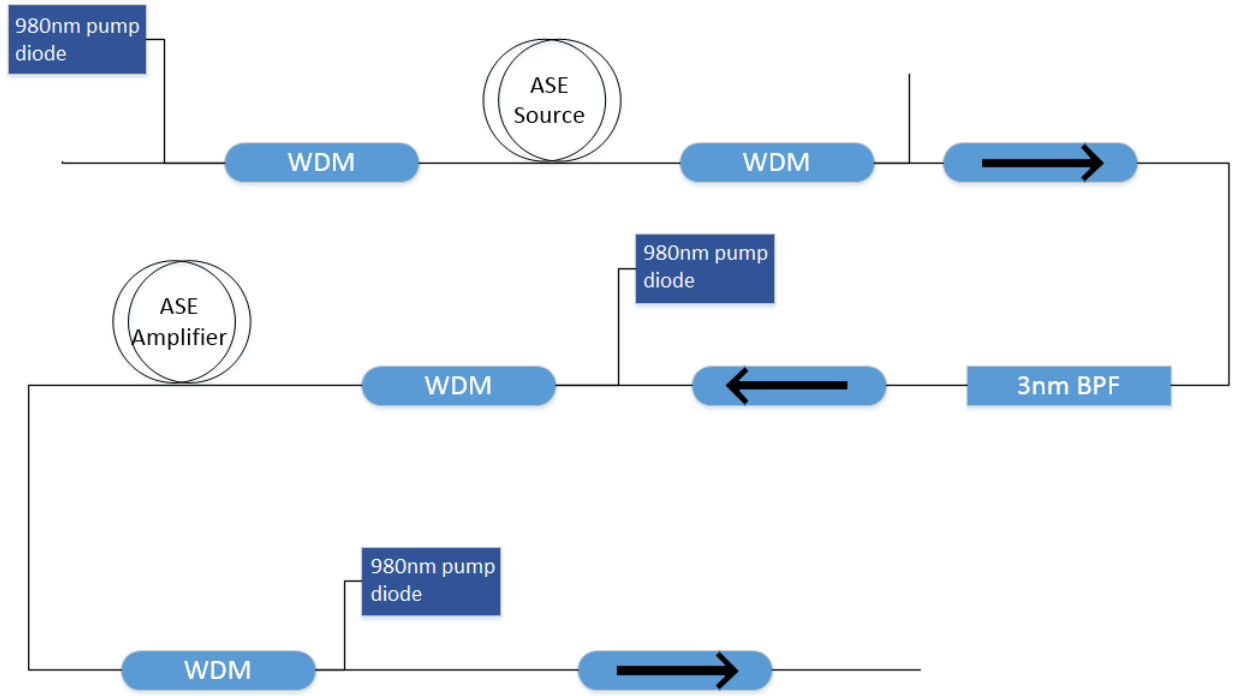

Figure 55: Schematic diagram of the ASE source and amplifier used to injection lock the FP diode. WDM: Wavelength division multiplexer

Before the output of the amplifier ASE source could be integrated to the rest of the system, the output fibre needed to be polarisation maintaining (PM). To achieve this, a final isolator was spliced to the output of the amplified ASE source. The final ASE and ASE amplifier set-up is shown in figure 55. Due to the change from non-PM to PM fibre, the power was reduced to 6.390mW. Before injection was possible, the spectrum needed to be further reduced in bandwidth. This was achieved with the addition of a narrow, 0.2nm bandwidth FBG. However, since the region of the spectrum we required is reflected from the FBG, the system was set up to include a circulator. This allowed us to easily connect the amplified ASE to the FBG, and then the narrowed spectrum could be retrieved in a separate fibre port. This signal was then injected into the FP diode, and thus a second circulator was used, to allow the injected signal to enter the diode through port one, and the output from the diode to exit through port 3, seen in figure 53.

Before splicing the FP diode to the circulator, the power and spectral width was measured at the output of port 2 of circulator 2 to be 125.8μW and 0.2nm respectively. To determine the effect of the injection locking, the FP diode was first run on its own, to obtain the free running spectral data. This was then compared with the results obtained when the diode was injected with the signal from the amplified and filtered ASE source, as shown in figure 56.

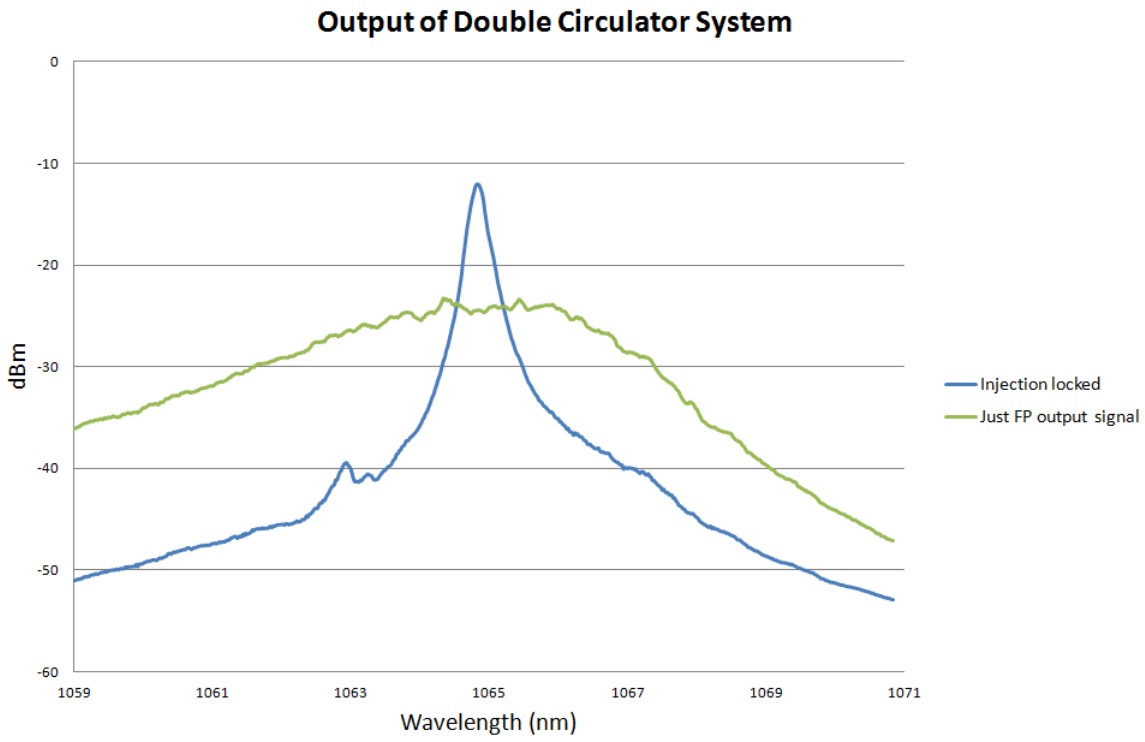

Figure 56: Output spectra for the FP seed diode with and without an injection locking signal from the amplified and filtered ASE source

4.2.3 Amplifier Configuration

The ASE seed source was run at a maximum power in initial locking test, and therefore there was no evidence that the result obtained was the best locking condition possible. Consequently, a 5.5m core-pumped amplifier was placed between Cir1 and Cir2 on figure 53. This way we could simply increase the amplifier pump current, in turn increasing the amount of power within the locking signal. The amplifier was pumped with 20mW to account for the loss, so that an accurate comparison could be made both with and without the additional amplifier. Pumping the amplifier with up to 110mw, the output signal showed no improvement, and a slight increase in the level of ASE. Therefore, it was concluded that the co-pumped amplifier was unnecessary, and it was removed from the system.

One advantage of using this injection locking technique is the ability to lock shorter pulses than was previously possible, when using an FBG. Previously the system had to run pulses in the order of 50ns to get a good lock, and then with the addition of the EOM, cut the pulse width down to tens of nanoseconds. Figure 57 shows the injection locking set-up is able to lock pulses as short as 4ns. Attempting to lock pulses any shorter results in a significant amplitude reduction, partly due to the internal impedance of the FP seed diode.

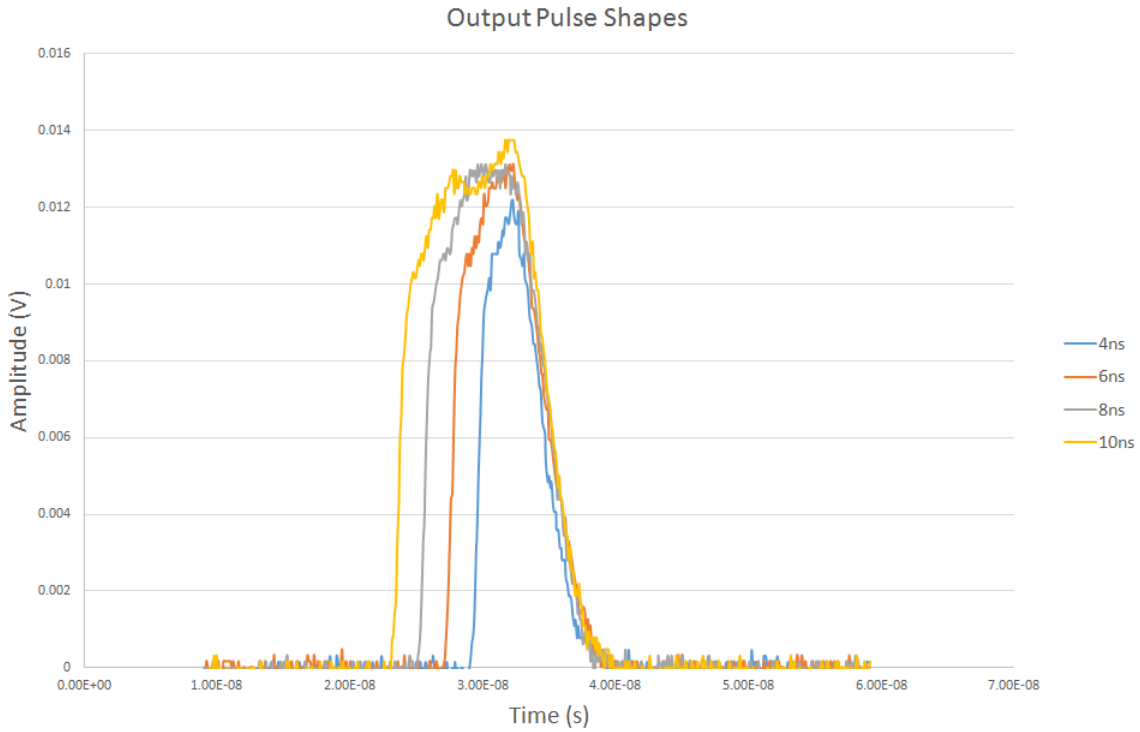

Figure 57: Output pulse shape recorded using a fast photodetector connected to a 500MHZ 1Gs/s oscilloscope

With the system successfully locking a range of pulse widths, it was necessary to rebuild the amplifier stages to bring the power back up to a comparable level, as measured with the previous MOPA2 set-up. The first amplifier, 6m of Nufern PLMA YDF 10/125 fibre, was targeted to reach an output peak power of 95W, as shown in table 2. By further increasing the peak power, we would also be able to verify if the injection locking system experiences a significantly higher threshold for SBS. In order to monitor the SBS within the system, a 5% tap was placed before the amplifier, this way the SBS could be measured through the backwards port via a fibre connected photodiode. Initial tests of the amplifier were carried out at a frequency of 100kHz, and a pulse width of 10ns, which resulted in an output power from the locked FP diode of 0.251mW.

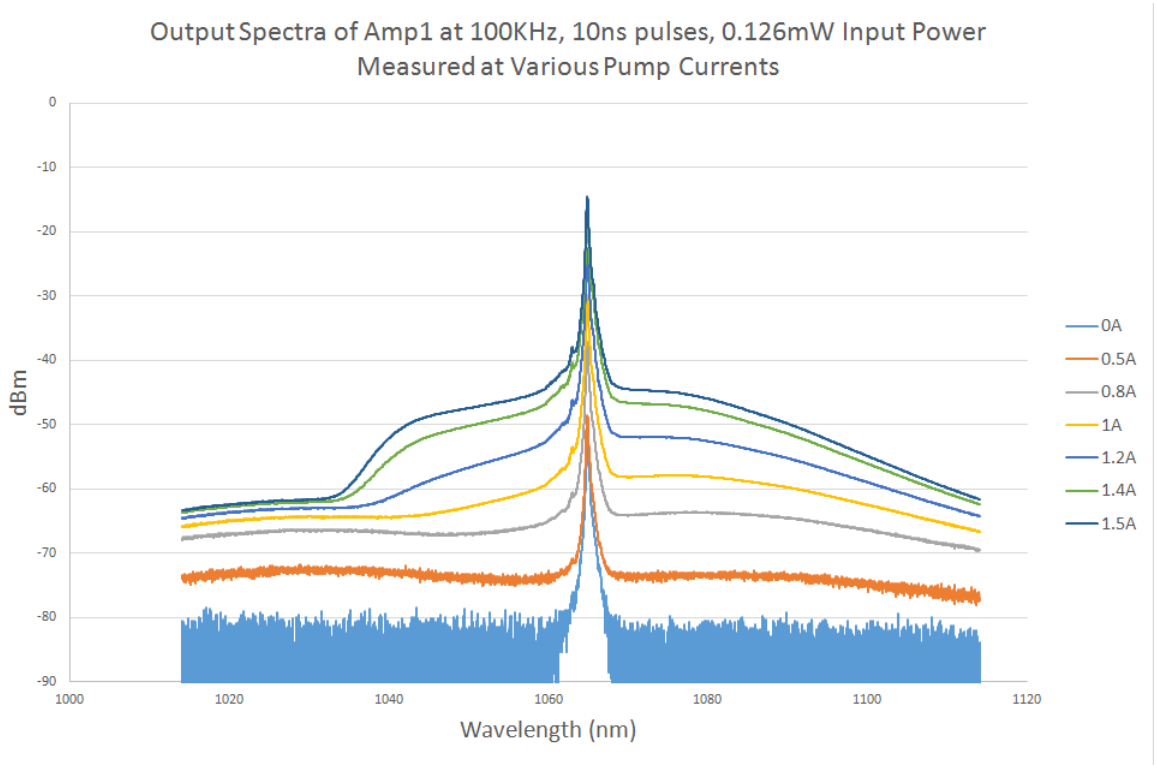

Figure 58: Output spectra from the first amplifier, measured at 100kHz using a 10ns pulse width

Figure 58, shows the spectral results measured from increasing the pump power up to 1W. From the initial data shown, it is apparent that as the pump power increases further, there will eventually be an issue with a build-up of short wavelength ASE. However, at a pump current of 1.5A (corresponding to a power of 1W), the system was already producing an output power of 97.9mW, corresponding to a gain of more than 28dB. Despite the relatively low pump power, the amplifier was already able to reach the targeted output characteristics, as set by table 2. However, in order to see how the amplifier performs at higher pump powers, and also to investigate the SBS threshold levels, the pump power was increased further up to a maximum value of 5.8A (corresponding to a pump power of 5W).

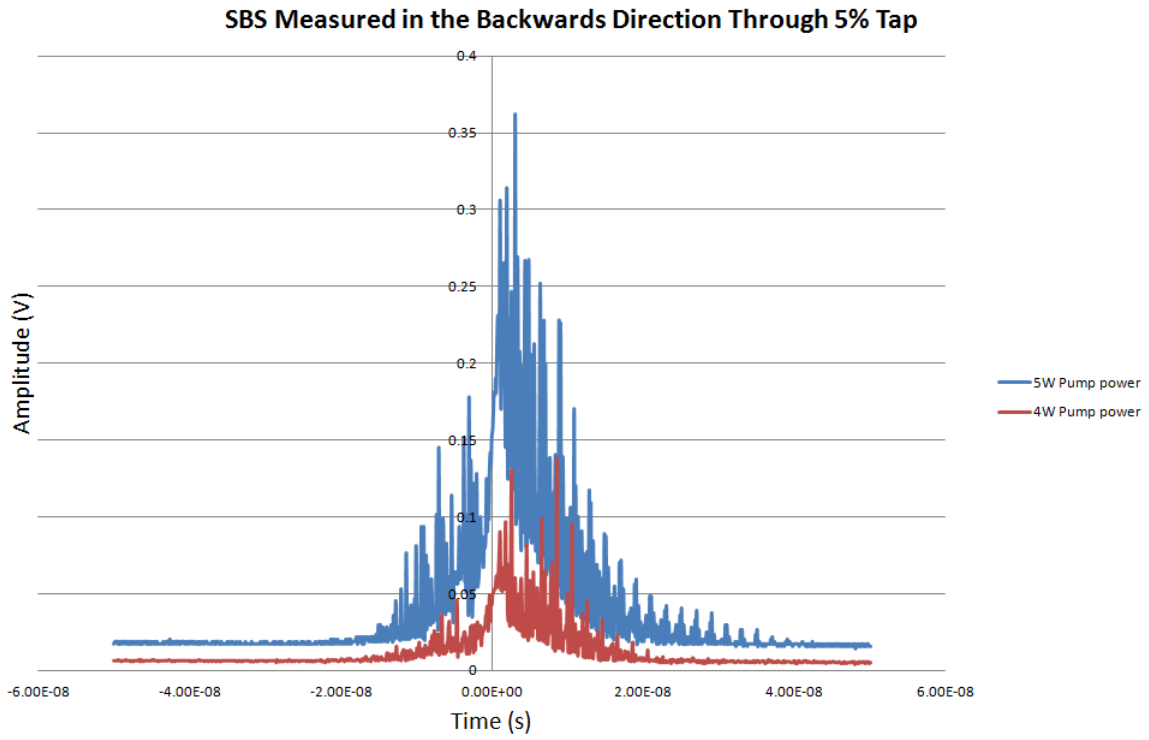

Figure 59: SBS measured in the backwards direction through 5% tap port at two different pump powers

Once again, the pulse shape was measured through the backwards tap to detect any signatures of SBS. Figure 59 shows that at 5W pump power, there are substantial amounts of SBS. This operating condition corresponded to an output power of 1.5W, and approximately 1.5kW peak power. However, when pumped at 4W, the system showed significantly fewer SBS peaks. The output power of the system at 4W pump power reached 1W, approximately 1kW peak power. In order to detect the SBS, the trigger level on the scope was set to twice the average amplitude of the detected pulse. If the oscilloscope triggered multiple times within a short window, of a few seconds, the level of SBS was deemed too high for operation. When the system was pumped with less than 4W there were no signs of SBS, and therefore, for operation within the system, the Amp1 pump should not exceed 4W.

The next and final stage of the fibre MOPA system is a second amplifier stage, a 3m length of Nufern PLMA YDF 25/250 fibre. In order to couple the light from the 10μm core Amp1 stage to the larger core of Amp2, an isolator with a 10/125μm input fibre was used, along with a 25/250μm output fibre. In addition to the isolator, a pump combiner was spliced into the system prior to the amplifier, in order to couple pump light into the fibre, as shown in the figure 53. To ensure the preservation of a good M^2 value, the amplifier stage was wound around an 80mm diameter bobbin, preventing the propagation of higher order modes. As Amp2 is the final output of the fibre MOPA, the fibre was angle cleaved, to prevent back reflections, and mounted in a v-groove onto a translation stage. This allowed for accurate collimation of the output beam using a 13.8mm aspheric lens. Additionally, after the lens, a dichroic mirror was used, that reflected any excess pump (at 975nm) and allowed the signal to pass through. The set-up used can be seen in figure 60

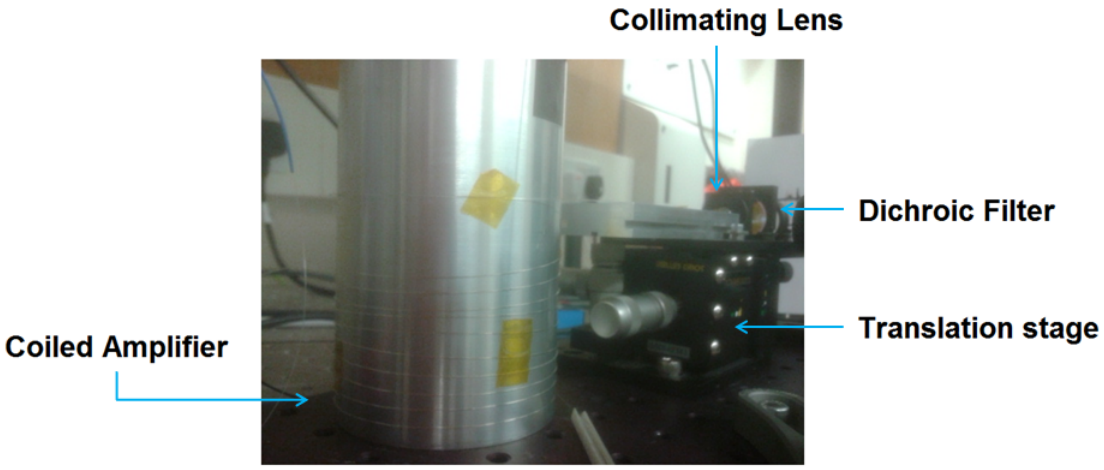

Figure 60: Picture of the Amp2 Set-up, output of the fibre is mounted in a v-groove, and then collimated and passed through a pump reflect dichroic filter

4.2.4 Experimental Results

Initial power measurements were taken using a 30W power meter, directly after the output of Amp2. The pump current was increased up to a maximum value of 4.5A (corresponding to a pump power of 20W). While operating at a repetition rate of 100kHz, and a pulse width of 4ns, the system was able to achieve a maximum output power of 8.05W. The targeted value of 13.4W, using a 10ns pulse, from table 2, can be estimated at a pulse width of 4ns, by reducing the power by the same factor as the reduction in pulse width, giving an approximate target power of 5.36W. Therefore, the system is capable of producing more than the targeted average power.

In addition to the power measurements taken, the spectral data was also collected. To ensure an accurate measurement technique, the set-up shown in figure 61, was used. The benefit of this set-up was that it allowed for both translation stages, holding the fibres, to be bolted parallel to each other, aiding in alignment. The wedge was used to attenuate the signal to a level that was safe entering the OSA.

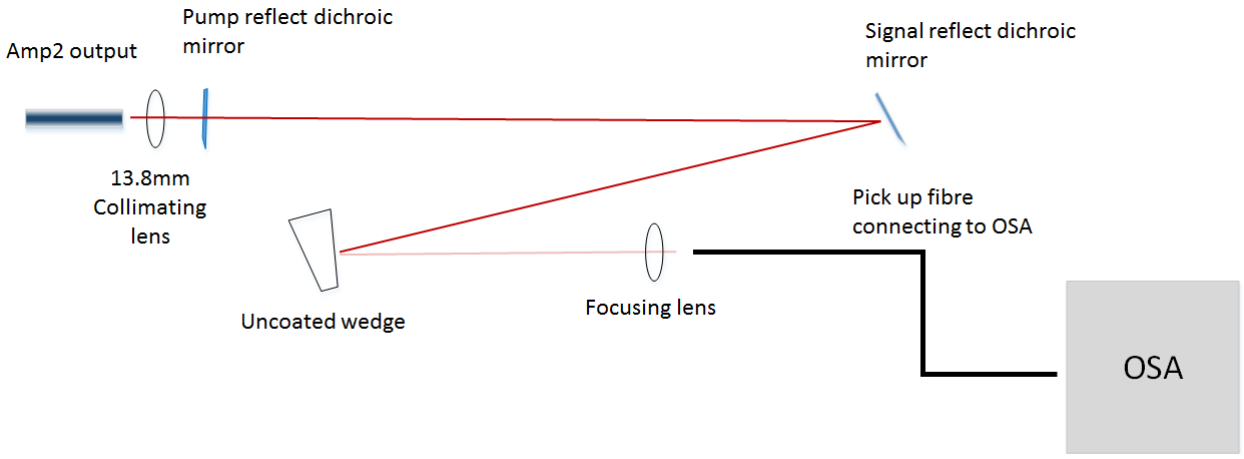

Figure 61: Diagram showing set-up used to take spectral measurements from Amp2. Double reflection used to allow parallel alignment of the translation stages holding the Amp2 output and pick up fibre. An uncoated wedge was used to attenuate the beam

Initial measurements were carried out with a pump power of 1W for Amp1 and up to 20W pump power for Amp2. As shown in figure 62, this resulted in a relatively large spectral width of 0.934nm. At this maximum pump power, we already had more output than targeted, so it was possible to optimise the system to obtain a slightly lower output but at a narrower bandwidth, by reducing both the pump power of Amp1 and Amp2.

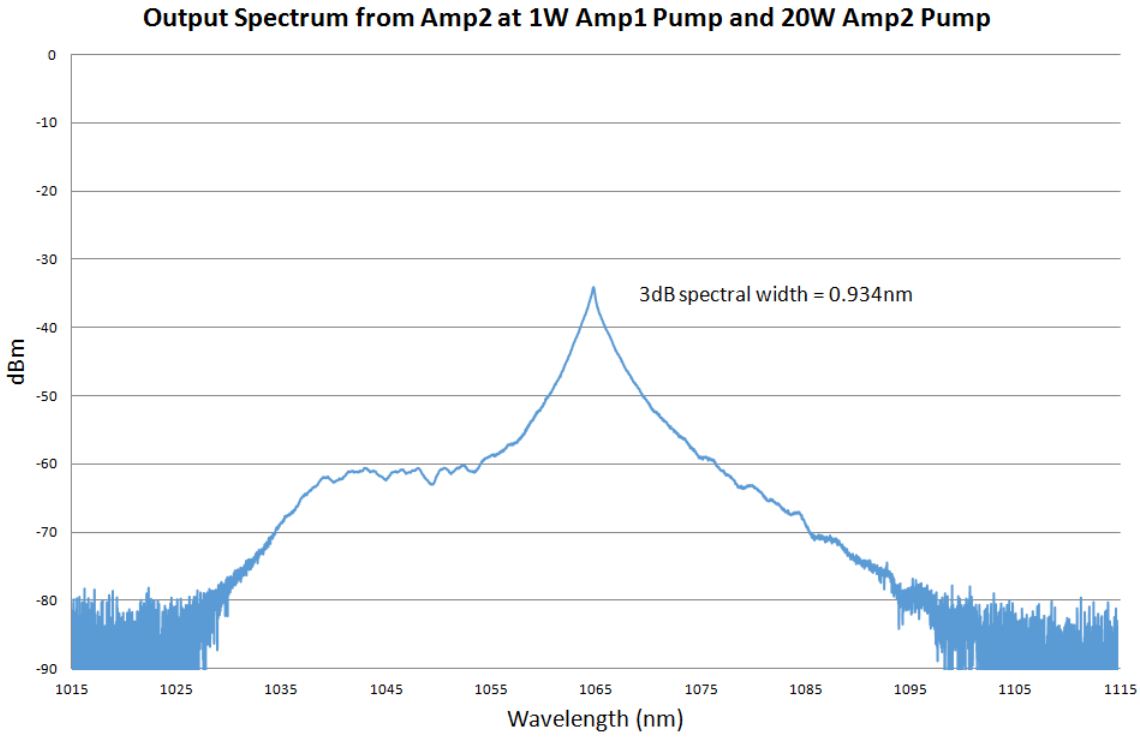

Figure 62: Spectral measurement from Amp2, with 1W pumping of Amp1 and 20W pumping of Amp2

By reducing the pump power to Amp1, it was possible to reduce the input signal power to Amp2. This would result in a larger gain from the fibre, and reduce the propagation length over which high peak power pulses are transmitted, as they would be reached later in the fibre. This has the effect of reducing the broadening effects from self-phase modulation (SPM). The resulting trade-off in doing this is that the ASE will also experience more gain, and thus reduce the output signal to noise ratio (OSNR). By varying the input power, an optimal condition can be reached between the output power, OSNR, and spectral width.

In order to optimise the output of the fibre MOPA system, the pump power of Amp1 was reduced and tested at multiple pump powers for Amp2. Table 3, shows a series of results for various pump powers, and the associated output power, spectral width and OSNR.

Table 3: Optimising output of Amp2 with respect to power, spectral width and OSNR

Amp1 Current (A)	**Amp2 Current (A)**	**Output Power (W)**	**Spectral Width (nm)**	**OSNR (dB)**
1.1	4.3	5.38	0.3458	16.71
1.2	4.0	5.62	0.4726	25.18
1.2	4.2	6.07	0.5045	24.01
1.2	4.3	6.31	0.5217	23.47
1.3	3.5	5.16	0.5114	29.12
1.3	4.0	6.34	0.6298	27.62
1.3	4.3	7.1	0.6779	27.7
1.3	4.5	7.53	0.7538	26.43
1.5	4.3	8.05	0.934	26.63

From the results shown in table 3 it is clear that there is a range of powers and spectral widths that can be achieved for different operating conditions of the system. The most critical value is the spectral width, as the crystal used for second harmonic generation will have a certain acceptance bandwidth, above which the conversion efficiency obtained will be substantially lower. The output power is also an important value, as it is necessary to obtain as high a power as possible to ensure that there is sufficient usable power by the end of the frequency generation section. However, with the ability to adjust over a range of conditions easily, the decision can be made based on initial frequency conversion results.

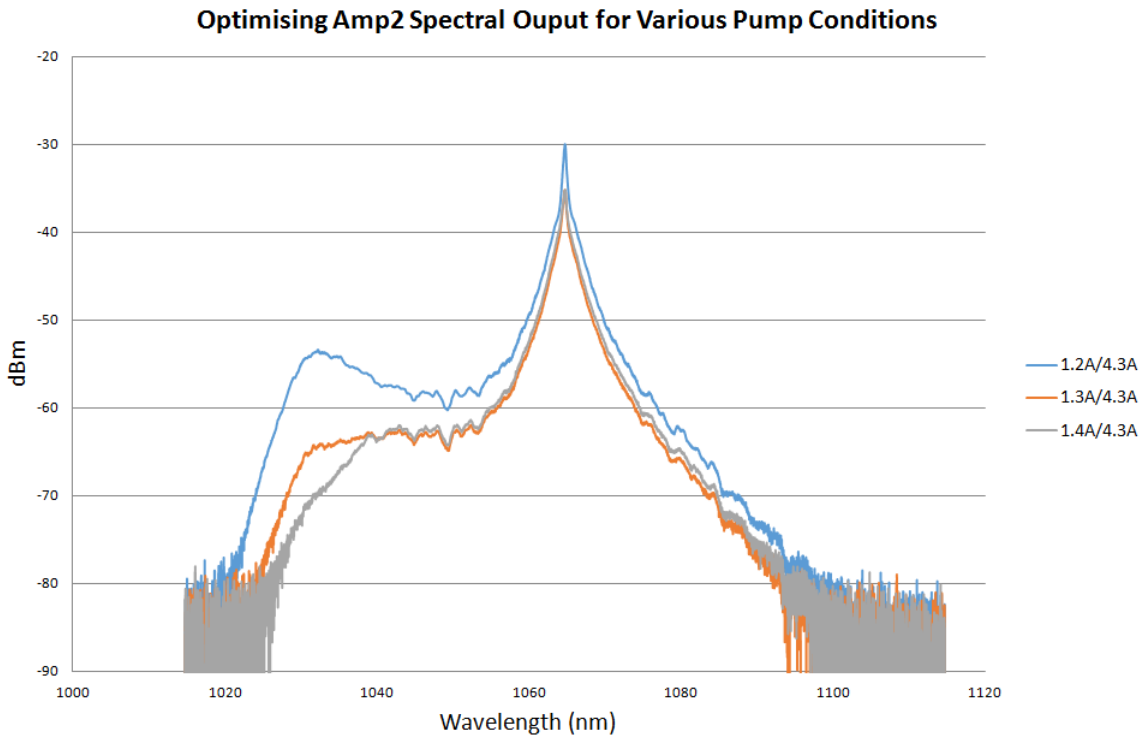

Figure 63: Output spectrum of three different Amp1 pump powers, demonstrating the trade-off between ASE levels and spectral width

Initially, the condition of 1.2A for Amp1, and 4.3A for Amp2 will be chosen as this gives more than the targeted output power initially stated and should be able to produce over 10kW peak power. Additionally, the reduced spectral bandwidth of operating at a lower Amp1 pump power will be beneficial in increasing SHG conversion, discussed in section 5. The trade-off for a narrower bandwidth is an increase in the level of ASE, however at the chosen operating condition, the ASE is still more than 20dB below the signal peak.

With the system able to reach these output conditions it had potential to be a suitable source for SHG. However there were concerns over using an ASE source, and its initial large bandwidth limited the efficiency that could be achieved in SHG. In order to clearly see the benefits and drawbacks of using an ASE source, it was proposed that a second source was configured, and both tested with a SHG set-up to compare the performance.

4.2.5 Conclusions

The first OR-PAM system has serious broadening issues which would result in a significant reduction in second harmonic generation if the bandwidth exceeds the acceptance of the crystal. Therefore to iterate upon the system development, the seed source was swapped from a FP diode locked using a grating, to a FP diode locked using an injected signal from an ASE source. In addition both of the modulators were removed from the system.

The removal of the modulators meant that there was no longer a method to shape or carve the pulses. However short sub 5ns pulses were generated from the FP diode, which relieved some of the concern of SBS. Due to the output pulse energy requirements of the OR-PAM system being significantly lower than that of the PAT system, the pulse shape would not experience such a large amount of distortion and therefore the lack of shaping ability was less of a concern. The system successfully ran at 100kHz up to an average output power of greater than 5W. Optimisation of the pump currents revealed a maximum power of 8W could be reached, however this was at the expense of a larger spectral width. Operating conditions were selected such that over 6W was generated with a bandwidth of 0.52nm.

4.3 Distributed Feedback (DFB) Injection Locking System

4.3.1 Introduction

With the system producing a larger bandwidth signal than was first realised, a different seed approach was considered to reduce the initial bandwidth and thus that of the final output. The solution was to implement a DFB laser to lock the FP diode. This is due to the naturally narrow spectrum produced by a DFB. Having a significantly narrower injection signal will help to ensure the final spectral width will be narrow enough for efficient SHG. The downside of using the DFB injection signal is that the threshold peak power for SBS is proportional to the spectral width. Therefore with a significantly smaller spectral width, the peak power at which SBS sets in will also be significantly lower, reducing the final output energy that can be obtained before the onset of SBS.

4.3.2 DFB Locking Source

To produce a significantly narrower spectral width, the locking signal was changed from an ASE source to a DFB. The DFB has a spectral width of 0.005nm, and therefore will produce a much narrower output from the MOPA system than when injected with the filtered ASE source. Using the DFB will ensure a larger portion of the power will be contained within the acceptance bandwidth of the second harmonic crystal. The DFB provides the benefit on not needing to be filtered and amplified before injection. This is an additional benefit to using the DFB, as it reduces the complexity of the system as well as reducing the number of components required and in turn requiring less space, allowing for a more condensed system. A schematic for the DFB injected system is shown in figure 64. To have the most flexibility in developing the most suitable system, both the ASE and DFB locking signals were spliced to angled physical contact (APC) connectors, such that the system could be swapped easily between the two, for comparison.

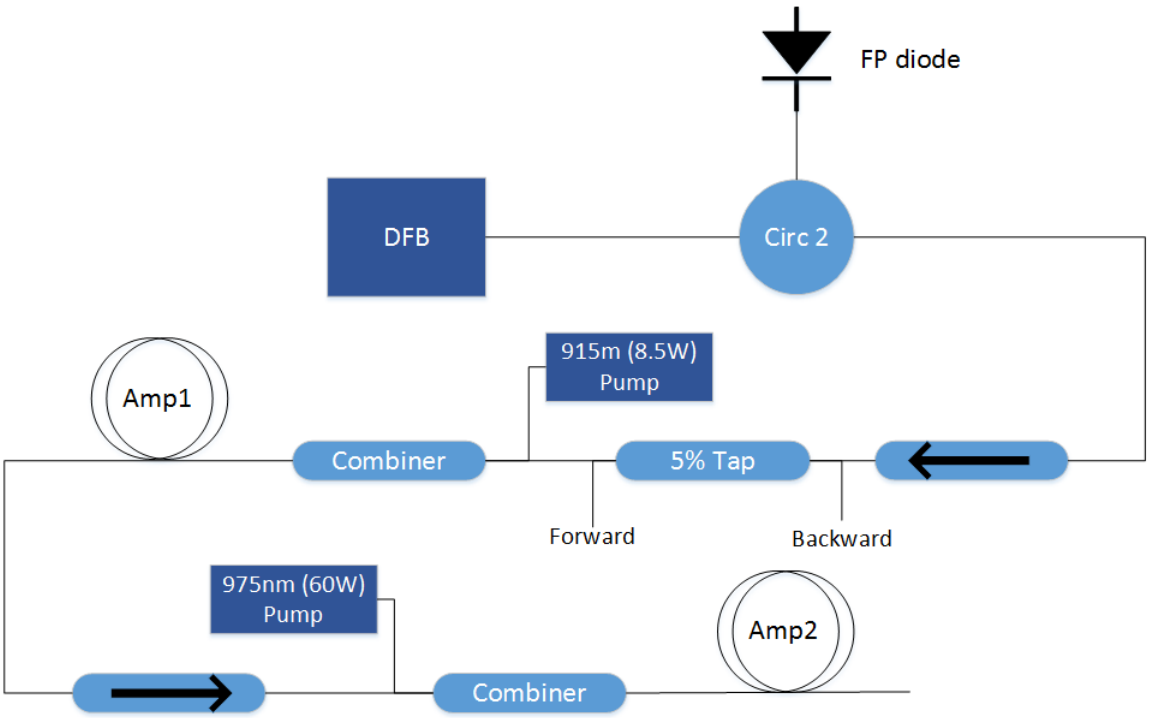

Figure 64: Schematic showing the integration of the DFB laser diode into the fibre MOPA system

Before connecting the DFB signal to the amplifier chain, the source was characterised through a series of measurements, evaluating the output power at increasing current, and measuring the output spectral data. The Drop in power around 74mA is due to the DFB changing modes. A spectral measurement confirmed this, showing the output was being produced at two distinct wavelengths. This can be seen in figures 65 and 66.

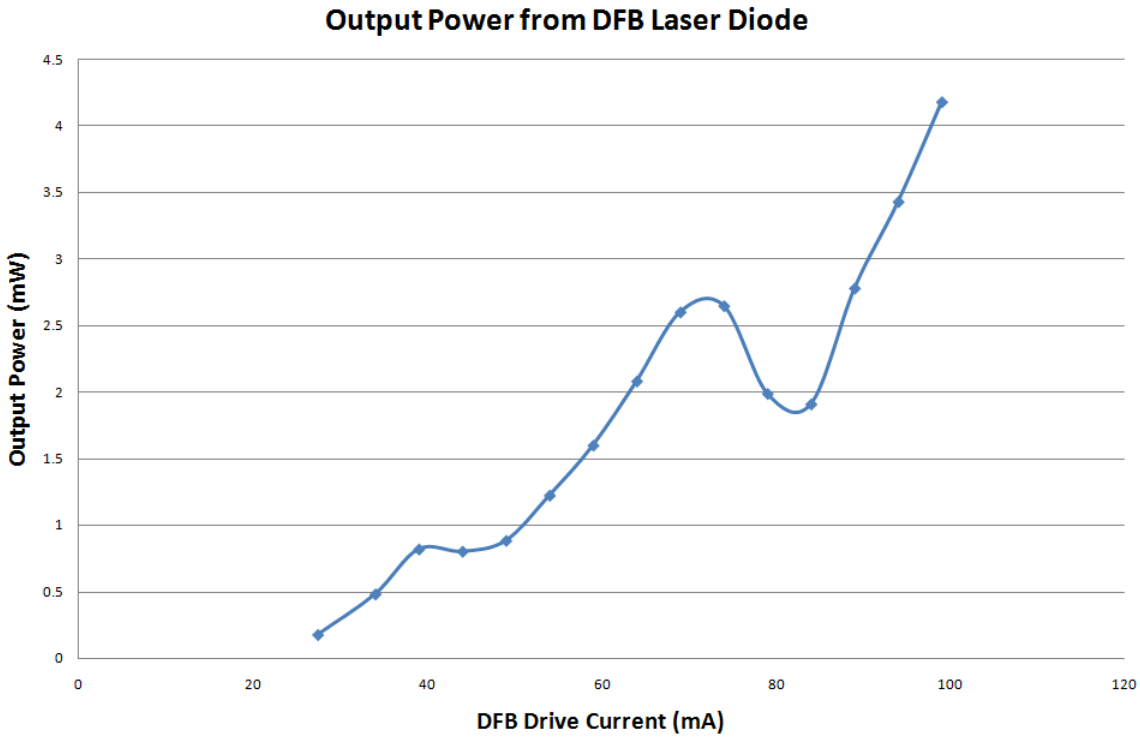

Figure 65: Output power directly from DFB diode

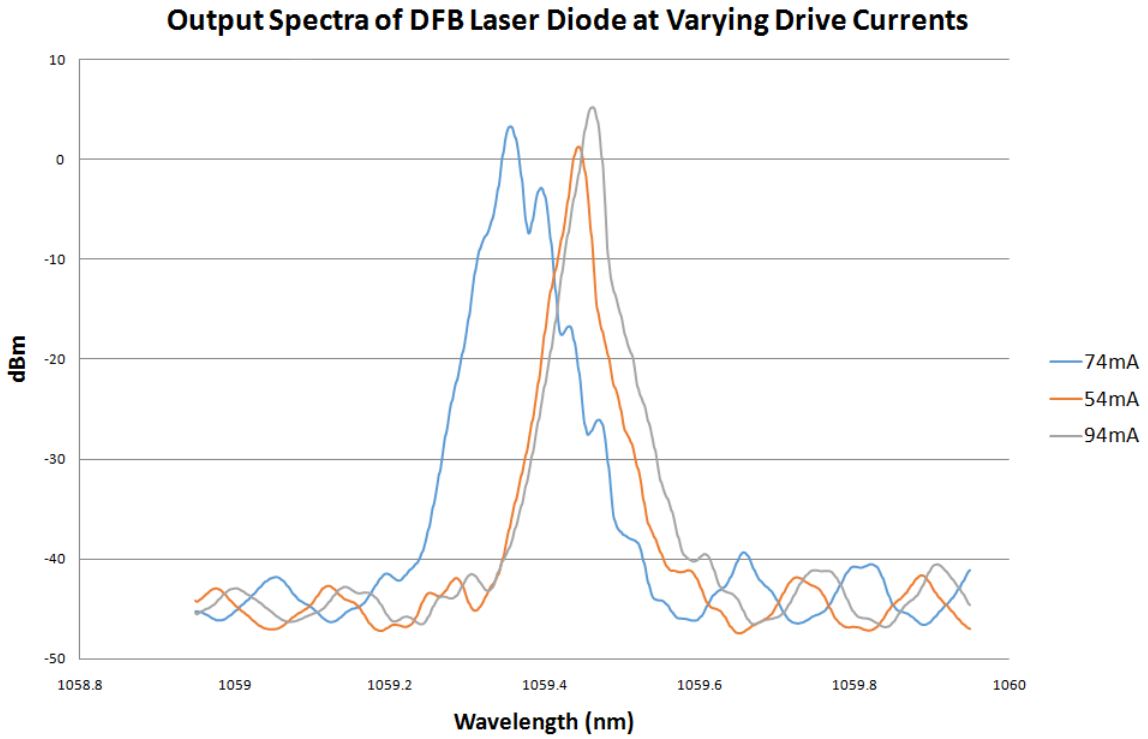

Figure 66: Output Spectra directly from DFB diode at three different drive currents. Output at 74mA shows the DFB transitioning between two modes

From figure 65 and figure 66, it can be seen that, at a drive current of 74mA, the output spectrum of the DFB is no longer a clean narrow spectrum, but instead has several peaks as well as emitting a significantly lower power. This is due to the DFB being between two operational modes. In order to prevent this during operation of the system, the drive current will need to avoid the region of 70-80mA such that the DFB operates at one clean mode and produces a clean and narrow spectrum to be used. With the DFB characterised, it was then connected to the FP diode via a circulator such that the DFB output was injected into the FP. As the remaining sections of the amplifier chain remained the same as when the ASE injection signal was used, output measurements of the DFB and FP seed combination were taken at the forward port of the 5% tap. The drive current to the DFB was increased until the spectrum from the FP diode was locked. This point was identified by the spectrum changing from a broad low intensity peak to a sharp narrow peak, centred at the wavelength produced by the DFB. The locked spectrum can be seen in figure 67, where the DFB was run at a drive current of 85mA, alongside the spectrum with no DFB signal injected into the FP.

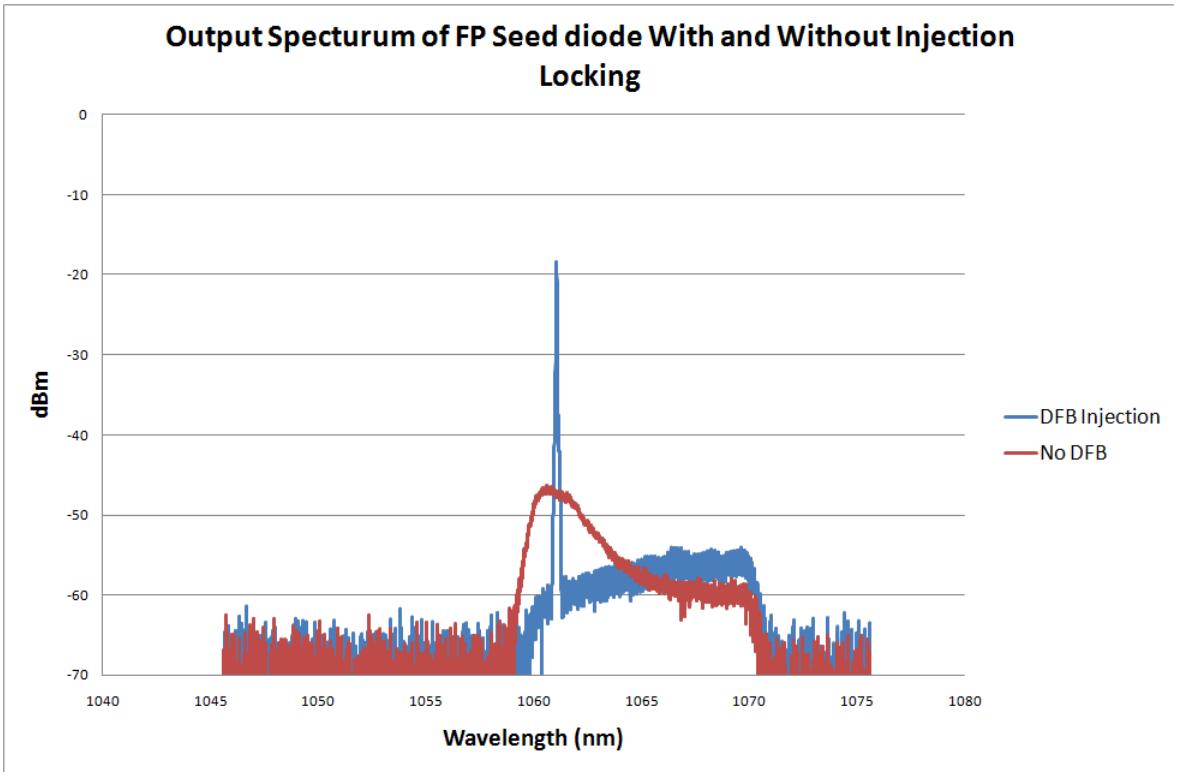

Figure 67: Output Spectra from FP seed diode with and without the injected locking signal from the DFB diode

Initial tests were carried out to determine the length of pulse that could successfully be locked by the DFB injection. This was determined by adjusting the duration of the pulses applied to the FP diode via a pulse generator. A range of pulse widths from 3ns to 50ns were tested at a repetition rate of 500kHz. The pulse shapes were detected from the output of the 5% tap using an indium gallium arsenide (InGaAs) photodetector. The measured pulse shapes are shown in figure 68. From these measured pulse shapes, it was apparent that it was not simple to produce flat topped pulses shorter than 10ns.

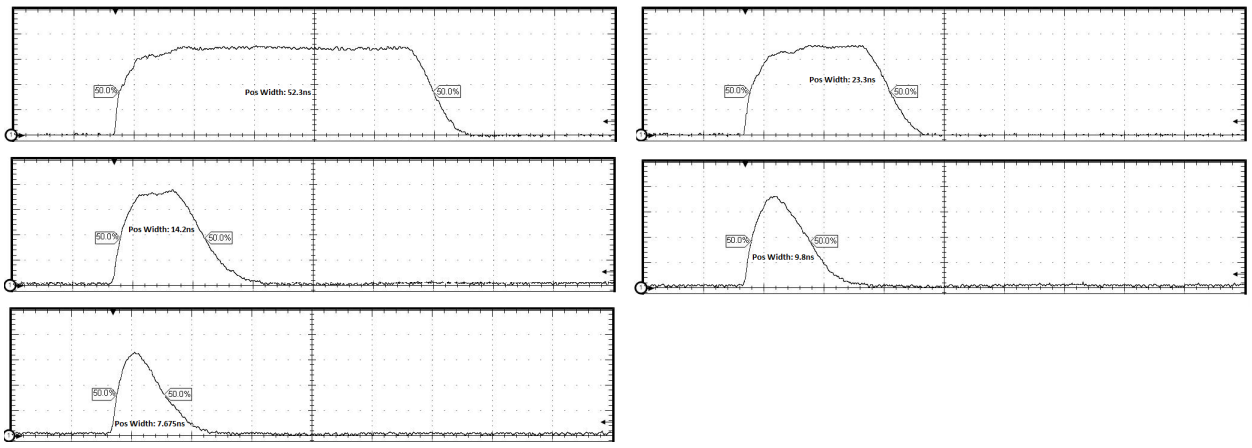

Figure 68: Oscilloscope traces showing generated pulses from locked FP seed diode. The pulse generator duration for each pulse, from top left to bottom right, are 50ns, 20ns, 10ns, 5ns and 3ns.

The custom diode driver being used for the FP should, in theory, be able to generate 1ns pulses, which seemed to suggested that the limitation was the diode packaging, preventing shorter pulses from being able to be generated. This could be due to the packaging having a high capacitance, which would effectively increase the time constant of the diode circuit, thus limiting the shortest pulse width that can be generated. In an attempt to resolve this issue, a new high speed packaged FP diode was tested. Unfortunately, the majority of the injected signal from the DFB was just reflected from the diode and therefore it was not able to lock the diode. This was probably due to a difference in the construction of the diode, resulting in a much higher reflection from the facet of the fibre. However, when swapping between the two FP diodes, it was noted that the injection signal from the DFB was at a significantly different output power for the same drive current. Upon further investigation, it became apparent that the pigtail from the DFB was non-PM, as opposed to the rest of the system which was PM. This meant that there could be fluctuations in the injected power to the FP seed diode. To correct this, a polarisation controller was placed on the pigtail of the DFB and optimised, such that the maximum power was transmitted. With the addition of the polarisation controller, it became slightly easier to lock shorter pulses through the tuning of the amplifier and bias settings on the FP driver board. It was now possible to lock a 3.4ns pulse with a relatively smooth shape, as shown in figure 69.

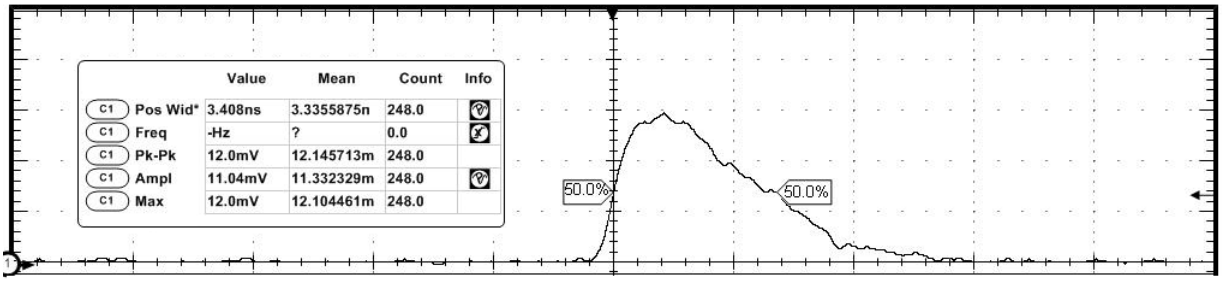

Figure 69: Optimised locked 3.4ns pulse achieved after the addition of a polarisation controller on the pigtail of the DFB

4.3.3 Experimental Results

With the DFB seed set-up successfully locking a 3.4ns pulse, the next stage was to pass this signal through the pumped amplifier chain, in order to observe the output power and spectrum produced. As the amplifier chain was still in one complete system from the ASE injection locked set-up, some initial tests could be quickly run to asses any major issues. Power measurements taken at the output of the fibre system indicated that the average power reached approximately 5W. This value suggested the system was working as intended, given that with the ASE injection set-up, a similar power of 5.62W, seen in table 3 was measured at slightly higher operating currents. However, upon inspection of the spectral data, the new DFB injected system had an output signal to noise ratio (OSNR) of approximately 10dB. This suggested that at some point in the system there was too little seed power entering an amplifier. As the amplifier chain was already constructed and spliced together, there was no direct way to measure the power entering the two amplifiers. However, using data taken from the forward 5% tap, it was possible to calculate the input to Amp1 by using the tap ratio of 15.5 calculated from previous measurement. By increasing the seed power entering the amplifier, the OSNR of the final amplifier should be reduced. To achieve this, Amp0, as shown in figure 33 was returned to the system. This pre-amplifier, with the option of both co and counter pumping, would provide a variable amount of amplification within the system to help increase the seed power to a suitable value, before entering the first amplifier.

To help keep the pulse broadening to a minimum throughout the system, Amp0 was initially only pumped backwards. The main purpose of adding Amp0 back into the system was to produce enough power to seed Amp1. Therefore, when deciding upon an operating pump current, the primary concern was producing enough power. However, only just enough power should be generated, as any excess gain will increase the broadening within the system, as well as increasing the ASE build-up within the amplifier, reducing the OSNR. Figure 70 shows the effect on the spectrum that increasing the pump current to Amp0 has, while table 4 shows the effect this has on the output power

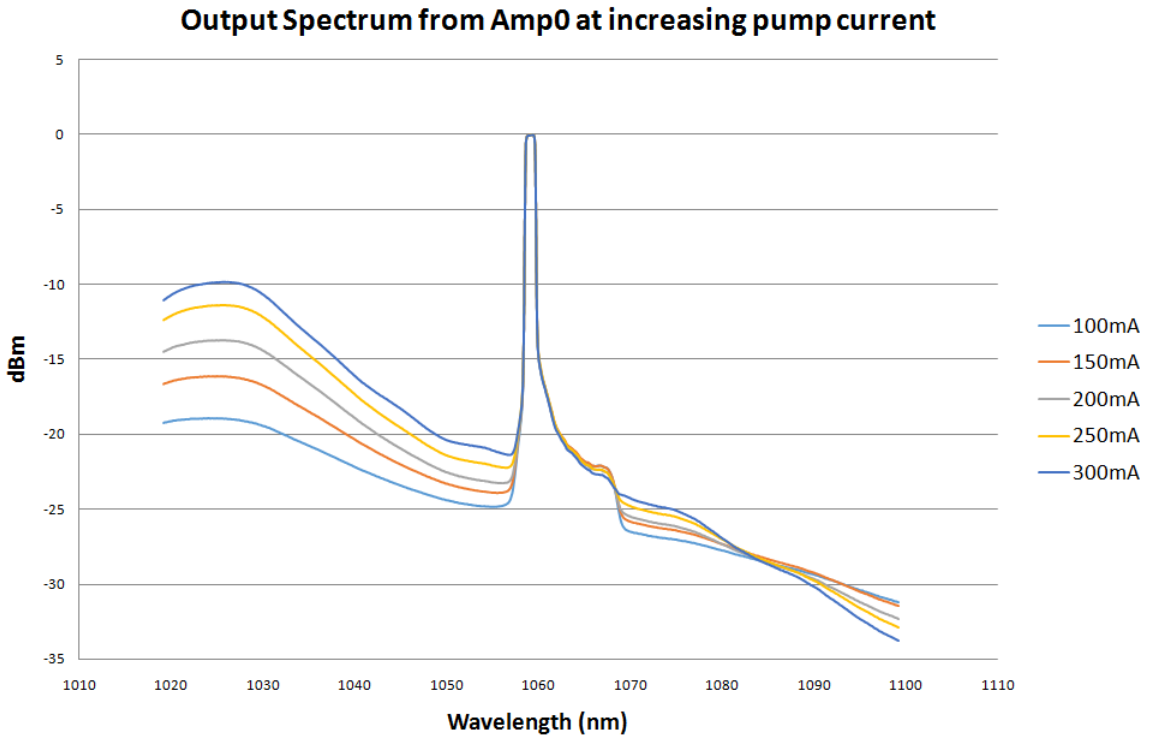

Figure 70: Normalised spectral output showing the increased ASE level as the amplifier pump current is increased

Table 4: Optimising output of Amp2 with respect to power, spectral width and OSNR

Amp0 Current (mA)	**Measured Output of Amp0 (mW)**	**Output Power at Tap (μW)**	**Calculated Power Entering Amp1 (mW)**
100	0.302	7.05	0.109
150	0.699	17.46	0.271
200	1.851	42.40	0.657
250	3.691	97.22	1.51
300	-	211.60	3.28

Table 4 shows the measured output power from Amp0 for an increase in the pump current, as well as the measured value for the power at the forward port of the 5% tap. The estimated power entering Amp1 was calculated using the known tap ratio. At a pump current of 300mA the output from Amp0 was unstable, and therefore a reliable reading could not be taken. This may have been due to the fibre being flat cleaved in preparation for splicing, resulting in a larger reflection from the fibre facet. To sufficiently seed Amp1 an input of 1mW was targeted as 0.25mW was sufficient when locking 10ns pulses using the ASE locking source. Therefore the current was set to 250mA for Amp0, providing slightly more than enough, allowing for tuning down if necessary.

With a suitable power seeding Amp1, the next available position to measure the signal was at the output of Amp2. Amp1 was set to run at the same condition as used with the ASE injection source, given the same amplifier configuration as well as the matched input to Amp1. With the output of Amp1 being used to seed the final amplifier stage, the final pump can be turned on and increased, while both the output power and spectral data are collected.

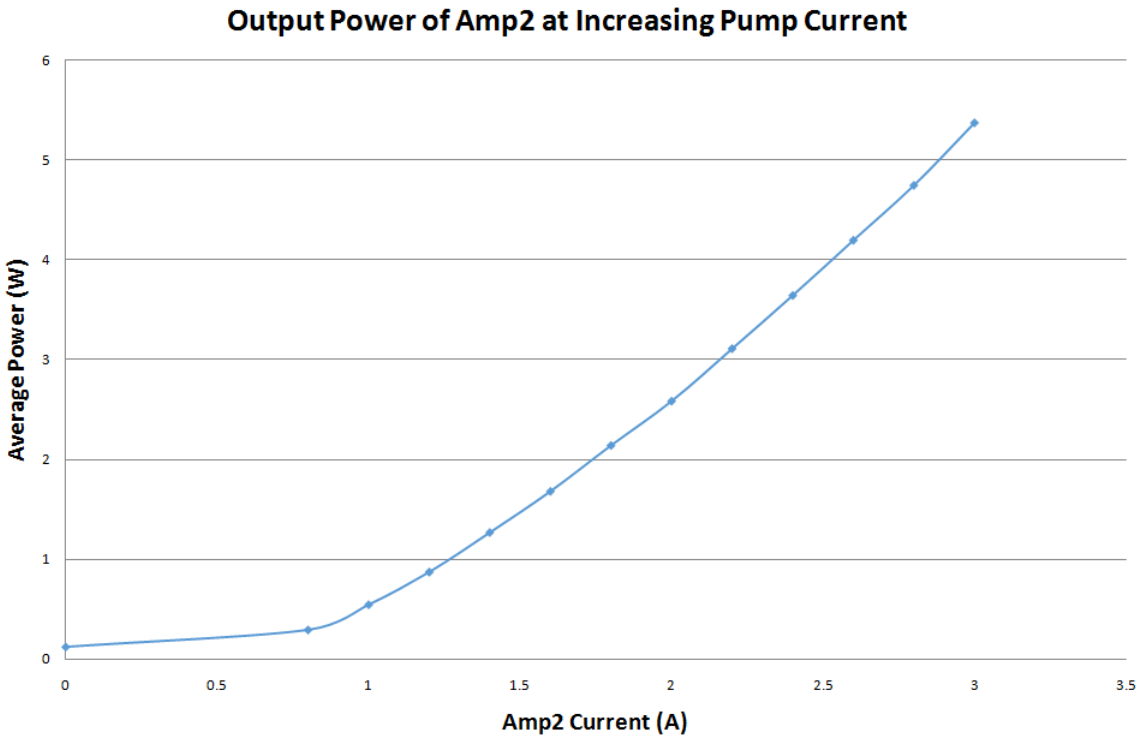

Figure 71: Output power of Amp2 as a function of applied pump current

Figure 71 shows that the output of Amp2 produces similar average power to that when the ASE source was used. However, given that the pulse is now shorter, the peak power will be increased in the case of the DFB system. Additionally, the DFB system produces a significantly narrower output spectrum, as show in figure 72, where the 3dB spectral width is below 0.04nm at 3A pump current.

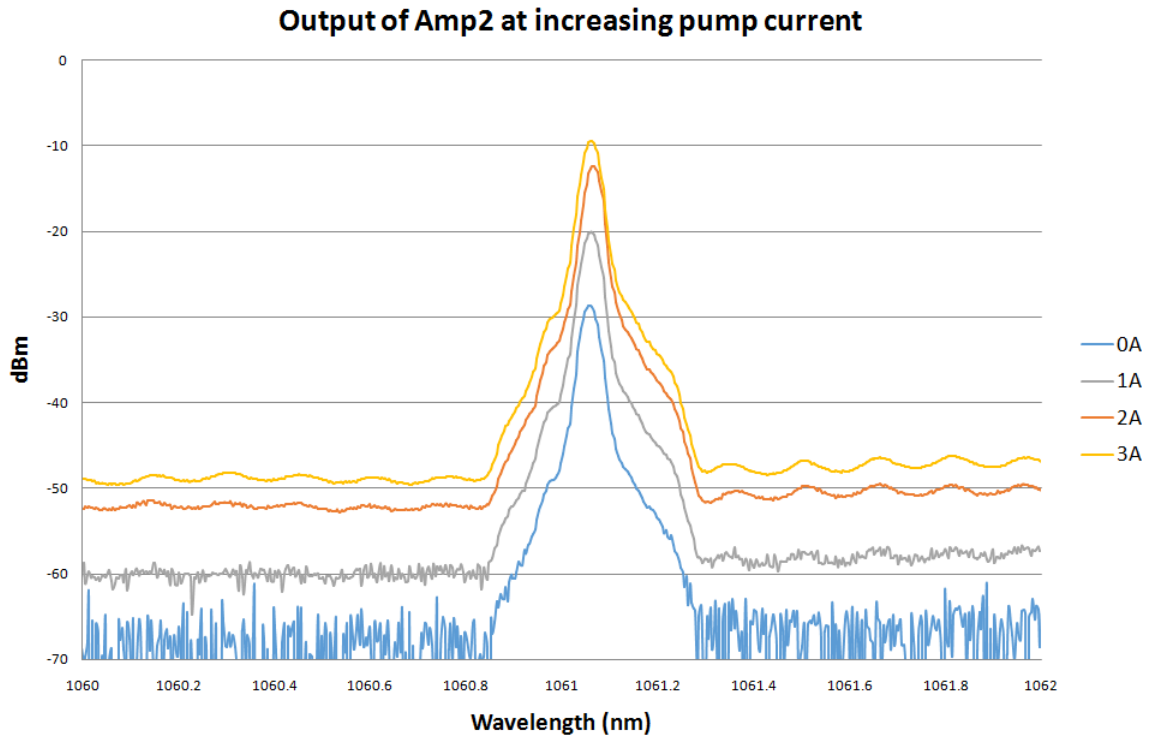

Figure 72: Output spectra of Amp2 at increasing pump current

To further improve the system, it was proposed to swap the final amplifier pumping scheme from co-pumping to counter-pumping. This would help to reduce the average peak power transmitted along the length of the final amplifier, due to the pump intensity being greatest at the end of the fibre. This should allow a higher peak power to be generated in the final stage without running into detrimental non-linear effects.To change the pumping scheme of the final amplifier, only a slight modification to the system was required. The pump combiner between the isolator and Amp2 needed to be removed, and a free space pump set-up needs to be implemented at the output of the system. In order to counter-pump the final amplifier, a simple set-up using a dichroic mirror can be implemented. The pump diode output fibre is prepared and placed on a translation stage, directed towards the end facet of Amp2. An 8mm focal length lens is used to collimate the pump output. This lens was chosen to match that used to collimate signal output, so that the pump would be focused into the final amplifier. A dichroic mirror with Thorlabs coating #3 is placed between the pump fibre and the amplifier fibre, in order to reflect the output signal from the system, while simultaneously allowing the pump signal to pass through the mirror and enter the amplifier. A schematic of the new counter-pumped amplifier can be seen in figure 73.

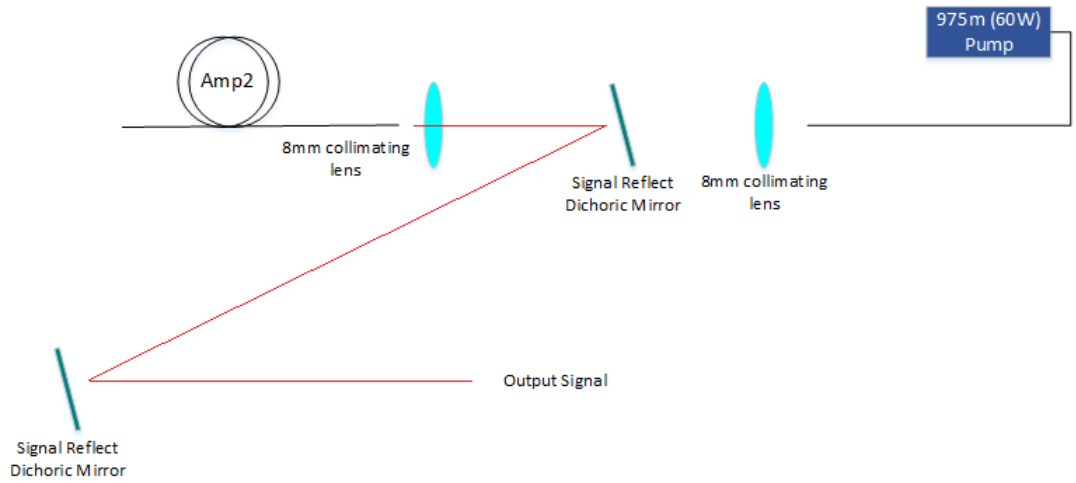

Figure 73: Schematic diagram showing the counter-pumped configuration used for Amp2

In the process of removing the pump combiner from the system, there was now a direct point to re-measure the input power to the final amplifier, at the output of the 10μm-25μm isolator. Having a clear idea of the input to the final amplifier helps to identify any irregular or unwanted features generated in the final amplifier, as well as being able to accurately calculate values such as the gain. The output measurements, shown in figure 74, depict the relatively clean and narrow spectrum, with a 3dB spectral width no more than 0.04nm and an OSNR of 24dB, was the output of the 10μm-25μm isolator. The power was increased up to an output just below 300mW. Although this is significantly lower than the output of the ASE injection system, due to the much shorter pulse width the peak powers in each case are comparable.

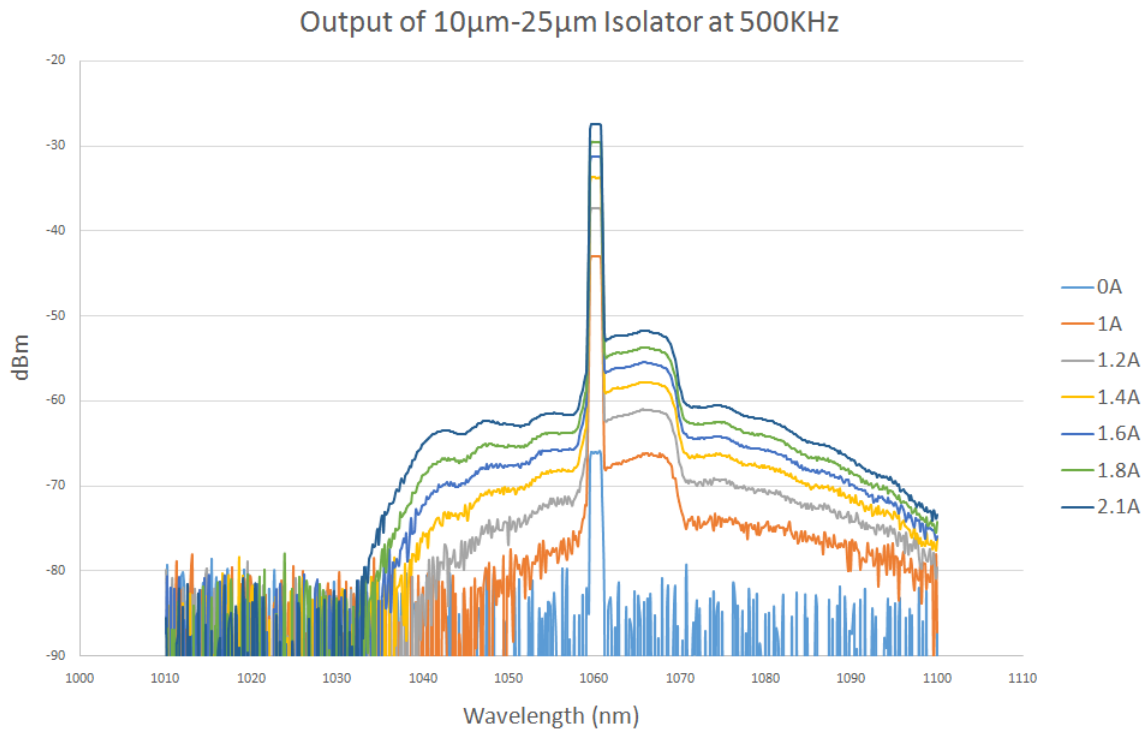

Figure 74: Output of 10-25um iso

With the characteristics of the pulse measured at the input to the final amplifier, the system was once again set-up, as shown in figure 73. The whole system could now be tested and compared with the results from when the ASE source was used. Table 5 shows the output power, spectral width and OSNR measured at the output of Amp2. The spectral width was measured at a resolution of 0.02nm while the OSNR was measured at a resolution of 1nm.

Table 5: Output characteristics from the final amplifier, running at a constant amp1 current of 1.2A

Amp2 Current (A)	**Output Power (W)**	**Spectral Width (nm)**	**OSNR (dB)**
1.0	0.844	0.0336	21.99
1.5	2.116	0.0354	22.44
2.0	3.58	0.0332	21.93
2.5	5.13	0.0352	22.16
3.0	6.73	0.0328	22.30
3.5	8.35	0.031	22.24
4.1	10.26	0.0319	22.15

Comparing the final outputs to those in table 3 it is apparent that the system is now capable of producing a significantly higher power, from a maximum of 8.05W up to 10.26W at comparable pump currents. Additionally the use of the DFB has greatly reduced the spectral width at high pump currents, from a maximum of 0.934nm when using the ASE to 0.0354 with the DFB. This difference in spectral width will ensure that a larger portion of the available power will be within the required bandwidth for efficient conversion. Despite these improvements, the OSNR of the system has dropped by up to 7dB. This indicates that there is a higher level of background unwanted power, which is in turn reducing the useful power that can be converted.

To determine the impact of the reduced OSNR, the power over the entire spectrum was integrated, and the power contained within the 3dB peak was compared to that calculated over the rest of the spectrum. This comparison indicated that the peak contained less than 40 % of the total power. With such a low portion of the power contained within the pulse peak, it was suggested that there may be some background CW light contributing a large portion of the power. To confirm this suspicion the output of the seed pulse was investigated at the output of the forward 5% tap. By switching the seed diode on and off while measuring the output spectrum it was apparent that not only was the pulse appearing, but the base level was also increasing. This base level can be attributed to CW light that is present at all times as opposed to the pulse window. By reducing the bias setting on the FP diode driver we were able to remove the CW light present. However this had a strong effect on the pulse shape, as well as reducing the output power. With no bias present, the best suited pulse shape that could be produced was a 1.4ns pulse made up of two distinct peaks, as shown in figure 75

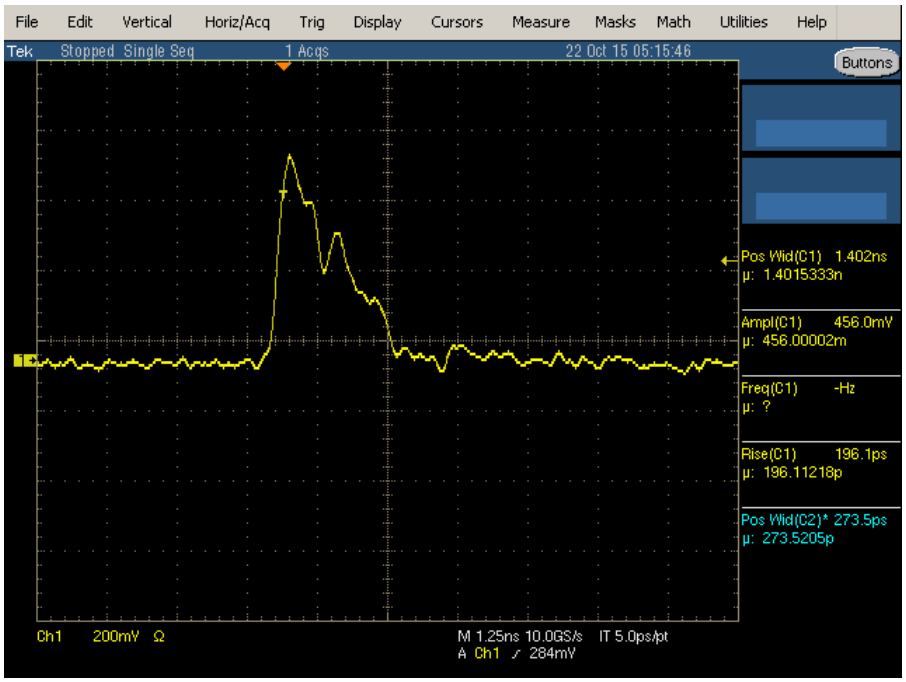

Figure 75: Optimised pulse shape while ensuring no CW light is present

Despite this pulse being less than ideal, after discussing the shape with our collaborators at UCL, it was decided that as long as the pulse shape remained a duration of a few nanoseconds, while reaching at least 1μJ of output energy when frequency doubled to 530nm, then it would still be able to be used to demonstrate an optical resolution photoacoustic microscopy system.

With the CW power removed from the pulse, the power entering the pre-amplifier was now lower, and thus to compensate the pump current was increased to 246mA. With these changes the signal was once again measured at the forward tap as well as at the output of the system with just Amp1 as well as both amplifiers running, the pulse shape and spectral data can be seen in figure 76, where all of the tests were conducted at a repetition rate of 500kHz.

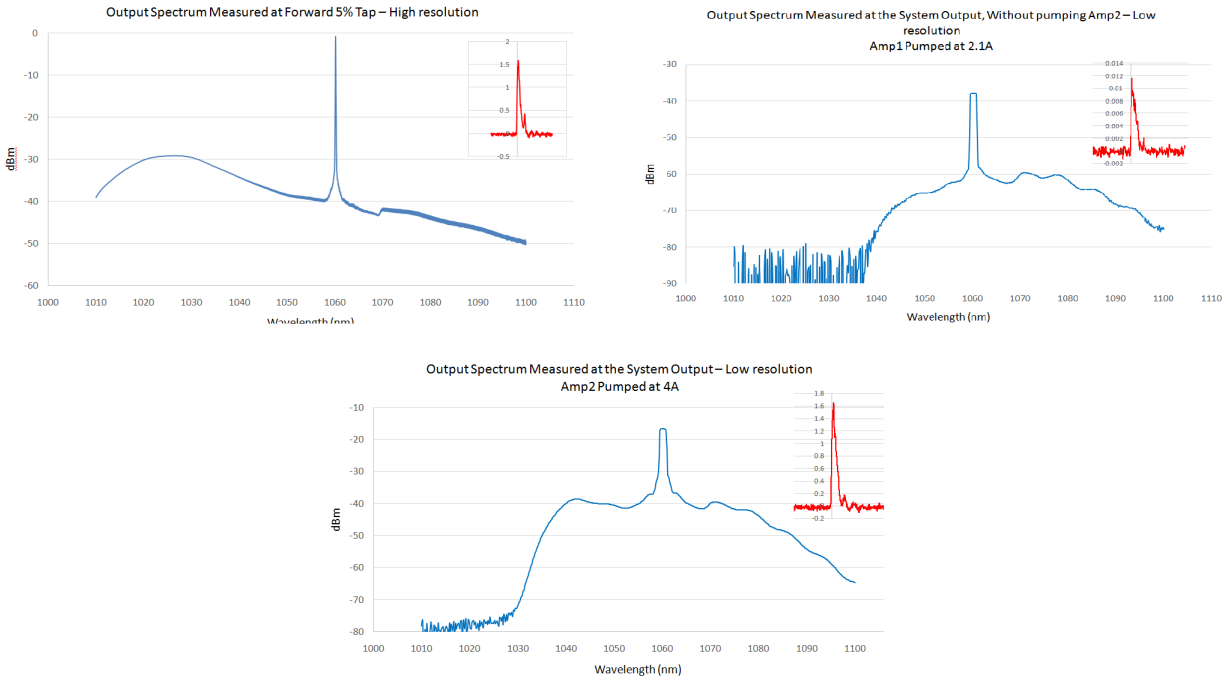

Figure 76: Output spectral measurement and pulse shape as the pulse propagated through the system

The changes to the system only resulted in a slight drop in power, reducing the output power at 4.1A to 9.93W. However, with the removal of the CW power, all of the measured average output power will be contained within the pulse.

4.3.4 Conclusions

Due to limitations with the pulse and spectral widths when locking with an ASE source, a second source was designed and tested using a DFB diode. The immediate advantage of using the DFB was the significantly narrower natural linewidth. Therefore the locking source was significantly simplified as well as reduced in physical size. Two different FP diodes were tested in an attempt to generate a 1-2ns pulses. Unfortunately one FP diode reflected the majority of the injected signal and therefore was not suitable for our use. Tests using the DFB system were able to reach average output powers of over 10W while running at 500kHz, while also maintaining a spectral width of less than 0.36nm.

5 Second Harmonic Generation

5.1 Introduction

The successful generation of the second harmonic relies on non-linearities within certain crystal as described in section 2.3. The advantage of this process is that it provides access to wavelengths that are non-trivial to produce as the fundamental of a laser system. Due to the varying levels of susceptibility of different materials, certain crystals are more attractive for desired non-linear interactions. For example lithium triborate (LBO) is a common crystal for SHG in Nd:YAG lasers.

When choosing a crystal for SHG there are several factors that must be considered, such as the dimensions of the crystal, the maximum power threshold, the spatial walk off and the operating wavelength. For SHG from a 1064nm fundamental source, there are three commonly used crystals, LBO, barium borate (BBO) and potassium titanyl phosphate (KTP). There main benefits being that BBO offers the highest conversion efficiency, KTP is the most cost-efficient and LBO can achieve non-critical phase matching at 1064nm. LBO was the chosen crystal for this experiment for a number of reasons. Firstly it has a high damage threshold, of 10GW/cm^2[51], as opposed to 100MW/cm^2[52] of lithium niobate, another common frequency doubling crystal. A high damage threshold is important due to the need to focus the beam into the crystal to reach required intensities for efficient conversion. Secondly, the crystal can be manufactured to behave in one of several phase matching types. These different types affect the polarisation of the generated beam depending upon the input. This is desirable, as it allows the second harmonic to be generated at a perpendicular polarisation from the fundamental when a type 1 crystal is used. This is beneficial, as it allows a type 2 crystal to be easily used for SFG, which requires two inputs at perpendicular linear polarisations. Finally it is possible to operate LBO in a non-critical phase matching (NCPM) regime. This is achieved by tuning the temperature of the LBO crystal, such that the refractive indices experience by the fundamental and second harmonic waves is identical, leading to a perfect phase matching condition. NCPM is advantageous as, due to the phase matching condition being achieved by temperature tuning, the SHG process is relatively insensitive to misalignments, as well as avoiding the effect of spatial walk-off, aiding in reaching the maximum efficiency possible.

5.2 Phase Matching

When attempting to obtain a high conversion efficiency from the fundamental to the second harmonic, it is important to look at the phase matching condition. Equation 42 describes the phase matching condition for type one, second harmonic generation, where k_1 represents the wavenumber of the incident light, and k_2 is the wavenumber of the second harmonic light.

$$\Delta k = 2k_1 - k_2 \tag{42}$$

By phase matching the process, $\Delta k = 0$, it is ensured that all of the second harmonic contributions along the crystal length add up constructively. With no phase matching maintained, the generated second harmonic waves may destructively interfere with each other, which, in the worst case, can result in no output power at the end of the crystal.

The phasor diagram, shown in figure 16 (section 2.3.1), shows that, without phase matching, the periodic shift in the phase leads to only a small generated second harmonic power that oscillates over the length of the crystal. Conversely, when the phase matching condition is met, each component adds up constructively, resulting in an increasing power over the length of the crystal. A phase miss-match has a strong negative effect on the conversion efficiency obtained for the SHG process. This effect can be described by the phase mismatch factor[19], $sinc^2(\frac{\Delta kL}{2})$, which has been plotted in figure 17. Figure 17 clearly shows that a small increase in Δk will result in a significant decrease in the value of the phase mismatch factor which directly affects the efficiency obtainable.

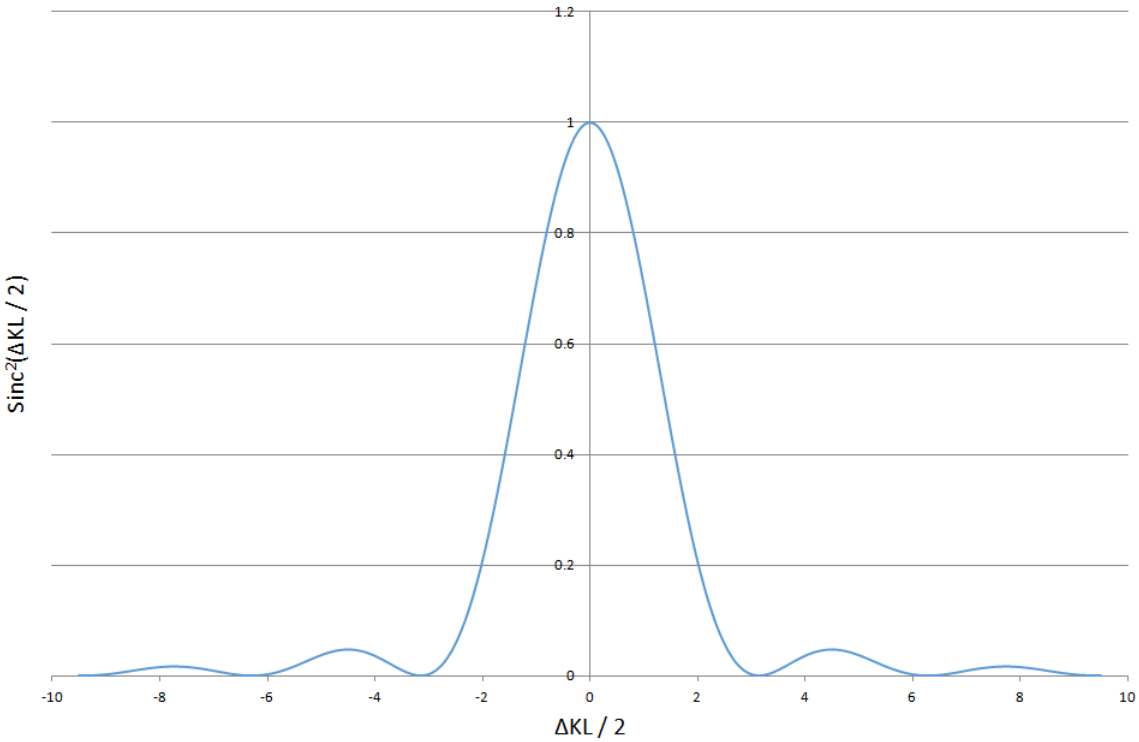

Figure 77: Plot of the phase mismatch factor, indicating the importance of phase matching to reach high conversion efficiencies

In order to understand the phase matching relation for LBO, the wavelength dependant refractive index was calculated, by using the Sellmeier equations[46], shown in equation 43-45, in order to determine where a perfect phase matching condition could be achieved.

$$n_x^2 = 2.4542 + \frac{0.01125}{\lambda^2 - 0.01135} - 0.01388\lambda^2 \tag{43}$$

$$n_y^2 = 2.5391 + \frac{0.01277}{\lambda^2 - 0.01189} - 0.01849\lambda^2 + 4.3025\text{x}10^{-5}\lambda^4 - 2.9131\text{x}10^{-5}\lambda^6 \tag{44}$$

$$n_z^2 = 2.5865 + \frac{0.01277}{\lambda^2 - 0.01189} - 0.01862\lambda^2 + 4.5778\text{x}10^{-5}\lambda^4 - 3.2526\text{x}10^{-5}\lambda^6 \tag{45}$$

Using the listed Sellmeier equations, the refractive index could be calculated at any given wavelength. By comparing the k values calculated from the wavelength dependant refractive index, it was possible to determine the phase matching wavelength at $20°C$. From figure 78 it can be seen that the phase matching condition is satisfied, when the fundamental wavelength is at 1.213μm.

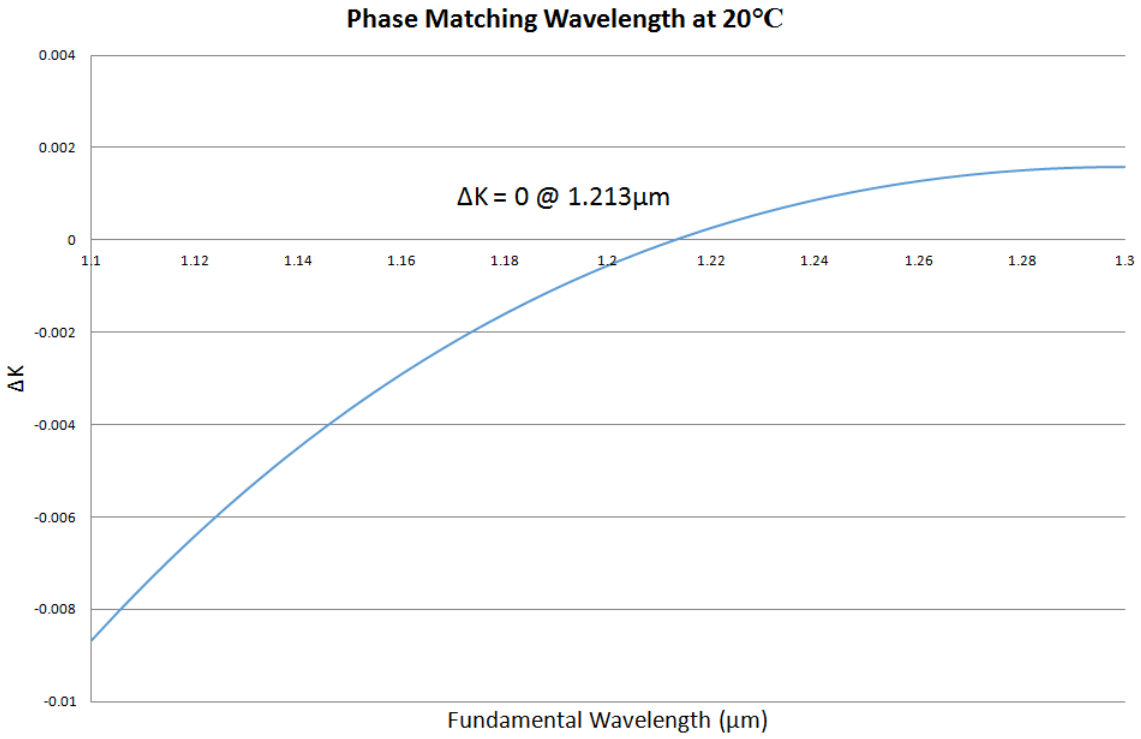

Figure 78: Plot of Δk at various fundamental wavelengths, showing that a perfect phase matching condition can be obtained for an incident wavelength of 1.213μm

Although this proves that perfect phase matching is achievable in LBO, the required wavelength is significantly higher than the operational wavelength of the MOPA2 system, 1.064μm. To shift the phase matching condition to a different wavelength, the crystal can either be angle or temperature tuned. This varies the refractive index that the two waves experience. Due to LBO's temperature tuning ability as mentioned earlier, it is possible to achieve phase matching at 1.064μm just using temperature tuning. The temperature dependant refractive index corrections, given in equation 46-48[54], can be used to determine the refractive indices at various temperatures. Using these equations, it was possible to determine that at a temperature of 200.5°C phase matching could be achieved for SHG at 1.064μm

$$\frac{dn_x}{dT} = -9.3\text{x}10^{-6} \tag{46}$$

$$\frac{dn_y}{dT} = -13.6\text{x}10^{-6} \tag{47}$$

$$\frac{dn_z}{dT} = -6.3\text{x}10^{-6} - 2.1\text{x}10^{-6}\lambda \tag{48}$$

Where λ is given in μm

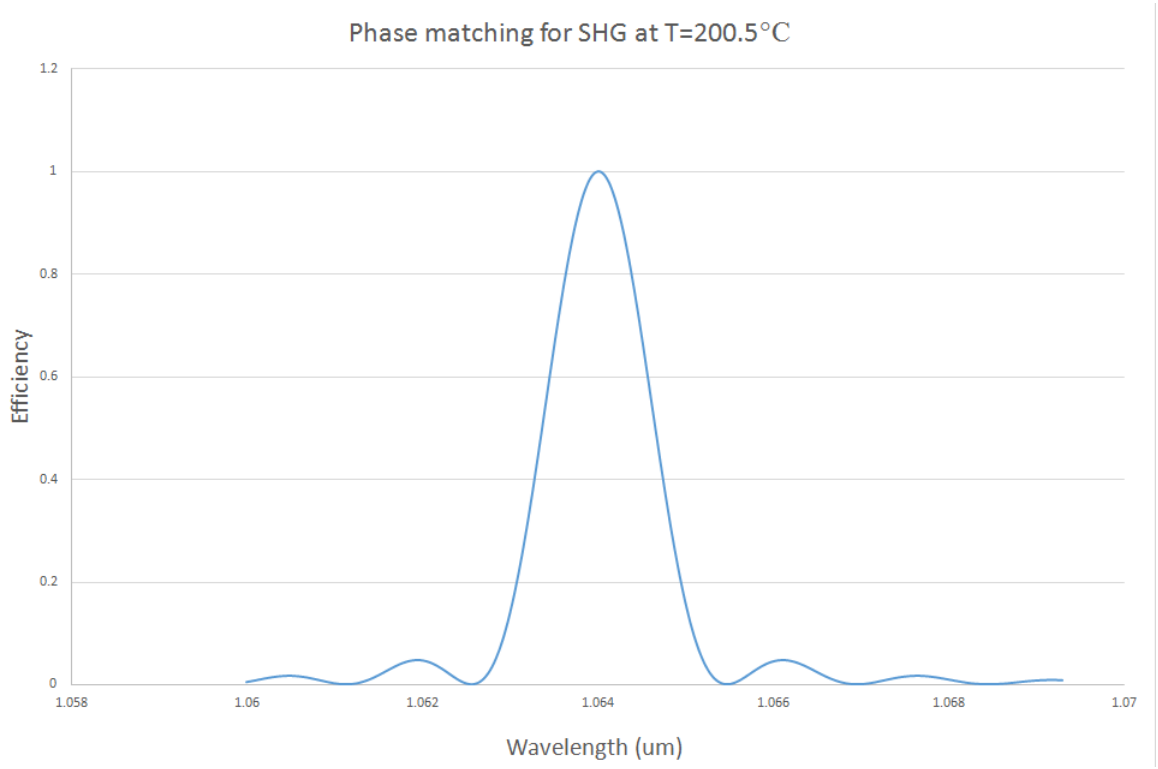

Figure 79: Plot of the phase mismatch function where the crystal has been heated to 200.5°C resulting in phase matching being achieved at 1.064μm

Using these expressions, in conjunction with the Sellmeier equations, it is possible to create a phase matching plot at 1.064μm. From figure 79 it can be seen that at a temperature of 200.5°C a perfect phase matching condition can be achieved. This figure can also be used to determine a suitable bandwidth to be used with the LBO crystal, as we want the pump signal to be no larger than the full width half maximum (FWHM) of the phase matching peak, measured to be 1.16nm. By ensuring that the input signal to the crystal does not exceed this bandwidth, then all of the signal can experience significant conversion, due to satisfying the phase matching condition. For comparison, the spectral bandwidth of a 15mm LBO crystal was measured to be $\sim 1nm$[47], 0.7nm[48] and 2nm[49]. This suggests that the calculated bandwidth here may be a slight overestimation, as for a longer crystal, the bandwidth will decrease. However, [49] measured a significantly larger bandwidth, which agrees with test results more closely. The discrepancies between values may be due to the temperature at which the LBO crystal was operated, as in [47] the crystal is maintained at a temperature of 130°C, as opposed to the 200.5°C suggested here and 195.5°C in [49]. Despite the difference in acceptance bandwidth, the calculation performed here gives a good approximation of the predicted bandwidth, and should be treated as a maximum value, rather than an optimal value, to ensure the best efficiency.

5.3 Experimental Set-up

To incorporate second harmonic generation into the system, an additional free space section was add on at the output of the final amplifier. The key components needed to successfully achieve SHG are primarily the non-linear crystal, where we had chosen LBO, and dichroic mirrors, designed to separate the fundamental and second harmonic from each other after the conversion. In addition the fundamental will be focused into the crystal to increase the energy density, and thus a series of lenses were used to focus and re-collimate the light. Finally a half wave plate was needed to orientate the fundamental light to align with the axis of the crystal to optimise the SHG efficiency.

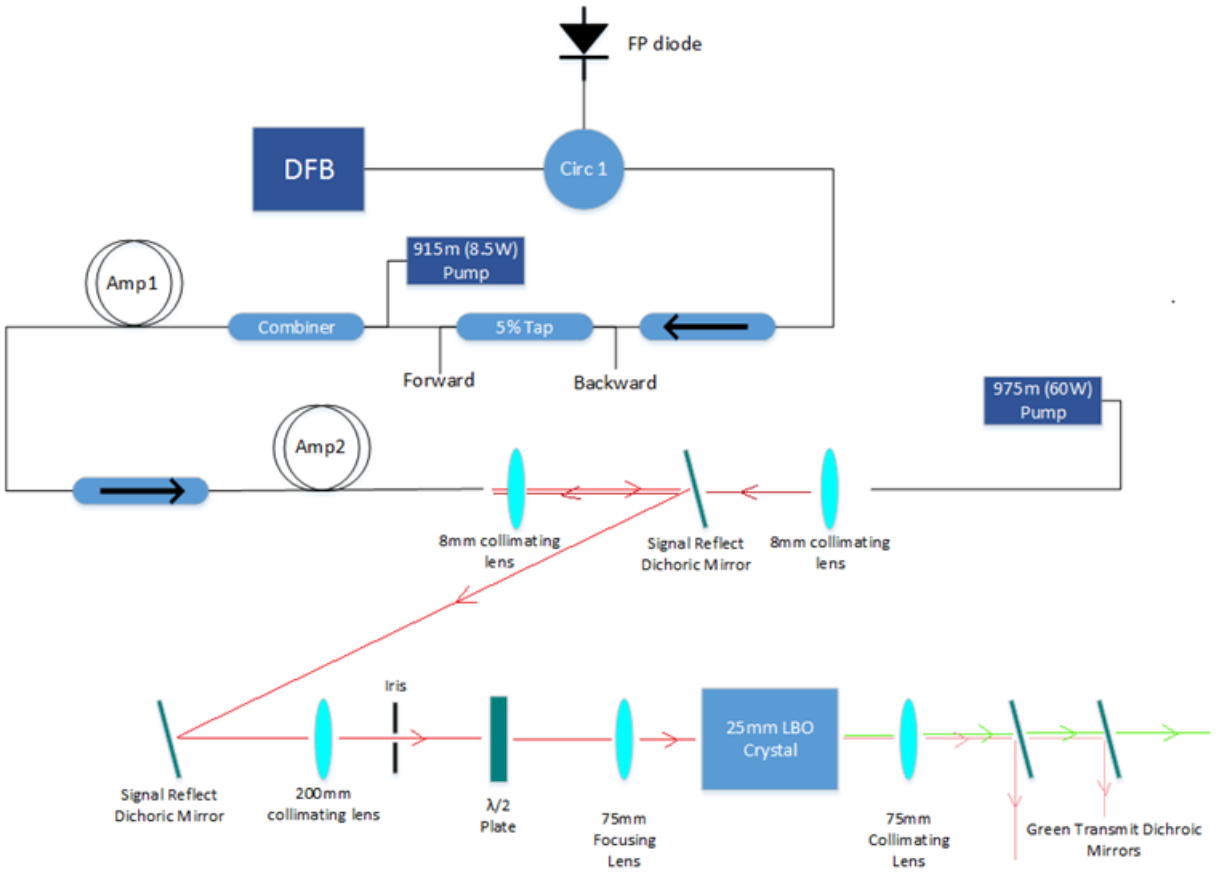

Figure 80: Schematic diagram of the set-up used for second harmonic generation.

The set-up we used, as shown in figure 80, uses two signal (fundamental) reflect mirrors to re-position the beam as well as ensure there is no excess pump light within the beam. An additional 200mm collimating lens was then added as the light at this point was slightly divergent. The iris was used to eliminate any cladding guided light that was present within the system. While the beam was collimated it was passed through a half wave plate to rotate the polarisation to match that of the LBO crystal. The initial position of the waveplate was not crucial as once the system was running, tuning the waveplate would give a noticeable change to the output power in the second harmonic, allowing for optimisation. Before entering the crystal, the light was focused into the crystal, and re-collimated after exiting. Finally two dichroic mirrors were used at the output of the system to separate the fundamental and second harmonic light. The chosen mirrors reflected the fundamental and allowed the second harmonic to transmit through.

5.4 Experimental Results

For the primary second harmonic generation tests, the seed source was replaced by the ASE source. This would allow us to compare the performances of the two seeds with respect to SHG. The crystal was placed in the path of the collimated fundamental beam, but no additional focusing optics were used. This was primarily to check for any initial conversion to confirm the alignment, crystal specifications and energy output of the system. With only Amp1 pumped, it was possible to see generated green light with the naked eye. However due to the sensitivity of the human eye the power levels were particularly low. Despite this, it did confirm that there was some level of conversion that could then be measured and optimised by increasing the fundamental output power, rotating the polarisation and focusing the beam into the crystal.

To begin to optimise the conversion, the final amplifier was lightly pumped, at a current of 1.4A. This produced less than 1mW of second harmonic light, with an input power of 0.529W. For this initial measurement the crystal was heated to 155 degrees. The first and easiest optimisation was to add the half wave plate before the crystal. By measuring the second harmonic power while rotating the half wave plate the optimal position could be found, resulting in the output power increasing to 61.6mW. The crystal was mounted on a 5-axis stage allowing for precise tuning of the position, initial re-alignment maximised the conversion when the crystal was at a significant angle, rather than perpendicular to the incoming beam. This was due to the phase matching condition at the current temperature. To rectify this, the crystal was aligned perpendicular to the beam and then the temperature was adjusted. Given the nature of the phase matching's sinc function, the temperature had to be tuned over a large range to ensure that the maximum conversion was due to the peak of the curve rather than a local maximum. In the set-up used we found the optimum temperature to be 148.5 degrees. The final optimisation was to add a focusing lens before the crystal to reduce the spot size within the crystal. Both a 100mm and a 75mm lens were tests, with 75mm giving slightly higher conversion.

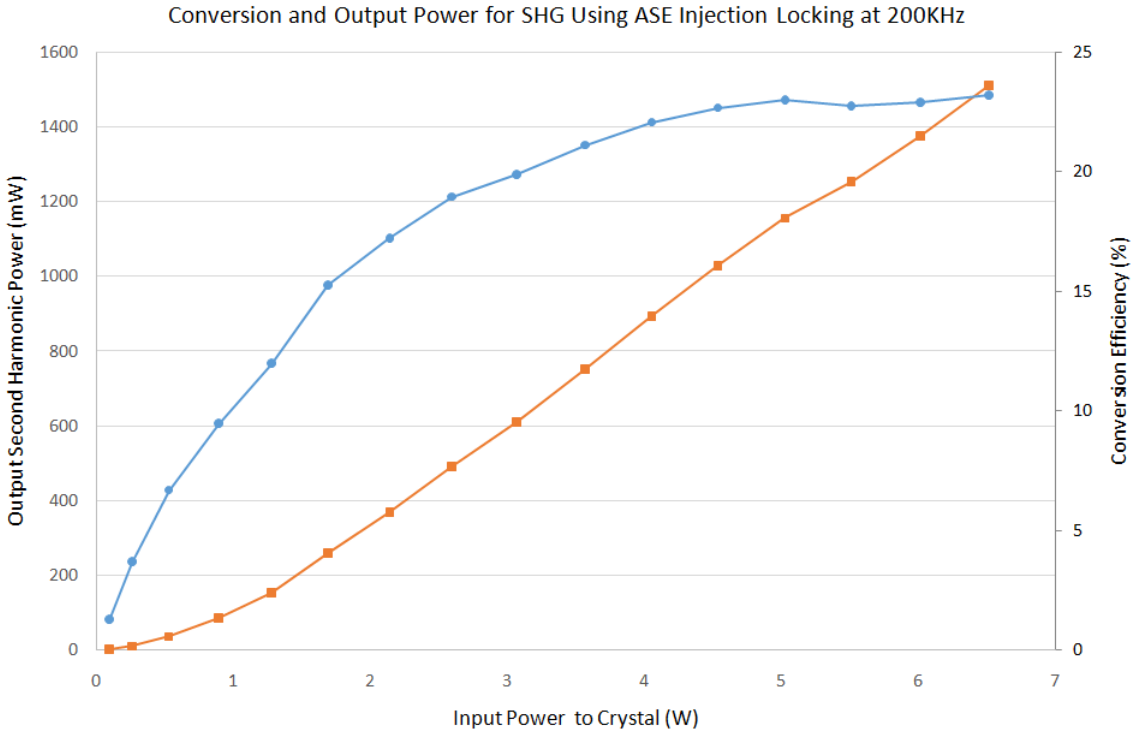

Figure 81: Output Power and conversion efficiency for ASE injection locked system running at 200kHz. Output power shown in orange, and conversion efficiency in blue.

With the system optimised, the ASE injection locked system was able to reach a conversion efficiency of 23% as shown in figure 81. Despite trying to further optimise with different focusing lenses, a change of crystal position and orientation, the efficiency never rose above this value. This is likely due to the large bandwidth produced when using the ASE source. Therefore the system was swapped back to using the DFB injection to compare the performance.

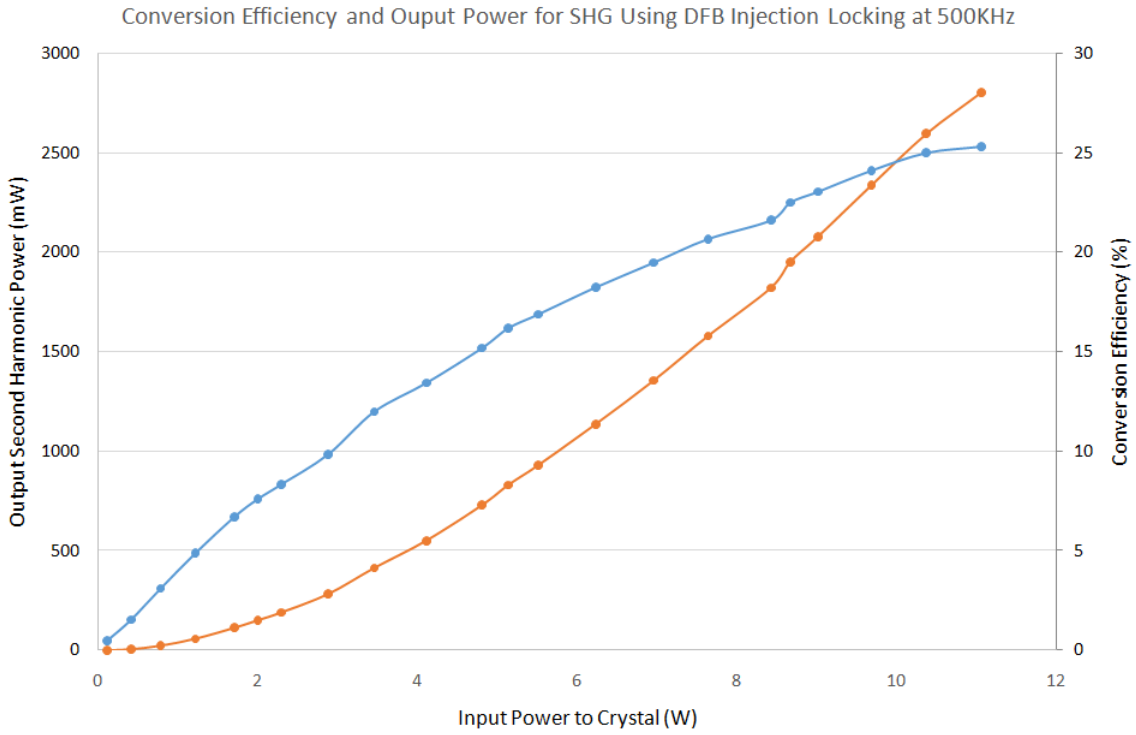

Figure 82: Output Power and conversion efficiency for DFB injection locked system running at 200kHz. Output power shown in orange, and conversion efficiency in blue.

Figure 82 shows the results for the DFB injection set-up, where the conversion efficiency reached 25.3%, a slight increase over the ASE set-up. Although due to the frequency difference, the DFB system is running at a lower peak power, the significantly reduced bandwidth should allow the system to perform better. In order to get a significant improvement in the conversion efficiency the earlier amplifier stages would likely need to be redesigned, due to the developing needs and targets the system has undergone from its first construction, thus the amplifier lengths are no longer specifically designed for this operation. However despite this, the DFB system was able to reach a second harmonic energy of more than 5μJ, which is more than required to be able to incorporate the system into UCL's imaging set-up. Therefore it was decided to continue with the DFB system as it offered the most potential for future improvement.

To develop the system to UCL's requirements, ideally both the pulse width and repetition rate should be flexible. However given the issues with the presence of CW light when the diode driver is adjusted, there was very little flexibility in pulse length that we could offer. Despite this, the pulses generated had a suitable length, between 1-3ns. In order to confidently provide a range of repetition rates, the system was tested over a frequency range from 100kHz to 1MHz. Due to the changes in peak powers as the frequency was changed, the pre-amplifier and Amp1 current settings were adjusted at each frequency to maintain a similar level of power entering the next amplifier, to ensure no non-linear effects developed as the frequency was reduced. The maximum peak powers were targeted to all be similar values, around 10kW, however the 100kHz test was only tested up to a maximum of 8kW as to not stress the system, while the 1MHz tests were only run up to a maximum of 5kW due to not wanting to push the pump diode harder than needed.

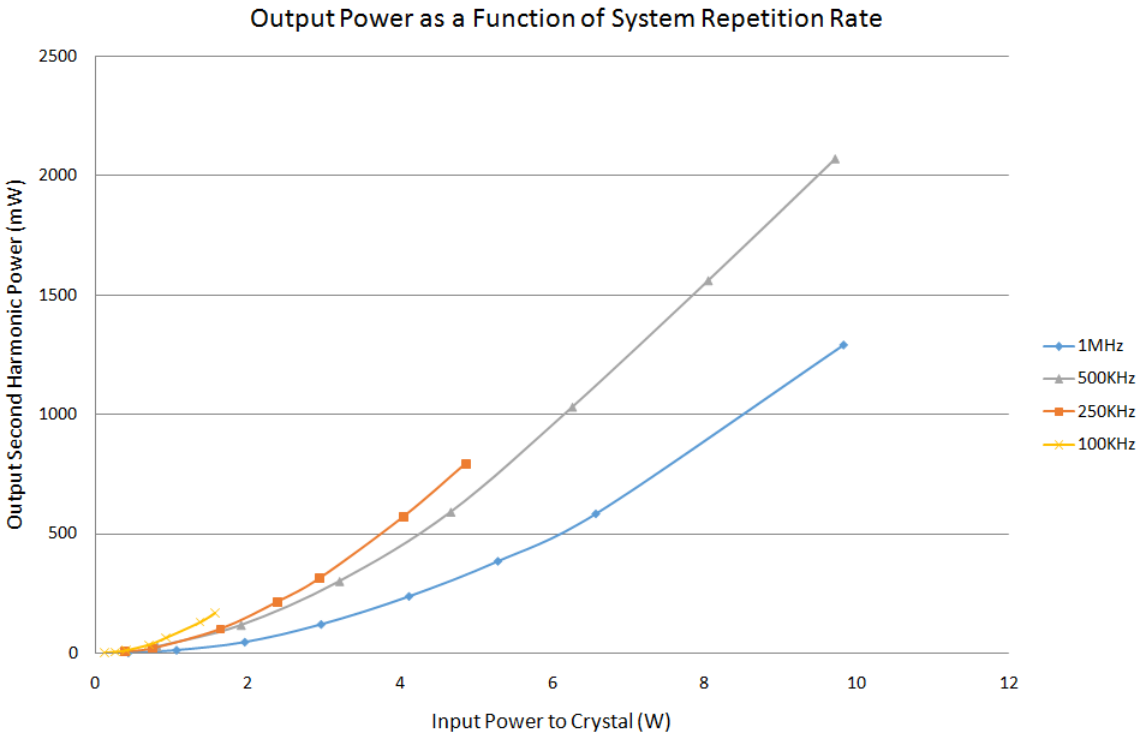

Figure 83: Output Power for the DFB system at varying repetition rates, ranging from 100kHz to 1MHz

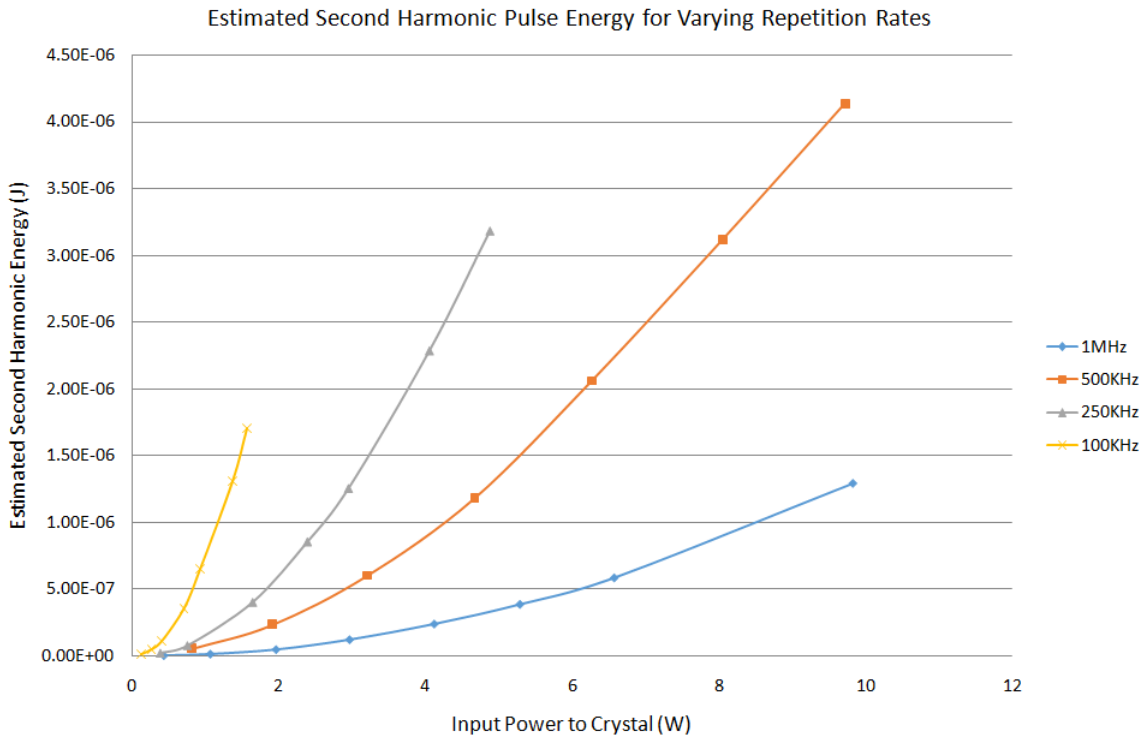

Figure 84: Estimated second harmonic pulse energy at varying repetition rates, ranging from 100kHz to 1MHz

From the results shown in figures 83 and 84 it can be seen that at any repetition rate between 100kHz and 1MHz the system is able to produce at least 1μJ of pulse energy at the second harmonic, with a maximum of 4μJ available at 500kHz. Therefore the system has a wide range of repetition rates available that will all produce the desired 1μJ needed to be integrated into UCL's imaging system successfully.

As a final check of the system, the beam quality was measured. In order to measure the beam quality, the second harmonic beam was reflected into a beam profiler. A 150mm lens was used to focus the beam to a waist within the travel of the beam profiler. The results shown in figure 85. The measurement was taken by moving the position of the beam profiler and recording the beam width. This data was then plotted and fit in MatLab. Due to the position of the profiler being manually changed, as well as fluctuations in the readings from the beam profiler the data does not fit the theoretical fit line perfectly. This can also be seen in the M^2 value less than one for the Y axis. However, despite this, the values are both very close to one, indicating that the beam is likely to be close to diffraction limited.

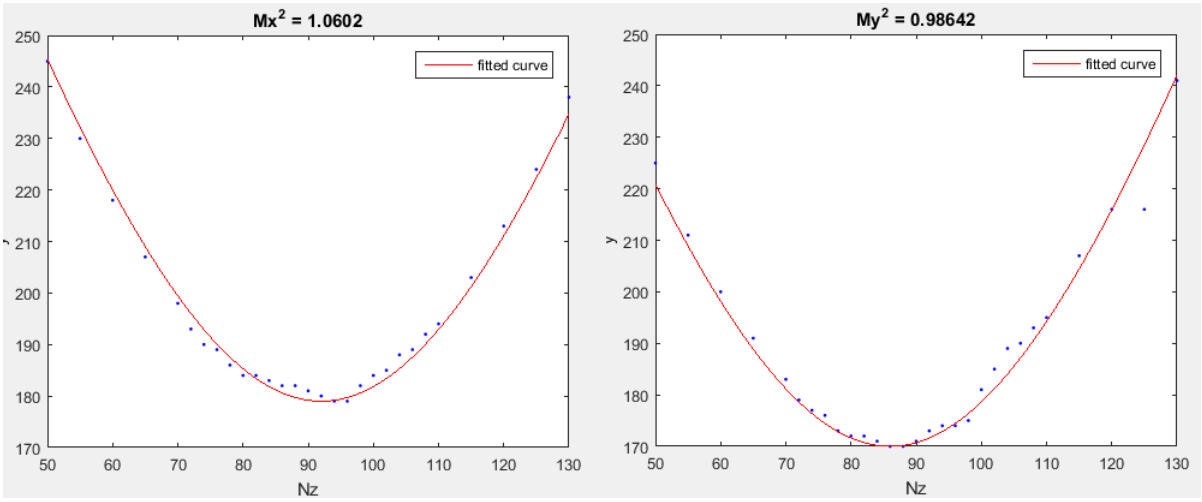

Figure 85: M^2 measurement of the second harmonic beam

To further check the reliability of the M^2 measurement, the values for the input and output fundamental beams were also measured. If the fundamental beam remained diffraction limited then the generated beam would also be.

Figure 86 shows that both before and after the crystal the M^2 measurements are all around 1, suggesting that at all points the beam is close to diffraction limited. The measurements do seem to suggest that the output M^2 may be higher than the input which could result in a slightly higher M^2 in the second harmonic beam. However, the highest recorded measurement for is an M^2 of 1.12, and therefore we can confidently say that the M^2 is less than 1.2.

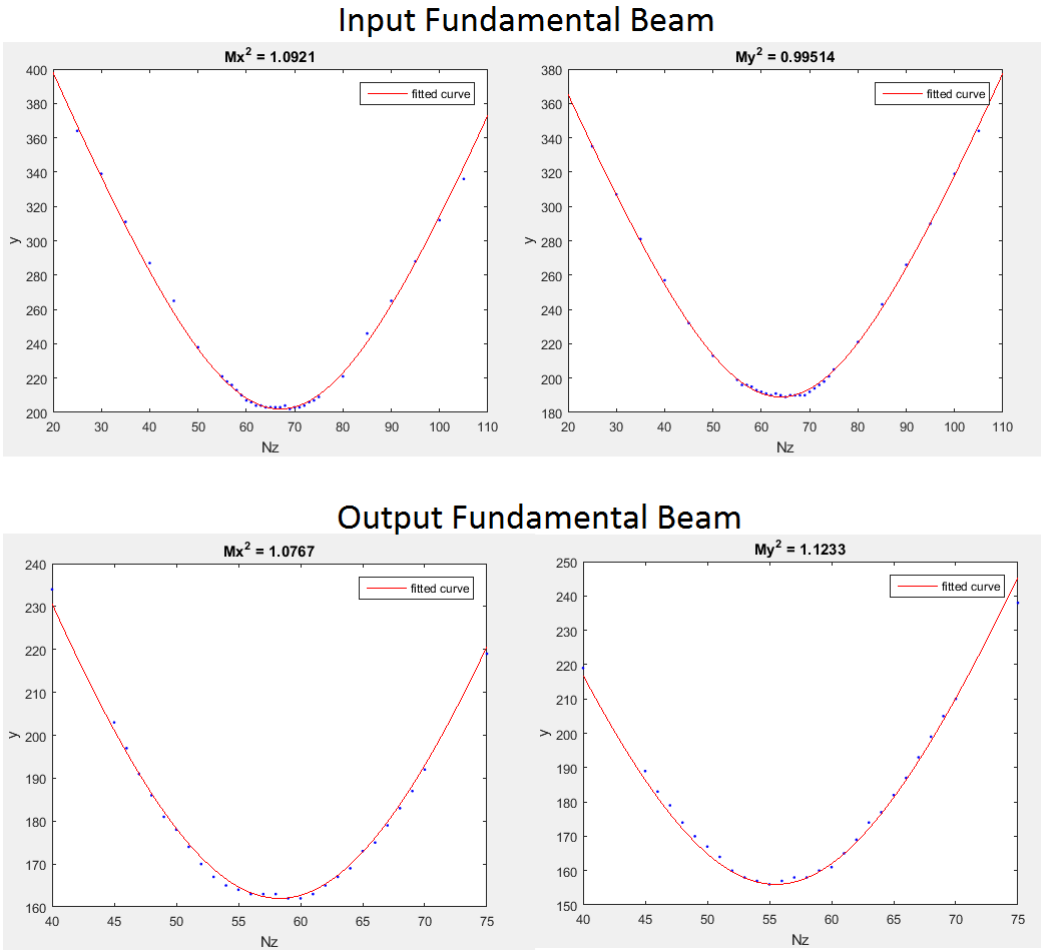

Figure 86: M^2 measurement of the fundamental beam, both before (top) and after (bottom) the crystal

With the system capable of producing sufficient energy as well as providing a large tuning range over the operation frequency, and a suitably low M^2 value, the system was ready to be moved to UCL to integrate with their imaging set up and test the system as a whole. The system was enclosed in a aluminium case to both provide protection during transport as well as contain stray light while being operated at UCL.

Initial tests carried out at UCL were testing the systems capabilities using phantoms. These are artificial constructs that are used to represent tissue samples. Tests using a leaf phantom were used to get initial ideas on how long the scans would take to acquire an image as well as clarity of the image.

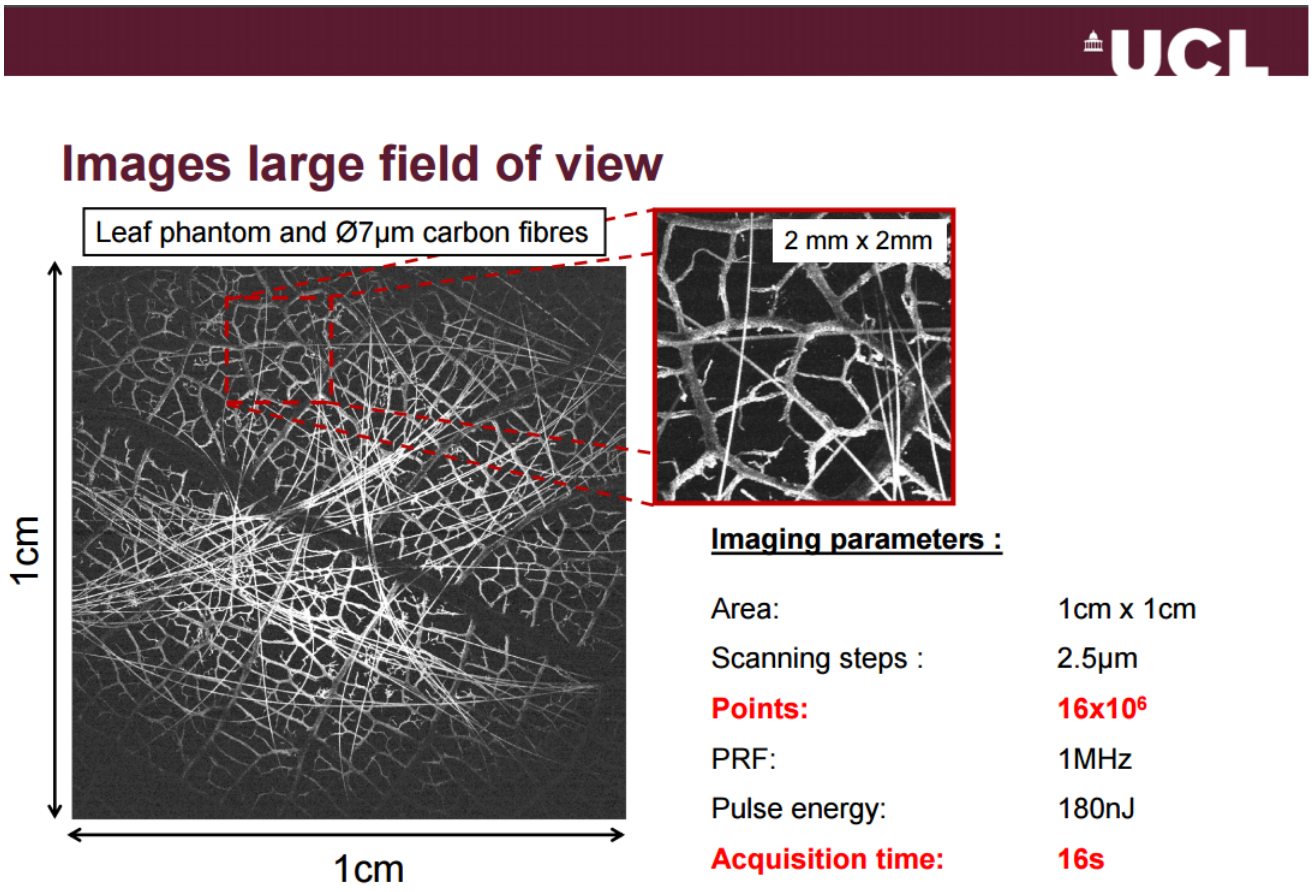

Figure 87: Image taken by using the OR-PAM system with the leaf phantom. Image from UCL publication[53]

The image shown in figure 87 was taken using the OR-PAM system running at a repetition frequency of 1MHz, and took only 16 seconds to acquire an image. The image is of a suitably high resolution such that a clear 2mm x 2mm section can be zoomed in on and still looks clear. Having successfully generated a good image from a phantom, the testing could progress onto imaging biological tissue. For tests using biological tissue, higher energies are needed, and thus the repetition rate was reduced down to 500kHz. The image created in figure 88, depicts a section of a mouse ear.

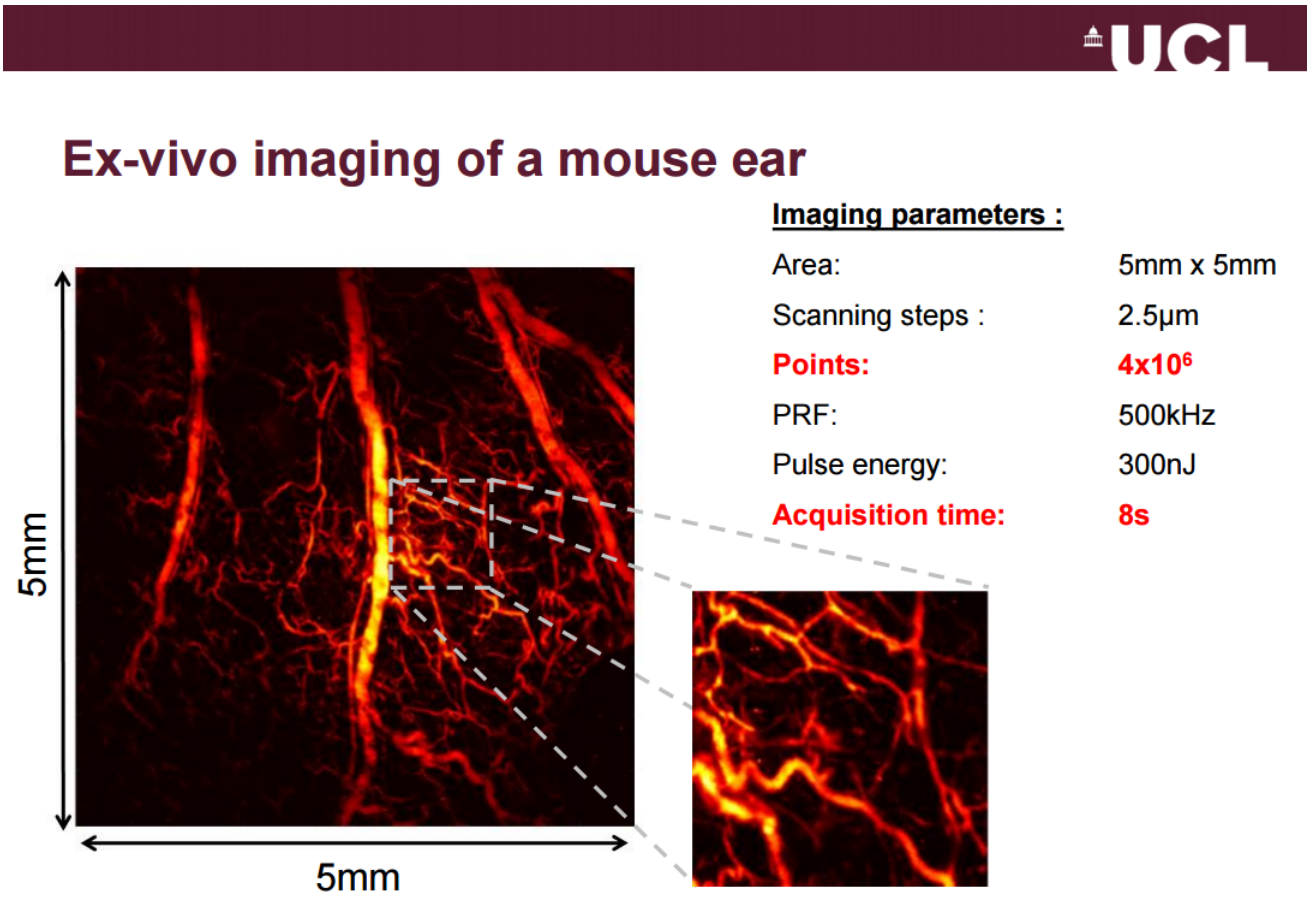

Figure 88: Image taken by using the OR-PAM system of a mouse ear. Image from UCL publication[53]

Being able to successfully produce an image using a biological tissue sample shows that the fibre system we delivered was suitable for the application and the tunable repetition rate was highly useful for different imaging systems. In an attempt to push the system beyond other similar systems, UCL ran the system at 2MHz repetition rate with a pulse energy of 100nJ. The test was aiming to produce a clear image in the quickest time possible, which would help to realise photoacoustic imaging as a useful medical technique.

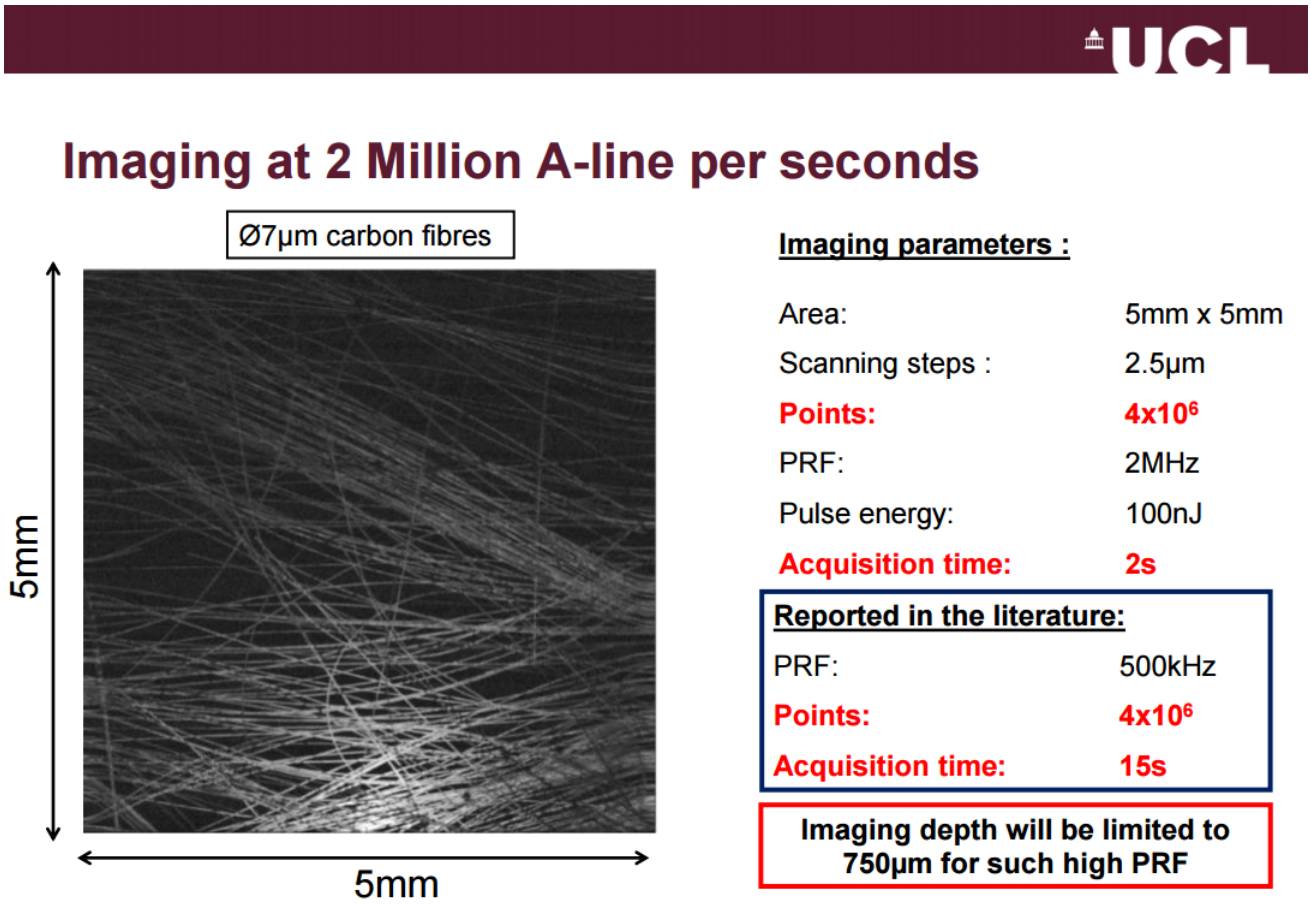

Figure 89: Image taken by using the OR-PAM system running at 2MHz, four times that of competitive systems. Image from UCL publication[53]

As shown in figure 89 the system successfully obtained a clear image at 2MHz, not only that but it only took 2seconds. This acquisition time is significantly lower than similar systems found in the literature. As noted in figure 89 running the system at such a high repetition rate will limit the penetration depth. This may be an issue in certain circumstances, but the speed of the system will be a big positive in others.

5.5 Conclusion

LBO was the chosen crystal for this experiments, mainly due to its high damage threshold and the operation in non-critical phase matching regime, allowing for temperature tuning to optimise the conversion efficiency. The crystal was integrated into the system using free space coupling, alongside the aids of focusing optics and a half waveplate to orientate the polarisation of the signal to that of the crystal. Both the ASE and DFB systems were tested with both reaching efficiencies around 25% before plateauing. Despite the maximum efficiency being lower than theoretical ideals, there was still sufficient second harmonic power for UCL to be able to take advantage of. Due to the size and complexity difference as well as narrower spectral width, the DFB system was chosen to be tested at UCL. Further characterisation of the system showed it was capable of producing over 1μJ pulse energy at a any repetition rate between 100kHz and 1MHz, while maintaining a high beam quality with an M^2 less than 1.15. Successful tests at UCL indicated that the system was suitable for the purpose and allowed for the generation of clear photoacoustic images, which set record breaking acquisition times.

6 Conclusions and Future Work

6.1 Summary of Results

The photoacoustic tomography system was initially designed as an 8 amplifier MOPA system, consisting of 3 seed amplifiers, two pre-amplifiers and 3 power amplifiers. The system relied on an amplified and filtered ASE source as a seed which was then amplified and modulated using an AOM. Due to the dimensions of the final amplifier stage, initially 50μm core diameter, the system was free space coupled and bidirectionally pumped. The system was able to reach a maximum pulse energy of 2.5mJ, being limited by the energy storage capability of the final amplifier stage. To improve upon the performance, various large core fibres were tests, with an in house manufactured fibre, with a core diameter of 96μm, performing best. The addition of this fibre to the system resulted in a maximum pulse energy of 9.7mJ.

Due to the large size of the first PAT system, a second portable system was constructed. To help reduce the physical size of the system, a filtered and amplified SLED was used as the seed source. This enabled us to remove several amplifiers as well as the AOM from the system. Resulting in a system comprising of 4 amplifiers. This system was only capable of producing a maximum pulse energy of 5mJ, however was significantly smaller, and suitable to delivery to UCL for initial testing purposes. The laser system has remained with UCL for almost a year, receiving positive feedback and results, including enabling them to achieve world leading results [53].

The optical resolution photoacoustic microscopy system initially comprised of 3 amplifiers, as well as both an EOM and an AOM for modulation purposes. The seed source used was a grating locked Fabry-Perot diode. The EOM was used to carve short pulses as well as define the shape of the pulses, while the AOM was implemented to reduce the frequency of the system to 1kHz. This way the system could be used for both OR-PAM and PAT tests. Initial issues with SBS arose, however these were solved by reducing the EOM opening window. At higher pump powers there was a clear Raman peak present which was limiting the capabilities of the system. It was concluded that the system should be refined to specifically target OR-PAM only, to reduce the requirements on the system.

The refined OR-PAM system opted to remove both the AOM, as there was no longer a need to reduce the repetition rate, and the EOM as it was a particularly delicate component, limiting the power that could be generated early within the system. This new system relied on the injection locking of a FP diode using an amplified and filtered ASE source. The system used 2 amplifiers within the main part of the system, and an additional amplifier within the ASE source. This system was capable of producing over 6W of output power at 100kHz. However the signal experienced significant broadening throughout the amplifier chain, reaching a 3dB width greater than 0.5nm.

The solution to the large bandwidth was to replace the ASE source with a DFB laser diode, ensuring that the system started with a highly narrow bandwidth. With the same amplifier chain, the system was able to produce comparable power while retaining a bandwidth of less than 0.04nm. Due to limitations with the FP diode driver, there was little flexibility in the pulse width and shape.

Second harmonic experiments were conducted using an LBO crystal with both the ASE and DFB injection locked system. Both performed very similarly, however due to the significantly narrower spectral width when using the DFB, this system was chosen to be developed and finalised into a deliverable system. The system was tested over a range of repetition rates, from 100kHz up to 1MHz, and was shown to be able to produce at least 1μJ at all repetition rates which was initially required by UCL in order for the system to be used to produce useful biological images. This final system was delivered to UCL, and they were able to take images at both 500MHz and 1MHz of both phantoms as well as biological tissue. The system was also run at 2MHz to successfully acquire an image at a record breaking speed of 2 seconds.

6.2 Future Work

The test system delivered to UCL successfully met the goals for OR-PAM system, with all the specifications meeting the ideal parameters apart from the ability to tune the wavelength, and some control over the pulse width and shape. In order to fulfil these criteria in the future, the system needs to be further developed to incorporate two further frequency conversion stages. A sum frequency generation stage is needed to generate the third harmonic, and finally an OPO stage is needed to provide a range of wavelengths.

6.2.1 Sum Frequency Generation

In order to produce a tunable wavelength over the entire visible spectrum, an OPO will be required. However the pump frequency needs required for a suitable OPO falls around the third harmonic of our system rather than the second, and therefore an additional frequency conversion stage is required before the OPO. As mentioned in section 2.3 a process known as sum frequency generation can be used. This process is very similar to the ideas behind SHG, however there are now two input waves. Using an identical method, the second order polarisation can be calculated using equation 18, but this time the electric field input must be made up of two components, at frequency ω_1 and ω_2, shown in equation 49. By substituting this new expression for the electric field into the second order polarisation, several additional terms are generated, as shown in equation 50. Each term of the equation corresponds to a different non-linear generation. The first term and second term are both SHG terms at ω_1 and ω_2 respectively. The third term, $2E_1E_2e^{-i(\omega_1+\omega_2)t}$ represents the SFG, and can be seen in the exponent term that contains $\omega_1 + \omega_2$. The fourth term represents difference frequency generation where the generated frequency is at $\omega_1 - \omega_2$. The final term represents optical rectification as it has no dependence upon the frequency. Despite multiple non-linear terms being present, only one process will be generated with substantial power in practice, due to different phase matching conditions.

$$E(t) = E_1e^{-i\omega_1 t} + E_2e^{-i\omega_2 t} + c.c \tag{49}$$

$$P^{(2)}(t) = \epsilon_0\chi^{(2)}\left[E_1^2e^{-2i\omega_1 t} + E_2^2e^{-2i\omega_2 t} + 2E_1E_2e^{-i(\omega_1+\omega_2)t} + 2E_1E_2^*e^{-i(\omega_1-\omega_2)t} + c.c\right] + 2\epsilon_0\chi^{(2)}\left[E_1E_1^* + E_2E_2^*\right] \tag{50}$$

The third harmonic wave needs to be generated in order to be used as a pump wavelength for the OPO. As mentioned in section 1.4 the third harmonic can be generated either directly through THG, or via SFG. For this experiment we opted to obtain the third harmonic via SFG, using a combination of the fundamental and second harmonic waves. Many of the same factors as SHG need to be taken into consideration with SFG. Once again, due to the high damage threshold and transparency at the operational wavelengths, an LBO crystal was deemed the most suitable. Unlike the SHG case, we can no longer operate the crystal in a NCPM regime, and have to rely upon critical phase matching. This implies that in order to reach a phase matching condition, the crystal needs to be accurately angle tuned. In order to achieve this, the crystal will be mounted on a 5 axis stage allowing the maximum possible adjustments. Due to having two inputs to the crystal this time, the decision between type one and two has a more significant impact. Since the crystal used for SHG is type 1, the second harmonic wave is produced at the opposite linear polarisation to the pump source. This means that the two inputs to the SFG crystal have perpendicular polarisations, making a type 2 crystal the clear choice, as it requires no additional optics to rotate one of the polarisations. Additionally, as walk-off effects will now be have an impact, type 2 LBO posses a lower walk-off angle than type 1 [54].

The efficiency calculation for SFG is more complex than that for SHG even in the plane wave case, and is shown in equation 51[55]. The efficiency is described by the Jacobi elliptic sine function, where γ is given in equation 53, where $P_{p2}(0)$ and $P_{p1}(0)$ represent the initial powers of the second harmonic wave and fundamental wave respectively.

$$\eta_{SFG} = sn^2[(L/L_{NL}), \gamma] \tag{51}$$

$$L_{NL} = \frac{1}{4\pi d_{eff}} \sqrt{\frac{2\epsilon_0 n_{p1} n_{p2} n_3 c \lambda_{p2} \lambda_s}{I_{p1}(0)}} \tag{52}$$

$$\gamma = \frac{\lambda_{p2} P_{p2}(0)}{\lambda_{p1} P_{p1}(0)} \tag{53}$$

Where L is the length of the crystal, d_{eff} is the non-linearity of the crystal and I_{p1} is the intensity of the fundamental pump wave.

The Jacobi elliptic sine function behaves such that as γ tends to 0, $sn(u, \gamma) \approx sin(u)$, and as γ tends to one $sn(u, \gamma) \rightarrow tanh(u)$. Figure 90 shows how the efficiency function varies for different values of gamma, which in the case of this experiment will depend upon the efficiency achieved by the SHG stage, and will be at a maximum, of 1, when there is twice the power in the second harmonic as there is in the fundamental. This condition is achieved when a SHG conversion efficiency of 66.66 % is achieved.

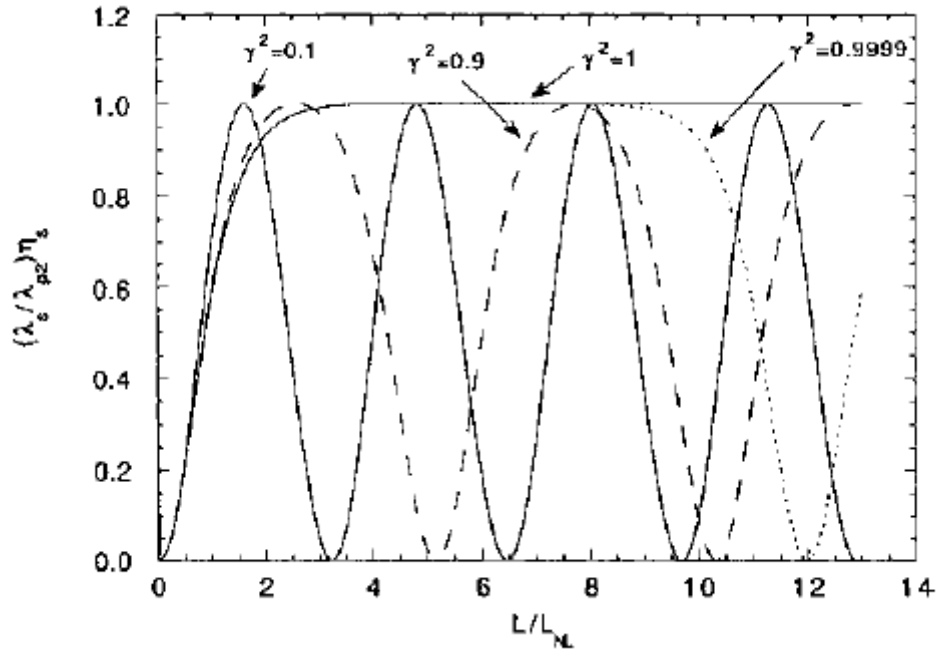

Figure 90: Plot of the SFG efficiency for various values of gamma [55]

To physically set up this additional conversion stage, both the converted second harmonic and the residual fundamental from the SHG stage need to be collimated and focused through an additional crystal designed for sum frequency generation. The output third harmonic signal would then need to be separated from any remaining input after conversion using dichroic mirrors. Due to a finite conversion efficiency there would be a further drop in usable energy after the conversion stage, and therefore it may be necessary to further improve the SHG efficiency such that around 50% of the fundamental is converted, resulting in an equal input to the THG stage.

6.2.2 Optical Parametric Oscillator

Initial calculations will need to be made to predict the threshold value, optimum crystal length and focusing condition. With these calculations, an informed decision on the operating conditions can be made, and a suitable cavity built. Initial literature reviews suggest that using a BBO crystal will be most suited [56][57], as it has a higher non-linearity than other suitable crystals, such as LBO, leading to higher conversion efficiencies, which in turn will help to lower the threshold of the OPO. However, LBO has the advantage that it has a smaller walk-off, allowing tighter focused beams to be used, which in turn increase the intensity within the crystal. As nanosecond pulses are being used, a linear cavity made from two plane mirrors is suitable, as by keeping the cavity length short, the pulse can fill it entirely. This makes building and aligning the OPO cavity more simple than having to rely upon a bow-tie style cavity.

Due to the operating wavelengths of the OPO being fixed, initial designs for cavity mirrors have been started. Each mirror in the linear cavity serves a different purpose, and custom coatings need to be used to specifically tailor the mirrors to the experimental needs. The input mirror needs to allow the pump (355nm) to enter the cavity, but reflect the signal wavelength (450-700nnm), design by Laseroptik shown in figure 91. The output mirror is used as an output coupler, where some portion of the signal can be extracted. Therefore the coating must have a signal reflectivity of less than one. However, in order to set-up stable oscillation within the cavity, a large fraction of the signal needs to be reflected back into the cavity, design by Laseroptik shown in figure 92. Therefore the key aspect of the mirror coatings is to define the output coupling fraction. In addition, the output coupler can reflect the pump wavelength, resulting in a double pass of the pump. After finishing my experimental work at UoS, Dr Lin Xu was able to further develop a similar MOPA system which successfully produced the third harmonic frequency using sum frequency generation. A set of custom mirrors as discussed was ordered and tested in an attempt to generate the tunable OPO frequencies. Unfortunately it was not possible to get the OPO operating. This was due to absorption of the OPO pump wavelength in the mirror coating.

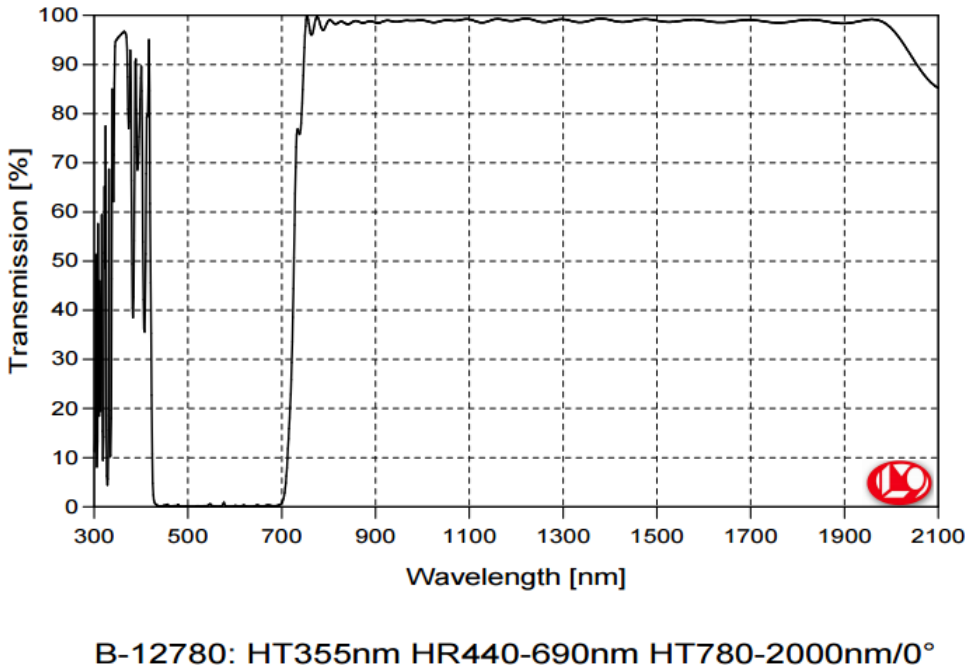

Figure 91: Design for the input OPO cavity mirror, transmitting as much of the signal as possible, while retaining a highly reflective region around the visible signal wavelengths. Designed by Laseroptik

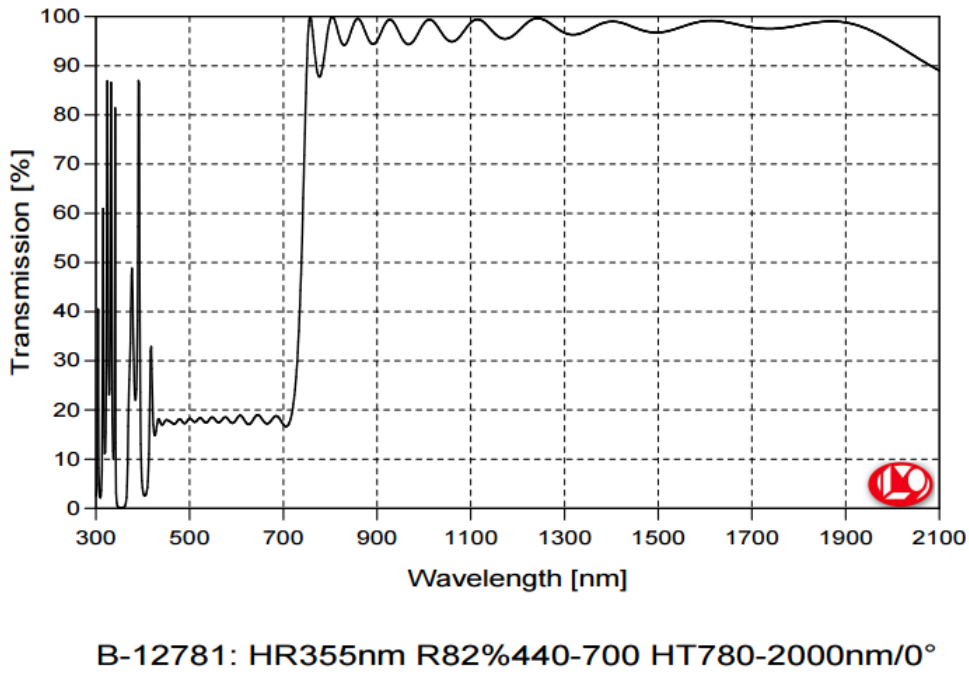

Figure 92: Design for the output OPO cavity mirror, an initial proposed 20% transmission for the signal region, to allow a significant portion of the signal power to stay within the cavity. Designed by Laseroptik

References

[1] Paul Beard (2011) Biomedical photoacoustic imaging Interface Focus 1 602−631

[2] RECENDT 2009 Photoacoustic Imaging Available at: http://www.recendt.at/528_ENG_HTML.php Accessed 9 May 2014

[3] UCL Department of Medical Physics and Bioengineering 2005 Photoacoustic Imaging Group Available at: http://www.medphys.ucl.ac.uk/research/mle/images.htm Accessed 21 May 2014

[4] Nuclear AMRC 2014 Laser Processing R&D Available at: http://namrc.co.uk/capabilities/innovation/laser-processing Accessed 25 Jan 2015

[5] ORC 2015 How Fibre Lasers Work Available at: http://www.orc.soton.ac.uk/61.html Accessed 16 Jan 2015

[6] Yulia Pinchasov-Grinblat and Zvy Dubinsky (2012). Photoacoustics: A Potent Tool for the Study of Energy Fluxes in Photosynthesis Research, Artificial Photosynthesis, Dr Mohammad Najafpour (Ed.), ISBN: 978−953−307−966−0, InTech, Available from: http://www.intechopen.com/books/artificial-photosynthesis/photoacousticsa-potent-tool-for-the-study-of-energy-fluxes-in-photosynthesis-research

[7] Roy G. M. Kolkman, Erwin Hondebrink, Wiendelt Steenbergen, and Frits F. M. de Mul (2003) In Vivo Photoacoustic Imaging of Blood Vessels Using an Extreme-Narrow Aperture Sensor IEEE Journal of Selected Toprics in Quantum Electronics, Vol. 9 No. 2 343−346

[8] D. Keck (2000) Optical fiber spans 30 years Lightwave Vol. 17 No. 8 7882

[9] S.B. Poole, D.N. Payne and M.E. Fermann (1985) Fabrication of low loss optical fibres containing rare earth ions Election Letters Vol. 21 Issue 17 737−738

[10] Robert Hall et al (1962) Coherent Light Emission From GaAs Junctions Phys. Rev. Lett. Vol. 9 Issue 9 366−368

[11] Jeff Hecht (2016) A Fiber-Optic Chronology Available at: http://www.jeffhecht.com/chron.html Accessed 12 Jan 2016

[12] R.J. Mears, L.Reekie, I.M. Jauncey and D.N. Payne (1987) Low-noise erbium-doped fibre amplifier operating at 1.54μm Electronics Letters Vol. 23 Issue 19 1026−1028

[13] B.Desthieux, R.i. Laming and D.N. Payne 1993 111kW (0.5 mJ) pulse amplification at 1.5 μm using a gated cascade of three erbium-doped fiber amplifiers Appl. Phys. Lett. 63(5) 586−588

[14] Ming-Yuan Cheng, Yu-Chung Chang, Almantas Galvanauskas, Pri Mamidipudi, Rupak Changkakoti and Peter Gatchell 2004 High-energy and high-peak-power nanosecond pulse generation with beam quality control in 200-μm core highly multimode Yb-doped fiber amplifiers Optics Letters 30(4) 358−360

[15] Dejiao Lin, Shaif-ul Alam, KangKang Chen, Andrew Malinowski, Steve Norman and David Richardson 2009 100W, Fully-Fiberised Ytterbium Doped Master Oscillator Power Amplifier Incorporating Adaptive Pulse Shaping Conference on Lasers and Electro-Optics Baltimore, Maryland United States

[16] A.Malinowski, P.Gorman, C.A.Codemard, F.Ghiringhelli, A.J.Boyland, A.Marshall, M.N.Zervas and M.K. Durkin 2013 High-peak-power, high-energy, high-average-power pulse fiber laser system with versatile pulse duration and shape Optics Letters 38(22) 4686−4689

[17] Newport, 2015, Tutorial: Fibre Optic Basics, Available at: https://www.newport.com/t/fiber-optic-basics Accessed March 2015

[18] C. N. Pannell, P. St. J. Russell, and T. P. Newson (1993) Stimulated Brillouin scattering in optical fibers: the effects of optical amplification J. Opt. Soc. Am. B 10, 684−690

[19] Robert W. Boyd, 2008, Nonlinear Optics, Academic Press 3rd edition

[20] N.Bloembergen and P.S.Pershan Light Waves at the Boundary of Nonlinear Media 1962 Phys. Rev. 128 606

[21] C.Chaungtian, W.Yicheng, J.Aidong, W.Bochang, and Y.Guming 1989 Lithium borate, laser systems U.S Patnent 4826283 A

[22] D.N.Nikogosyan 1991 Beta Barium Borate (BBO) Applied Physics A 52 359−368

[23] Y.X.Fan, R.C.Eckardt, R.L.Byer, C.Chen and A.D.Jiang 1989 Barium Borate Optical Parametric Oscillator IEEE Journal of Quantum Electronics Vol.25 No.6

[24] P.S.Banks, M.D.Feit and M.D.Perry 1999 High-intensity Third-harmonic Generation in Beta Barium Borate Through Second-order and Third-order Susceptibilities Optics letters Vol.23 No.1 4−6

[25] S.P.Velsko, M.Webb, L.Davis, C.Huang 1991 Phase-Matched Harmonic Generation in Lithium Triborate (LBO) IEEE Journal of Quantum Electronics Vol.27 No.9 2182−2192

[26] Paschotta, R., Nilsson, J., Tropper, A.C. and Hanna, D.C. (1997) Ytterbium-doped fibre amplifiers IEEE Journal of quantum electronics Vol. 33 No.7 1049−1056

[27] RP Photnics, 2012, RP Photonics Encyclopaedia, Available at: http://www.rp-photonics.com/encyclopedia.html Accessed 16 March 2015

[28] Firecomms, 2012, About Optical Fibres, Available at: http://www.firecomms.com/products-about-fibers.html Accessed August 2015

[29] Thorlabs, 2016, Polarization-Maintaining (PM) Fibre, Available at: https://www.thorlabs.com/newgrouppage9.cfm?objectgroup-id=2410 Accessed August 2015

[30] Newport, 2015, Fibre Optics: How Fused Fibre Optic Couplers Work, Available at: https://www.newport.com/medias/sys-master/images/images/h86/hb2/8797287088158/Tech-Note-26-How-Fused-Fiber-Optic-Couplers-Work.pdf Accessed December 2015

[31] Kafka J. (1989) Laser Diode Pumped Fiber Laser With Pump Cavity US Patent 4,829

[32] Coherent, 2016, Ytterbium-Doped Large-Mode-Area Double-Clad Fiber - LMA-20/490, Available at: https://www.coherent.com/products/?1755/Ytterbium-Doped-Large-Mode-Area-Double-Clad-Fiber-LMA-20-490 Accessed July 2015

[33] S.Kobtsev and S.Kukarin (2008) Hybrid bulk/fibre MOPA system based on Yb:KYW laser SPIE Solid State Lasers XVII: Technology and Devices Vol 6871

[34] C. Jauregui, S. Bhme, G. Wenetiadis, J. Limpert, and A. Tnnermann (2010) Side-pump combiner for all-fiber monolithic fiber lasers and amplifiers J. Opt. Soc. Am. B Vol.27 Issue 5 1011-1015

[35] Yuhong Kang (2002) Calculations and Measurements of Raman Gain Coefficients of Different Fiber Types Thesis submitted to The Faculty of the Virginia Polytechnic Institute and State University

[36] G.D. Boyd and D.A. Kleinman (1968) Parametric Interaction of Focused Gaussian Light Beams, Journal of Applied Physics Vol. 39 Issue 8 2597-3639

[37] Photline Technologies 2011 A review of $LiNbO_3$ modulators specifications Available at: http://www.photline.com/filer/get/14/ReviewModulSpecs.pdf Accessed 21 May 2014

[38] Ophir Photonics 2016 M2 Beam Propagation: Why So Many Different Approaches to Measurement Instrumentation Available at: http://www.ophiropt.com/laser-measurement-instruments/beam-profilers/knowledge-center/tutorial/m2-beam-propagation Accessed November 2016

[39] Elent A, 2013, Acousto-optical modulators (AOM), Available at: http://www.elent-a.net/index.php/en/products-2/teo2-crystals/acousto-optical-applications/acousto-optical-modulators Accessed February 2016

[40] M.Berendt et al (2015) 5mJ pulsed Yb-doped all-fiber MOPA seeded by 0.2nm spectrally sliced super luminescent diode 2015 European Conference on Lasers and Electro-optics - European Quantum Electronics Conference, (Optical Society of America, 2015) paper CJ-9-2

[41] Bangzheng Yin, Da Xing, Yi Wang, Yaguang Zeng, Yi Tan and Qun Chen (2004) Fast photoacoustic imaging system based on 320-element linear transducer array Phys. Med. Biol. 49 13391346

[42] Roger J. Zemp, Rachel Bitton, Meng-Lin Li, K. Kirk Shung, George Stoica and Lihong V. Wang (2007) Photoacoustic imaging of the microvasculature with a high-frequency ultrasound array transducer J. Biomed. Opt. 12(1) 010501

[43] Kwang Hyun Song and Lihong V. Wang (2007) Deep reflection-mode photoacoustic imaging of biological tissue J. Biomed. Opt. 12(6), 060503

[44] Optipedia 2014 Properties of Yb-doped fiber Available at: http://en.optipedia.info/lsource-index/fiberlaser-index/fiberlaser-basic/fiberlasers/yb-doped-chara/yb-emission Accessed 25 Jan 2015

[45] F. Anquez, E. Courtade, A. Sivry, P. Suret, and S. Randoux (2010) A high-power tunable Raman fiber ring laser for the investigation of singlet oxygen production from direct laser excitation around 1270 nm Opt. Express 18 Issue 12 22928-22936

[46] Eskma Optics, 2013, Lithium Triborate - LBO Crystals, Available at: http://eksmaoptics.com/nonlinear-and-laser-crystals/nonlinear-crystals/lithium-triborate-lbo-crystals Accessed 11 March 2015

[47] R.Cieslak and W.A.Clarkson, 2011, Internal Resonantly Enhanced Frequency Doubling of Continuous-Wave Fiber Lasers, Optics Letters Vol. 36 No.10 1896 - 1898

[48] Pascal Dupriez, 2007, Advanced High-Power Pulsed Fibre Laser Systems and Their Applications, PhD Thesis, University of Southampton, Faculty of Engineering, Science & Mathematics, Optoelectronics Research Centre

[49] Kyung-Han Hong, Chien-Jen Lai, Aleem Siddiqui, and Franz X. Krtner, 2009, 130-W picosecond green laser based on a frequency-doubled hybrid cryogenic Yb:YAG amplifier, Optics Express, Vol. 17, Issue 19, 16911-16919

[50] N.Hoghooghi, 2012, Injection-Locked Semiconductor Lasers for Realization of Novel RF Photonics Components, PhD Thesis, University of Central Florida, The College of Optics and Photonics

[51] Coherent, 2002, LBO, Available at: http://www.coherent.com/downloads/$LBO_DS.pdf$page=1. Accessed 20 March 2015

[52] Lasertec, 2005, LN (Lithium niobate, LiNbO3), Available at: http://www.lcoptical.com/LiNbo3/LiNbo3.html Accessed 20 March 2015

[53] T. J. Allen, M. O. Berendt, J. Spurrell, S. U. Alam, E. Z. Zhang, D. J. Richardson, P. C. Beard (2016) Novel fibre lasers as excitation sources for photoacoustic tomography and microscopy Proc. SPIE 9708, Photons Plus Ultrasound: Imaging and Sensing 2016, 97080W

[54] Laser Components, 2011, Lithium Triborate (LiB_3O_5, LBO) Available at: http://www.lasercomponents.com/DataSheets Acessed 11 March 2015

[55] Richard L.Sutherland, 2003, Handbook of Nonlinear Optics, CRC Press

[56] A. Fix, T. Schröder, R. Wallenstein, J. G. Haub, M. J. Johnson, and B. J. Orr, 1993, Tunable β-Barium Borate Optical Parametric Oscillator: Operating Characteristics with and Without Injection Seeding, Journal of the Optical Society of America B, Vol. 10, Issue 9, 1744-1750

[57] R.C. Bapna, C.S. Rao, and K. Dasgupta, 2008, Low-Threshold Operation of a 355-nm Pumped Nanosecond β-BaB_2O_4 Optical Parametric Oscillator, Optics & Laser Technology, Vol. 40, Issue 6, 832-837

7 Publication List

T. J. Allen, M. O. Berendt, J. Spurrell, S. U. Alam, E. Z. Zhang, D. J. Richardson, P. C. Beard (2016) Novel fibre lasers as excitation sources for photoacoustic tomography and microscopy Proc. SPIE 9708, Photons Plus Ultrasound: Imaging and Sensing 2016, 97080W

Berendt, M.O., Spurrell, J., Barua, P., Umnikov, A.A., Nuez Velazquez, M., Sahu, J.K., Alam, S.U. and Richardson, D.J. (2015) 5mJ pulsed Yb-doped all-fiber MOPA seeded by 0.2nm spectrally sliced super luminescent diode At CLEO/Europe 2015 - European Conference on Lasers and Electro-Optics, Germany. 21 - 25 Jun 2015